UNIVERSITY OF CALIFORNIA SAN DIEGO

Turbulent Mixing in the Ocean Surface Boundary Layer

A dissertation submitted in partial satisfaction of the
requirements for the degree Doctor of Philosophy

in

Oceanography

by

Alexander Andriatis

Committee in charge:

Matthew H. Alford, Chair
Luc Lenain, Co-Chair
Matthew Mazloff
Robert Pinkel
Sutanu Sarkar

2025

The Dissertation of Alexander Andriatis is approved, and it is acceptable in quality and form for publication on microfilm and electronically.

University of California San Diego

2025

TABLE OF CONTENTS

Dissertation Approval Page iii

Table of Contents iv

List of Figures vi

Acknowledgements ix

Vita xi

Abstract of the Dissertation xii

Introduction 1

Chapter 1 Observations and Numerical Simulations of the Onset and Growth of Langmuir Circulations 4
1.1 Introduction 5
1.2 Methods 9
1.2.1 Experiment 9
1.2.2 Instrumentation 12
1.2.3 Scale analysis 14
1.2.4 Large-eddy simulation 23
1.3 Onset of Langmuir Circulations 25
1.3.1 Fetch-limited wind forcing 25
1.3.2 Airborne infrared observations 25
1.3.3 Comparison with idealized LES 32
1.4 Growth of Langmuir circulations and diurnal warm layer deepening 34
1.4.1 Afternoon sea breeze 34
1.4.2 Airborne infrared and subsurface observations 36
1.4.3 Comparison with LES forced from observations 39
1.4.4 Subsurface observations of full mixed-layer depth LCs 44
1.5 Summary and Discussion 46
1.6 Acknowledgments 50

Chapter 2 Observations of turbulent structures at the base of the ocean mixed layer . . 52
2.1 Introduction 53
2.2 Methods 56
2.2.1 Experiment 56
2.2.2 Instrumentation 57
2.3 Qualitative observations of transition layer coherent structures across forcing regimes 63
2.3.1 Wind-wave forcing with surface cooling 70
2.3.2 Wind-wave forcing with weak surface heating 70

2.3.3 Convective cooling with weak wind forcing 72
2.3.4 Diurnal warm layer with weak wind forcing 73
2.4 Scaling of the transition layer turbulence 75
2.5 Mixed Layer Deepening, Entrainment Rate, and Heat Budget 78
2.5.1 Diascalar flux from temperature gradients 80
2.5.2 Thorpe scales 81
2.5.3 Comparison of entrainment estimates 83
2.6 Discussion and Summary 85
2.7 Acknowledgments 89

Chapter 3 Observations of near-inertial wave generation and ζ-refraction from a drifting array 90
3.1 Introduction 91
3.2 Methods 92
3.2.1 Experiment 92
3.2.2 Instrumentation 93
3.3 Mixed Layer Kinetic Energy Budget 97
3.4 Downward NIWs and Vorticity Gradients 102
3.5 Upward NIWs 108
3.6 Discussion and Summary 109
3.7 Acknowledgments 110

Appendix A Supplemental information for Chapter 1 111
A.1 2D Temperature Wavenumber Spectra and LC Scales 111
A.2 Timeseries of Scaling Parameters 112

Appendix B Supplemental information for Chapter 2 114
B.1 Gaussian Fitting to Boundary Layer Heave 114

Bibliography 116

LIST OF FIGURES

Figure 1.1. Map showing the Catalina experiment region and deployed assets. 10

Figure 1.2. Meteorological and oceanic forcing from wave glider *Planck*. 11

Figure 1.3. Observational platforms during the Catalina Basin deployment. 14

Figure 1.4. Comparison of Stokes drift estimates. 21

Figure 1.5. Scale analysis of TKE production from surface forcing. 22

Figure 1.6. Aircraft transects and subsurface platform positions during the Catalina Basin deployment. 26

Figure 1.7. Surface temperature from transects of airborne infrared imagery. 28

Figure 1.8. Representative samples of surface temperature from the airborne IR camera for different wind conditions. 29

Figure 1.9. Composite IR camera frame showing the sharp contrast between regions with LCs and a patch of unbroken cool skin. 31

Figure 1.10. Conceptual schematic showing the spatial filtering effect of a convective downwelling region on surface gravity waves. 31

Figure 1.11. Spectra of observed sea surface temperature, separated by wind-relative orientation and binned by wind speed. 32

Figure 1.12. Idealized LES run with stabilizing surface heating. 33

Figure 1.13. Representative samples of surface temperature from the idealized LES and the corresponding temperature wavenumber spectra. 35

Figure 1.14. Comparison between subsurface observations and LES of diurnal warm layer deepening. 37

Figure 1.15. Comparison between observations and LES of sea surface temperature of LCs during diurnal warm layer deepening. 38

Figure 1.16. Comparison between observations and LES of subsurface temperature structures. 40

Figure 1.17. Profiles of LES initial conditions for realistic forcing run. 41

Figure 1.18. Comparison of observations to LES run with different implementation of surface heating. 42

Figure 1.19. Domain-averaged LES profiles during diurnal warm layer deepening. 43

Figure 1.20. Observations of Langmuir circulations from the offshore thermistor chain. 45

Figure 1.21. The cross-cell spacing determined from spectra of sea surface temperature from LES and observations. 50

Figure 2.1. Map showing the offshore experiment region and trajectories of deployed assets. 57

Figure 2.2. Data summary of meteorological and subsurface observations. 58

Figure 2.3. Components of the calculation of non-dimensional TKE production scaling. 65

Figure 2.4. Scale analysis of the forcing, shown as a scatter plot of 10-minute binned observations using the non-dimensional parameter space La_t vs. Λ. 66

Figure 2.5. 3-hour temperature timeseries showing the behavior of the upper mixed layer for four selected times. 67

Figure 2.6. Observations of the transition layer during wind-wave dominated forcing with surface cooling. 71

Figure 2.7. Observations of the transition layer during wind-wave dominated forcing with weak surface heating. 72

Figure 2.8. Observations of the transition layer during convectively-dominated forcing with weak wind forcing. 73

Figure 2.9. Observations of the transition layer below a diurnal warm layer during stabilizing buoyancy forcing with weak wind forcing. 74

Figure 2.10. Shear and stratification scaling for the transition layer, using one-hour averages of T-chain data. 76

Figure 2.11. Scaling parameters for stratified turbulence in the transition layer. 77

Figure 2.12. Histogram of Thorpe scales L_T observed in the transition layer. 82

Figure 2.13. Summary of the mixed layer deepening budget. 86

Figure 2.14. Comparison between wind friction velocity, Thorpe scales, and outer vertical turbulent patch scales. 88

Figure 3.1. Schematic of the drifting Wirewalker and T-chain array. 94

Figure 3.2. Summary of observed fields for WW1, representative of all WW observations. 95

Figure 3.3. Mean profiles of sorted CTD variables for each WW. 95

Figure 3.4. Reference profiles used for WKB scaling for all of the Wirewalkers. 96

Figure 3.5. Rotary frequency spectrum of velocity and shear from each of the Wirewalkers. 99

Figure 3.6. Inertial kinetic energy budget. 103

Figure 3.7. Downward component of vertical shear of zonal velocity from each Wirewalker, in WKB-stretched isopycnal coordinates. 104

Figure 3.8. Vorticity estimated from plane fits to wirewalker velocity observations along isopycnals. 105

Figure 3.9. Lateral vorticity gradient magnitude and direction. 106

Figure 3.10. Plane wave fit to the downward component of shear in WW3, on isopycnal WKB coordinates. 106

Figure 3.11. Downward-propagating component of (a) zonal and (b) meridional shear at the 170 m_{WKB} isopycnal. 108

Figure 3.12. Wavenumber magnitude from multi-ww plane fits to shear phase. 108

Figure 3.13. Upward component of vertical shear of zonal velocity from each Wirewalker, in WKB-stretched isopycnal coordinates. 109

Figure A.1. 2D temperature wavenumber spectra and LC scales. 112

Figure A.2. Timeseries of scaling parameters. 113

Figure B.1. Example of Gaussian fits to segments of isopycnal displacement in the transition layer. 115

ACKNOWLEDGEMENTS

I would like to thank my advisors Matthew Alford and Luc Lenain for their guidance, encouragement, mentorship, and trust over the course of this scientific journey. They provided me with both the flexibility to pursue creative ideas and the discipline to produce results which were essential to this dissertation. I also thank committee members Matthew Mazloff, Robert Pinkel, and Sutanu Sarkar, along with Bruce Cornuelle and Sarah Gille for their support and constant willingness to share their time and scientific prowess. I am incredibly grateful to the faculty at Scripps for teaching me about the ocean.

Thank you to my collaborators and co-authors Nathaniel Winstead and Joseph Geiman at Johns Hopkins APL for their generosity and numerical expertise, as well as Drew Lucas and Sophia Merrifield for sharing their skills in observational oceanography. I am forever grateful to William Kuperman for leading the Task Force Ocean observational campaign that made this dissertation possible.

The Multiscale Ocean Dynamics group have been incredible colleagues. Their scientific, engineering, and seagoing abilities are outdone only by their vibrant personalities. Thank you to all of the PIs, researchers, postdocs, grad students, and engineers that have created such a supportive and welcoming scientific culture. Thanks especially to Sara Goheen, San Nguyen, Nicole Couto, Arnaud Le Boyer, Jonny Ladner, Spencer Kawamoto, and all the other engineers and technicians that supported the instrumentation used in this dissertation. The Air-Sea Interaction group and Coastal Observing Research and Development Center were also essential to the data used in this thesis, especially Laurent Grare and Nick Statom. I would also like to thank the captain and crews of the *Sally Ride*, *Roger Revelle*, *Bob and Betty Beyster*, *Sproul*, and *Sikuliaq*, all of whom enabled successful and rewarding seagoing experiences.

The graduate student body at Scripps was the bedrock of my experience here. Thank you to all my fellow students for their camaraderie, solidarity, and resilience. It was a joy to watch all my friends mature as scientists and human beings and set out on great paths in life. Thanks for every Wednesday hangout, pickleball session, TG green flash, all-at-sio email, and camping trip.

Thank you to my mom and grandparents, who instilled in me curiosity, hard work, ambition, and perseverance, and encouraged me every step of the way. And finally thank you to Bethan Wynne-Cattanach for being the most supportive partner in the office, in class, at sea, and in our adventures together.

Chapter 1, in full, is a reprint of the material as it appears in Journal of Physical Oceanography (2024). Andriatis, Alexander, Luc Lenain, Matthew H. Alford, Nathaniel Winstead, and Joseph Geiman. "Observations and Numerical Simulations of the Onset and Growth of Langmuir Circulations". DOI:10.1175/JPO-D-24-0004.1. The dissertation author was the primary investigator and author of this paper.

Chapter 2, in part is currently being prepared for submission for publication of the material. Andriatis, Alexander, Matthew H. Alford, Luc Lenain, Andrew J. Lucas, Sophia Merrifield. The dissertation author was the primary investigator and author of this material.

Chapter 3, in part is currently being prepared for submission for publication of the material. Andriatis, Alexander, Matthew H. Alford, Luc Lenain, Andrew J. Lucas, Sophia Merrifield. The dissertation author was the primary investigator and author of this material.

VITA

2018	Bachelor of Science in Physics, Massachusetts Institute of Technology
2025	Doctor of Philosophy, Scripps Institution of Oceanography, University of California San Diego

PUBLICATIONS

Andriatis, Alexander, Luc Lenain, Matthew H. Alford, Nathaniel Winstead, and Joseph Geiman. "Observations and Numerical Simulations of the Onset and Growth of Langmuir Circulations." *Journal of Physical Oceanography* 54.8 (2024): 1737-1763.

ABSTRACT OF THE DISSERTATION

Turbulent Mixing in the Ocean Surface Boundary Layer

by

Alexander Andriatis

Doctor of Philosophy in Oceanography

University of California San Diego, 2025

Matthew H. Alford, Chair
Luc Lenain, Co-Chair

Turbulent mixing in the ocean surface boundary layer (OSBL) mediates the transfer of energy, momentum, and gases between the atmosphere and the ocean. While the dynamics that drive these exchanges happen on small lateral and vertical scales relative to the size of the ocean, they are crucial in setting the behavior of Earth's climate on global scales. Historically, small-scale processes near the ocean's surface have been difficult to observe. Using novel measurements of the OSBL enabled by advances in instrumentation and multi-platform observational techniques, this thesis investigates specific OSBL turbulent dynamics. The onset and growth of Langmuir circulations (LCs) is observed from simultaneous airborne infrared imagery of sea surface

temperature and subsurface in-situ measurements. For weak, fetch-limited wind wave forcing with stabilizing buoyancy forcing, LCs appear non-uniformly in space. During a period of LC growth and diurnal warm layer (DWL) deepening, subsurface temperature structures show temperature intrusions into the base of the DWL of the same scale as bubble entrainment depth during the deepening period. A large-eddy simulation run with observed initial conditions and forcing reproduces the onset and rate of DWL deepening, but exhibits coherent temperature structures with a larger aspect ratio than in observations, with large sensitivity to the numerical representation of surface radiative heating. At the base of the mixed layer, a drifting thermistor chain is used to observe temperature fluctuations consistent with turbulence in a stratified shear layer resulting from a mixture of Kelvin-Helmholtz and Holmboe instabilities. The size and frequency of these structures depends on the surface forcing regime, defined by the balance of wind-shear, wave-shear, and convective turbulent kinetic energy production. Thorpe scale estimates of dissipation and entrainment are consistent with the observed rate of mixed layer deepening, while the outer vertical scale of the turbulent region is correlated with the wind forcing magnitude. Below the mixed layer, observations of velocity from an array of drifting profiling instruments are used to relate spatial gradients in near-inertial wave energy flux to array-scale lateral vorticity gradients. These unique observational studies can aid in improving future numerical simulations and parametrizations used in global climate simulations.

Introduction

The ocean surface boundary layer (OSBL) connects the atmosphere to the ocean, mediating the transfer of energy, momentum, and gases, exchanges that are crucial in governing Earth's climate. The rate of air-sea exchange is driven by turbulence resulting from wind, wave, and buoyancy forcing (Fox-Kemper et al. 2022). While the dynamics that drive these exchanges happen on small lateral and vertical scales relative to the size of the ocean, they are crucial in setting the behavior of Earth's climate on global scales (Sullivan and McWilliams 2010). Part of the reason for the large-scale significance of the OSBL is that the dominant source of power for oceanic motions is input by wind friction at the surface (70 TW; Wunsch 2020). The distribution of wind energy into currents, surface waves, and internal waves determines how and where the energy is dissipated, which in turn governs processes like water mass transformation, geochemical exchanges, biological productivity, and the distribution of pollutants (Fox-Kemper et al. 2022). Because the dynamics of the OSBL are globally important but happen on small scales, they are generally parametrized in ocean models (Large et al. 1994). The specifics of these parametrizations can have a significant impact on estimates of overall regional ocean and atmospheric conditions in the near-term, and climate trends on long time scales (Large et al. 1997; Jochum et al. 2012; Li et al. 2016). To improve parametrizations and model accuracy, there is an ongoing need for observations of the OSBL, which has historically been difficult to sample because of the high spatial and temporal resolution needed to study the relevant dynamics. This thesis leverages advances in instrumentation and multi-platform operations to study dynamical processes in the OSBL.

One important dynamical process in the OSBL is Langmuir turbulence (LT) and the

associated coherent dynamical structures called Langmuir circulations (LCs) (Langmuir 1938; Thorpe 2004). Langmuir turbulence is now understood to be a leading-order mixing process in the OSBL, and needs to be included in global climate models, in particular to improve mixed layer depth accuracy (Belcher et al. 2012; Li et al. 2019). In-situ ocean observations of Langmuir circulations come from a handful of experiments across a relatively narrow range of wind and buoyancy forcing regimes, and few have characterized both the lateral and vertical structure of coherent vortices (Weller and Price 1988; Zedel and Farmer 1991a; Smith 1992; Plueddemann et al. 1996). Instead, LT has been studied primarily using large-eddy simulations (LES) (Skyllingstad and Denbo 1995; McWilliams et al. 1997; Kukulka et al. 2010), with recent work aimed at representing a broad range of realistic forcing conditions (Harcourt and D'Asaro 2008; Van Roekel et al. 2012; McWilliams et al. 2014; Wang et al. 2019; Fan et al. 2020; Wang et al. 2022). While LES have been useful tools in studying LT and in the development of parametrizations, it remains important to validate their performance against observations. Chapter 1 studies the onset and growth of LCs using a unique combination of simultaneous airborne and subsurface in-situ measurements, and evaluates the ability of an LES run with observed forcing to reproduce LC behavior.

The interaction between the OSBL and the interior of the ocean is governed by turbulent processes at the base of the boundary layer, a region commonly referred to as the transition layer (TL). Here, turbulent forcing interacts with strong stratification of the upper thermocline, leading to mixing between surface waters and the ocean interior. Large-scale climate and biological models are sensitive to the exchange of heat, freshwater, carbon dioxide, and nutrients across the transition layer, but accurately parametrizing these processes is challenging (Ferrari and Boccaletti 2004). Mixing in the TL is particularly complicated because surface forcing, such as surface wind stress, surface heating and cooling, and Langmuir turbulence interacts with subsurface forcing such as shear from internal waves in the thermocline, subsurface ocean currents, and submesoscale eddies, to produce a rich variety of turbulent velocity production (Fox-Kemper et al. 2022). This turbulent production leads to a variety of instabilities at the base

of the mixed layer such as Kelvin Helmholtz (KH) billows, Holmboe (H) instability scouring, and convective plumes (Smyth and Peltier 1991). Understanding the conditions under which these instabilities arise and their effect on modifying the structure of both the mixed layer and the thermocline below it is essential to accurately model the mixed layer. LES and direct numerical simulation (DNS) have been widely used to study stratified shear turbulence (Smyth and Moum 2000; Peltier and Caulfield 2003; Pham et al. 2009; Watanabe et al. 2018; Sarkar and Pham 2019; Kaminski and Smyth 2019; VanDine et al. 2021), but models are limited in their ability to represent the richness of stratification and shear profiles present in a real ocean. In-situ observations of turbulent structures in the boundary layer are therefore necessary to understand the effects of combining a multitude of forcing mechanisms. Chapter 2 uses a drifting thermistor chain with high vertical and temporal resolution to visualize coherent turbulent structures in the transition layer and relate their vertical scale to surface forcing regimes.

Finally, wind energy input into the OSBL that is not dissipated as heat or converted to potential energy through thermocline entrainment in the transition layer can be radiated into the ocean interior in the form of near-inertial internal waves (NIWs) (Alford et al. 2016). The generation and propagation of wind-driven NIWs is important because their energy input into the ocean interior has been estimated to be of the same magnitude (O(1 TW); Alford 2001, 2003a; Watanabe and Hibiya 2002), as the energy from internal tide generation, processes which together account for the majority of mixing in the ocean interior (Waterhouse et al. 2014; MacKinnon et al. 2017). Global estimates of the amount of wind work going into NIW generation have large uncertainties due to the treatment of the forcing stress profile in 1-D models (Stokes et al. 2024), the amount of energy lost to turbulence (Alford 2020b), and the effect of the interaction of the submesoscale with inertial oscillations (Asselin and Young 2020). Chapter 3 uses a drifting profiler array to investigate the effect of submesoscale vorticity gradients on the near-inertial kinetic energy budget for the conversion of wind work to NIW propagation into the interior.

Chapter 1

Observations and Numerical Simulations of the Onset and Growth of Langmuir Circulations

We report novel observations of the onset and growth of Langmuir circulations (LCs) from simultaneous airborne and subsurface in-situ measurements. Under weak, fetch-limited wind wave forcing with stabilizing buoyancy forcing, the onset of LCs is observed for wind speeds greater than about 1 m s^{-1}. LCs appear non-uniformly in space, consistent with previous laboratory experiments and suggestive of coupled wave-turbulence interaction. Following an increase in wind speed from < 1 m s^{-1} to sustained 3 m s^{-1} winds, a shallow (< 0.7 m) diurnal warm layer is observed to deepen at 1 m hr^{-1}, while the cross-cell scales of LCs grow at 2 m hr^{-1}, as observed in sea surface temperature collected from a research aircraft. Subsurface temperature structures show temperature intrusions into the base of the diurnal warm layer of the same scale as bubble entrainment depth during the deepening period, and are comparable to temperature structures observed during strong wind forcing with a deep mixed layer that is representative of previous LC studies. We show that an LES run with observed initial conditions and forcing is able to reproduce the onset and rate of boundary layer deepening. The surface temperature expression however is significantly different from observations, and the model exhibits large sensitivity to the numerical representation of surface radiative heating. These novel observations of Langmuir circulations offer a benchmark for further improvement of numerical models.

1.1 Introduction

The ocean surface boundary layer (OSBL) connects the atmosphere to the ocean, mediating the transfer of energy, momentum, and gases, exchanges which are crucial in governing Earth's climate. The rate of air-sea exchange is driven by turbulence resulting from wind, wave, and buoyancy forcing (Fox-Kemper et al. 2022). Early efforts to understand mixing in the OSBL centered on shear instability forced by wind stress and convective instability from surface heat fluxes (Large et al. 1994). Wind-driven surface waves were found to influence mixing through wave breaking and Langmuir turbulence (LT) (D'Asaro et al. 2014; Sutherland and Melville 2015). LT is generated by the interaction of horizontally sheared surface currents with the Stokes drift of surface gravity waves. The vertical shear resulting from Stokes drift tilts vertical vorticity created by surface currents in the direction of wave propagation, creating wind-aligned roll vortices, a process known as the CL2 mechanism (Craik and Leibovich 1976). Pairs of vortices are spaced at regular intervals with a separation of about two times the boundary layer depth, forming coherent dynamical structures called Langmuir circulations (LCs) (Thorpe 2004). At the surface, pairs of roll vortices form convergence zones which concentrate buoyant particles such as algae or bubbles into elongated windrows, the commonly recognized surface expression of LCs (Langmuir 1938; Farmer and Li 1995). Below these convergence rows, subduction can entrain particles (Weller et al. 1985), but also plays an important role in momentum transfer from the surface, enhancing Eulerian shear and turbulent kinetic energy (TKE) at the base of the boundary layer (Li et al. 1995; Kukulka et al. 2010). Advancing our understanding of coherent LC structure can improve modeling of OSBL processes, such as the interaction of LCs with internal waves (Chini and Leibovich 2003) or fronts (Sullivan and McWilliams 2017), the scattering of sound off bubbles near the surface (Thorpe, Osborn, Farmer, et al. 2003), the dispersion of buoyant particles such as oil spills (Simecek-Beatty and Lehr 2017), biology (Larson 1992; Dierssen et al. 2015), and plastics (Cózar et al. 2021; Sutherland et al. 2023), the formation of sea ice (Drucker 2003; Ciappa and Pietranera 2013), and applications to industry such as aquaculture

(Yan et al. 2021) and wind power (Dorrell et al. 2022).

Langmuir turbulence is now understood to be a leading-order mixing process in the OSBL, and needs to be included in global climate models, in particular to improve mixed layer depth accuracy (Belcher et al. 2012). Early parametrizations of LT related TKE production to idealized parameters of wind stress and surface Stokes drift through the turbulent Langmuir number (McWilliams and Sullivan 2000). Including effects such as wind-wave misalignment and varying wave states has led to improvements in its parametrization (Smyth et al. 2002; Li et al. 2017; Li and Fox-Kemper 2017; Solano and Fan 2022). Including a parametrization of LT in regional (Schultz et al. 2020) and global ocean models (Li et al. 2017; Li and Fox-Kemper 2017) has significant impacts on mixed layer depth and can affect long-term ocean and climate trends (Li et al. 2016; Ali et al. 2019), but large differences due to model specifics need to be resolved, especially during mixed-layer deepening and strong diurnal forcing (Li et al. 2019; Pham et al. 2023; Johnson et al. 2023).

Studies of LT behavior have primarily relied on large-eddy simulation (LES) models with CL2 vortex forcing (Skyllingstad and Denbo 1995; McWilliams et al. 1997). While early LES was largely used to model an idealized ocean, advances in understanding processes which impact LT scaling were made by simulating increasingly realistic ocean conditions, such as varying the decay scale of the Stokes drift (Harcourt and D'Asaro 2008) and changing the wind and wave directional alignment (Van Roekel et al. 2012; McWilliams et al. 2014; Wang et al. 2019). To further enhance realism, recent LES studies have run simulations with observed ocean and atmospheric conditions. Kukulka et al. (2009) find that LES reproduces mixed layer deepening and LC scale growth seen by Smith (1992) during a wind forcing event only when including LC effects. Kukulka et al. (2010) find that LT can enhance TKE production due to Stokes drift shear in the middle of the mixed layer, and the downwelling transfer of horizontal momentum interacts with the base of the thermocline, enhancing shear-driven instabilities and associated mixing. By comparing to observations with wind-wave misalignment and fetch-limited winds, Fan et al. (2020) find that LT can lead to a TKE reduction in a swell-dominated wave field with

under-developed wind seas by reducing shear production, and Wang et al. (2022) find reduced LT strength for fetch-limited winds, with less organized coherent LCs for misaligned wind and waves.

Few LES studies have modeled LT under stabilizing surface buoyancy forcing, in part because of the fine vertical grid spacing required to resolve turbulence for the shallowest diurnal warm layers (Beare et al. 2006). Min and Noh (2004) and Noh et al. (2009) show that LCs are important for the formation of a diurnal warm layer (DWL), but that sufficiently strong buoyancy forcing can inhibit LC formation. Conversely, Kukulka et al. (2013) show that sufficiently strong LT can inhibit diurnal restratification. Pearson et al. (2015) find a scaling for the boundary layer depth under stabilizing surface buoyancy forcing that is set by the initial mixed layer depth under equilibrium wind seas, and the relative strength of buoyancy to wave forcing. Their simulations, however, do not account for changing wind forcing or for shallow diurnal warm layers under strongly stabilizing forcing whose depth is comparable to the Stokes drift decay scale. Wang et al. (2023) further develop boundary layer depth scaling that depends on wave, wind, and buoyancy forcing. Pham et al. (2023) demonstrate the importance of LT interacting with diurnal buoyancy forcing in LES studies of mixed layer behavior of Monsoon Intra-seasonal Oscillations.

In laboratory studies, LCs were generated shortly after the appearance of surface waves, on a time scale associated with the acceleration of a surface shear layer (Melville et al. 1998; Veron and Melville 2001). Recent experiments show that the onset of instability leading to Langmuir turbulence is sensitive to wave conditions, making wave-averaged LES models limited by their inability to capture the coupling between Langmuir turbulence and the surface wave field (Wagner et al. 2023). To properly represent LCs in models, parametrizations and LES need to be validated with observations across a variety of ocean and atmospheric conditions.

In-situ ocean observations of Langmuir circulations come from a handful of experiments across a relatively narrow range of wind and buoyancy forcing regimes, and few have characterized both the lateral and vertical structure of coherent vortices. Weller and Price (1988) observed the three-dimensional flow structure of Langmuir circulations using buoyant drifters in combination

with vector current meters deployed from R/P *FLIP*. In regions of convergent surface flow, downward vertical and downwind horizontal velocities were observed of similar magnitude, with a subsurface maximum in the downwind jet. Sidescan sonar imaging of bubble clouds can provide a two-dimensional sonar image over a limited range, revealing the shape of convergence and downwelling zones where bubbles are entrained (Zedel and Farmer 1991a; Farmer and Li 1995). Smith (1992) used surface velocity from sidescan sonar to trace the growth of LCs, finding that streak spacing between pairs of convergent bubble entrainment regions grew at about twice the rate of the deepening of the mixed layer, indicating a cell aspect ratio of about 1:1. Plueddemann et al. (1996) found a hierarchy of LC spacing over a broad wavenumber range (10 - 200 m), and a dependence of LC strength on both wind friction and Stokes drift magnitude in support of turbulent Langmuir number scaling (McWilliams et al. 1997). More recently, Chang et al. (2019) measured the cross-cell separation scale of Langmuir circulations using optically-tracked bamboo surface drifters, finding a hierarchy of LC spacing. Temperature patterns can also be used to identify convergence and downwelling zones. At the surface, upwelling areas of LCs break the cool skin, leading to a cold signature in regions of convergence and downwelling (Veron et al. 2008a). Veron et al. (2009) showed the correlation between temperature structures of cool jets with broader warm patches and a surface velocity field consistent with Langmuir circulations using infrared (IR) imagery with particle image velocimetry. Airborne IR imagery has also been used for fine spatial and temperature resolution measurements of surface skin temperature (Zappa and Jessup 2005). Marmorino et al. (2005), Marmorino et al. (2007), and Marmorino et al. (2008) used airborne IR to identify Langmuir circulations over a large area, but lacked subsurface measurements to relate cell spacing to the boundary layer depth.

The goals of this study are to characterize the three-dimensional scales of LCs and the ocean and atmospheric forcing that governs their time evolution, and to evaluate the ability of an LES forced from observations to reproduce the observed structure of LCs. We present the first simultaneous airborne and subsurface measurements of a wind forcing event leading to the onset of Langmuir circulations, allowing us to relate the surface cell structure to subsurface

temperature patterns and boundary layer deepening. We collected data offshore of the Southern California coast in November 2020. Observations in the Catalina Basin were characterized by a period of relatively low winds, small waves, and a shallow diurnal warm layer (DWL) with daytime heating and nightly cooling of the ocean surface. The onset of LCs was observed from airborne infrared imagery of sea surface temperature during a morning land breeze, followed by a stronger afternoon sea breeze that led to boundary layer deepening and growth of larger LCs, observed by airborne IR and thermistor chains on autonomous wave gliders. During a wind event further offshore with a deeper mixed layer, we observe similar subsurface temperature structures. We contextualize the wind, wave, and buoyancy forcing during our observations with non-dimensional scale analysis. We compare our observations to an LES model initialized by observed ocean and atmospheric conditions, and forced with observed wind and buoyancy forcing, with a Stokes drift parametrization based on the observed wind friction. In section 1.2 we review the experiment, instrumentation, and LES methodology. In section 1.3 we observe the onset and spatial structure of Langmuir circulations, and compare with an idealized LES run. In section 1.4 we observe the growth of LCs and deepening of the shallow surface warm layer under sustained wind forcing, and compare surface and subsurface temperature structures with LES and with a more typical strong forcing regime. In section 1.5 we discuss and summarize the results.

1.2 Methods

1.2.1 Experiment

The data used in this paper were collected as part of the Task Force Ocean (TFO) "Platform Centric ASW Processing with Through-the-Sensor Data Assimilation and Fusion" experiment off the coast of Southern California in November 2020 (doi:10.6075/J0VQ32W2; Andriatis et al. 2023). The experiment was conducted in two parts, a deployment in deep water (4 km, hereafter "offshore") between 5 November and 14 November 2020, and a deployment in the Catalina Basin between 15 November and 24 November 2020. The deployments were based

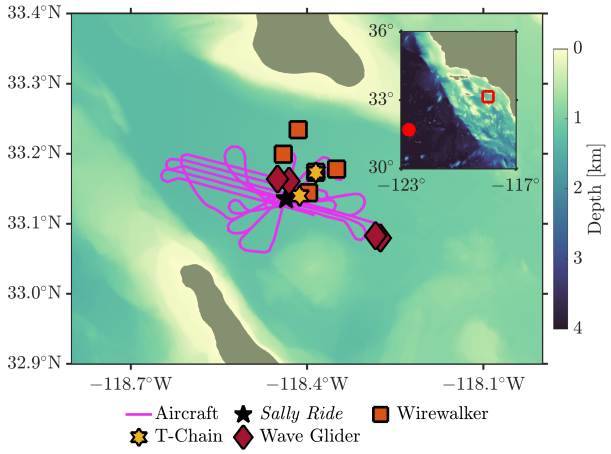

Figure 1.1. Map showing the Catalina experiment region and deployed assets. The inset shows the larger California coast region, with the Catalina experiment area (red square outline) and the offshore experiment area (red circle). Aircraft tracks (pink) are plotted for flights from 1700 to 1800 UTC 20 Nov and 0000 to 0100 UTC 21 Nov. Asset locations are shown for their position at 2100 UTC 20 Nov.

aboard the *R/V Sally Ride*, accompanied by numerous drifting instruments and remotely-piloted wave gliders. During the Catalina deployment, the *Sally Ride* was joined by the *R/V Bob and Betty Beyster* and a fixed-wing aircraft. The *Beyster* provided assistance in repositioning assets as they drifted out of the operational region by strong along-channel currents, while the aircraft gathered aerial imagery of the ocean surface in transects over the experiment region. Figure 1.1 shows a snapshot of deployed assets in the Catalina Basin, with an inset showing the larger California coast region and the offshore experiment site.

Because we are interested in observing how the scales of LCs evolve with changing atmospheric and ocean conditions, we focus on observing the evolution of LCs during and after a rapid increase in the wind stress on the ocean surface. Observations of wind during the experiment show a diurnal pattern of increased speeds during the afternoon sea breeze. The biggest relative increase in winds occurs on the afternoon of 20 November, with low winds of 1 m s^{-1} during the day rapidly increasing to 5 m s^{-1} into the evening (Figure 1.2). For the majority of the analysis we will focus on the time period from 1500 UTC 20 November to 0300 UTC 21 November (the local experiment time is UTC-8).

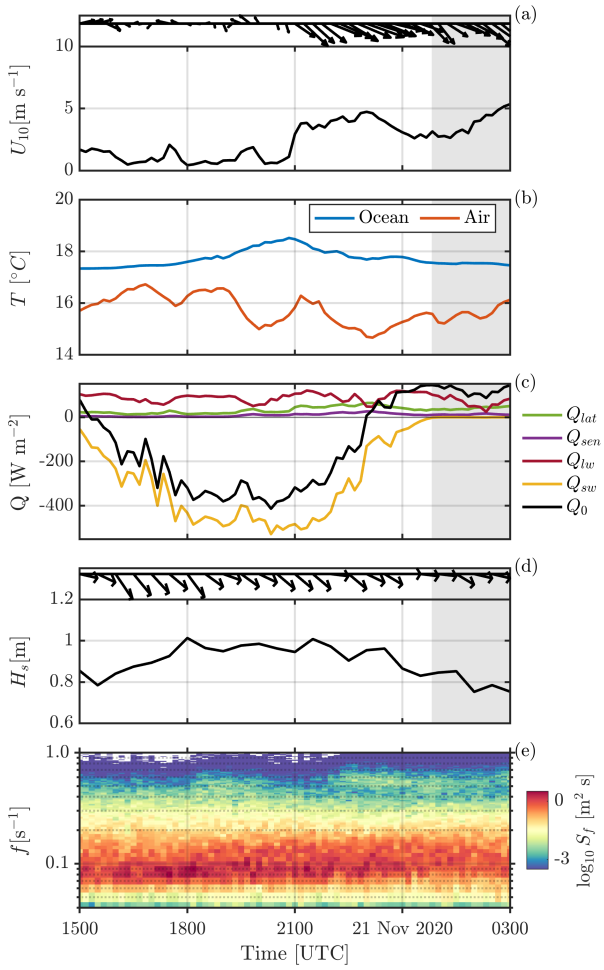

Figure 1.2. Meteorological and oceanic forcing from wave glider *Planck*: (a) Wind speed referenced to 10 m height U_{10} with a feather plot indicating wind direction (going towards); (b) Water temperature from CTD at 0.3 m depth (blue) and air temperature form wave glider met package at 1 m height (red); (c) Surface heat flux components: (green) latent heat, (purple) sensible heat, (red) net longwave radiation, (yellow) downwelling shortwave radiation, and (black) the net surface heat flux, with positive values corresponding to ocean cooling. (d) Significant wave height H_s and wave direction at peak frequency (going towards); (e) Omnidirectional frequency spectrum of wave energy vs. time, with logarithmic color scale. Nighttime is shaded in gray.

1.2.2 Instrumentation

The *Sally Ride* provided observations of atmospheric conditions - air temperature, humidity, pressure, and precipitation, along with downwelling solar shortwave and longwave radiation. A flow-through CTD system recorded ocean temperature and salinity at 5 m depth. We also deployed a FastCTD system (Klymak et al. 2008), a winched CTD capable of profiling at speeds of 3 - 5 m s^{-1}, resulting in profiles to 200 m every 2 - 3 minutes.

Autonomous surface vehicles provide a rich dataset of atmospheric and near-surface observations. During the Catalina deployment, three Liquid Robotics SV2/SV3 wave gliders (*Planck*, *Stokes*, and *Kelvin*) were equipped with a meteorological package and flow-through CTD, a thermistor chain along the umbilical between 0 - 8 m depth, and an upward-looking Signature 1000 ADCP on the subsurface platform and downward-looking ADCP mounted on the surface float (Grare et al. 2021; Hodges et al. 2023) (Figure 1.3). The umbilical thermistor chains sampled at 1 Hz and provide a dense vertical resolution of temperature in the upper boundary layer, with thermistors at 0.70, 0.95, 1.20, 1.45, 1.80, 2.30, 2.80, 3.55, 4.30, 5.05, 6.05, 7.05, and 8.05 m depth, with an additional CTD mounted on the keel of the surface float at 0.31 m depth. The SV2 wave glider (*Kelvin*) has an additional thermistor chain extending to 40 m depth, enabling temperature observations through the base of the mixed layer which averaged about 25 m deep. The upward-looking ADCP provides high-resolution velocity measurements, and backscatter intensity from the vertical fifth beam at 2 cm resolution. The wave gliders also measure the directional wave field using high-precision GPS and inertial measurement units (IMUs) (Colosi et al. 2023).

During the Catalina deployment, airborne measurements were collected using the Modular Aerial Sensing System (MASS; Melville et al. 2016) during daytime low-altitude flights over the experiment region (Figure 1.3). The primary instrument for this analysis is the longwave infrared camera in the 8.0 - 9.2 μm spectral range. The camera operates at 50 Hz and has a resolution of 0.5- 2 m with a field of view from 300 - 1000 m, depending on flight altitude. Additionally,

the MASS features a waveform scanning LIDAR to measure sea surface topography, which can be used as another record of directional wave information (Lenain and Melville 2017). The images collected by the aircraft are georeferenced using a 200 Hz GPS-IMU. One limitation to the airborne measurements is that collecting images of the sea surface required cloudless daytime conditions, which were rare during the deployment period in the Catalina basin. Composite images of SST are made by combining individual georeferenced images along the aircraft's flight path into a mosaic, with each 2 m x 2 m pixel formed by averaging about 900 images for a flight speed of 55 m s^{-1}, 50 Hz camera frequency, and 1000 m aperture. Temperature mosaics are examined individually and only those with small background variability and no cloud contamination are used in the analysis. While infrared imaging of the sea surface has previously been used to calculate surface velocity using particle image velocimetry (e.g. Veron et al. 2008a; Vrećica et al. 2022), the transient flights here are incompatible with this technique as a given image area is not kept in frame for a sufficient time.

During both deployments, an array of drifting instruments supplemented temperature and velocity measurements with greater depth range than the wave glider platforms alone. Five drifting Wirewalkers (Pinkel et al. 2011), vertically profiling wave-powered instruments, were deployed featuring a CTD and upward-looking ADCP (Zheng et al. 2022). Four of the instruments profiled to 500 m while the fifth went to 200 m. The profile repeat times vary with wave conditions, with the fastest repeats being every 7 minutes for the 200 m configuration during the largest swell, and as long as every hour for the 500 m package in calm conditions. Two drifting thermistor chains (T-chains) were deployed with thermistor spacing every 2.5 m and an upward-looking ADCP at the bottom. One chain went to 100 m and featured additional dense thermistor spacing (0.5 m) in the thermocline while the other chain went to 200 m. The sampling frequency of most thermistors was 2 Hz, with some up to 16 Hz.

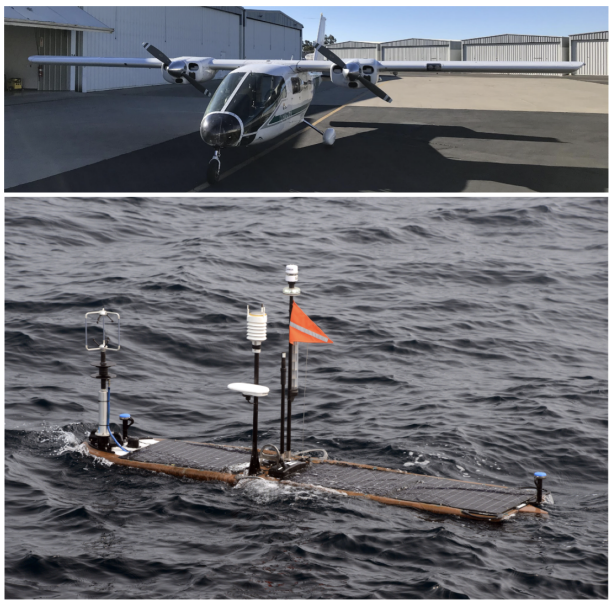

Figure 1.3. (Top) Research aircraft Partenavia P68 operated by Aspen Helicopters (Oxnard, CA), equipped with MASS, used for aerial surveys of the Catalina experiment region. (Bottom) Surface platform and instrumentation of a deployed SV3 wave glider.

1.2.3 Scale analysis

To gauge whether LCs are expected to be an important OSBL driver during the selected observational period, we consider the relative importance of wave-driven turbulence to wind-shear and convectively driven turbulence, following Li et al. 2005. The ratio of wind-forced to wave-forced TKE production is given by the turbulent Langmuir number La_t (McWilliams et al. 1997),

$$\frac{u_*^3/h}{w_{*L}^3/h} = \frac{u_*}{u_{s0}} = \mathrm{La}_t^2, \tag{1.1}$$

where u_* is the friction velocity in water, u_{s0} is the surface Stokes drift, and h is the boundary layer depth. The friction velocity in water u_* is calculated from the wind stress at the surface, τ and the surface water density ρ_0, and is analogous to the friction velocity in air, $\rho_0 u_*^2 = |\boldsymbol{\tau}| = \rho_{\mathrm{air}} u_{*\mathrm{air}}^2$. The vertical velocity scale is given by $w_{*L} = \left(u_*^2 u_{s0}\right)^{1/3}$ (Grant and Belcher 2009). In cases where the wind stress and Stokes drift are misaligned a modified Langmuir number can be used (Van Roekel et al. 2012) since misalignment can impact the strength and orientation of LCs, as

highlighted by recent numerical and observational studies (Wang et al. 2019; Wang and Kukulka 2021a; Wang and Kukulka 2021b; Wang et al. 2022). The LCs in this study are primarily driven by fetch-limited wind waves, which, especially at times of weak offshore wind, are misaligned with remote swell. The differentiation between wind waves and remote swell, along with a changing boundary layer depth, requires the use of a surface-layer Langmuir number (Harcourt and D'Asaro 2008). We follow Van Roekel et al. (2012) in using the surface layer averaged and projected Langmuir number,

$$\mathrm{La}_{\mathrm{SL,proj}} = \sqrt{\frac{u_* \cos(\alpha)}{|\langle \mathbf{u}_s \rangle_{SL}| \cos(\theta_{\mathrm{ww}} - \alpha)}}, \tag{1.2}$$

where $\langle \mathbf{u}_s \rangle_{\mathrm{SL}}$ is the depth-average of the Stokes drift over the top 20% of the boundary layer, θ_{ww} is the angle between the wind and the surface Stokes drift, and α is the angle between the wind and Langmuir cells, approximated by

$$\alpha \approx \tan^{-1}\left[\frac{\sin(\theta_{\mathrm{ww}})}{\frac{u_*}{u_{s0}\kappa}\ln(|h/z_1|) + \cos(\theta_{\mathrm{ww}})}\right], \tag{1.3}$$

with von Kármán constant $\kappa = 0.4$ and z_1 the onset depth of the law of the wall, approximated as four times the significant wave height H_s (Li et al. 2016). We note that this scaling requires the mean Stokes drift shear over the surface layer to be approximated by the surface Stokes drift (Van Roekel et al. 2012). This assumption breaks down during periods of weak offshore wind forcing with a shallow diurnal warm layer, where the Stokes drift of short wind-waves cancels the opposing swell contribution near the surface, dramatically reducing the Stokes drift shear within the surface layer, at times even inverting the sign of the Stokes drift shear. For the offshore region, the Stokes drift is assumed to be aligned with the wind, reducing (1.2) to $\mathrm{La}_{\mathrm{SL}}$.

We use a stability parameter Λ (Chor et al. 2021) as a measure of the relative importance

of convective turbulence to shear turbulence,

$$\Lambda = \kappa \frac{w_*^3}{u_*^3} = -\frac{h}{L_O}, \tag{1.4}$$

where $w_* = (B_0 h)^{1/3}$ is the turbulent convective velocity (Large et al. 1994) and L_O is the Monin-Obukhov length, with surface buoyancy flux B_0. We choose to use Λ as opposed to other commonly used scalings such as the Langmuir stability length (Belcher et al. 2012) or the Hoenikker number (Li et al. 2005) due to its recent use in studies of entertainment buoyancy flux in the surface boundary layer (Li et al. 2017; Chor et al. 2021; Pham et al. 2023). We note that Pearson et al. (2015) introduce a modified Langmuir stability length that uses an effective buoyancy flux to account for distributed radiative heating. While we could apply this modification to our buoyancy flux, we retain the surface definition here for simplicity.

Calculating the parameters $\mathrm{La}_{\mathrm{SL,proj}}$ and Λ requires the water friction velocity, u_*, surface buoyancy flux, B_0, Stokes drift velocity, u_s, and boundary layer depth h. u_* and B_0 are obtained with the help of the COARE algorithm for calculating air-sea fluxes (Fairall et al. 2003), using inputs of observed ocean-relative wind speed, air temperature, pressure, humidity, precipitation, radiative fluxes, near-surface ocean temperature, and significant wave height and phase speed. Atmospheric and ocean measurements from wave glider *Planck* were supplemented with downwelling solar radiation measurements from the *Sally Ride*. The friction velocity in water u_* is calculated from $\boldsymbol{\tau}$ and the sea surface density ρ_0 from the wave glider CTD at 0.31 m depth. Surface buoyancy flux is given by

$$B_0 = -\frac{g\alpha}{\rho_0 c_p} Q_0 + g\beta(E - P)S_0, \tag{1.5}$$

where α and β are thermal expansion and haline contraction coefficients, c_p is the specific heat of water, Q_0 is the net surface heat flux, combined from incoming shortwave solar radiation, net longwave radiation, latent, and sensible heat fluxes (Figure 1.2 c), and $E - P$ is the freshwater

flux in m s^{-1} (Cronin and Sprintall 2009), with S_0 the surface salinity. There was no precipitation during the experiment and stratification is set by temperature. Negative B_0 corresponds to stabilizing surface forcing (warming).

The boundary layer depth h is commonly defined as the region with active turbulent transport (Li et al. 2016) and can differ substantially from both the depth of the mixed diurnal warm layer and the deeper seasonal mixed layer (Pearson et al. 2015). For scaling in the Catalina basin, we define the boundary layer depth as the depth of the maximum vertical temperature gradient, within the depth range observed by the wave glider thermistor chain (0.31 to 8.05 m). Alternative boundary layer definitions are explored in section 1.4. A two-hour moving mean is applied to h for use in this scale analysis. The mixed layer depth in the Catalina basin was about 25 m, as determined by a density difference relative to the 10 m density equivalent to a 0.2 K temperature difference, following Boyer Montégut et al. (2004). For the offshore experiment, in the absence of an observable diurnal warm layer, the boundary layer depth is taken to be equivalent to the mixed layer depth.

To characterize observations of Langmuir circulations, the Stokes drift $\mathbf{u}_s$ is calculated from observations of the directional wave spectra from wave gliders. The leading-order expression for the full Stokes drift of a spectrum of deep-water waves (Kenyon 1969; Webb and Fox-Kemper 2011) is given by

$$\mathbf{u}_s = \frac{16\pi^3}{g} \iint (\cos\theta, \sin\theta, 0) f^3 S(f,\theta) e^{\frac{8\pi^2 f^2 z}{g}} \, \mathrm{d}\theta \, \mathrm{d}f \,. \tag{1.6}$$

Directional wave spectra $S(f,\theta)$ were estimated from the motion of the wave gliders (Colosi et al. 2023). While the low-frequency swell waves are more energetic, high-frequency wind waves contribute more to the Stokes drift and its gradient near the surface due to their increased steepness and rapid decay with depth. Wave gliders are capable of resolving frequencies of up to about 1 Hz. In fully developed seas, the directional spectra can be extended with a tail to account for the Stokes drift contribution from unresolved frequencies (Belcher et al. 2012; Lenain and Pizzo 2020). A

tail with an f^{-4} slope is fit up to wavenumber $k_n = rg/u_{*\mathrm{air}}^2$, the predicted transition between the equilibrium and saturation ranges, with $r = 9.7 \times 10^{-3}$. For wavenumbers above k_n, an f^{-5} slope is fit out to a cutoff wavenumber k_M above which the directional spectrum is assumed to be isotropic, resulting in zero Stokes drift, with $k_M = (g/u_{*\mathrm{air}}^2)e^{(\pi/2-\theta_0)/\gamma}$, $\theta_0 = 2.835$ and $\gamma = 0.48$, following Lenain and Melville (2017). The wave spectra were computed in 10-minute segments, and were rescaled to preserve variance relative to the wave glider heave timeseries. A limitation to this methodology is the inability to resolve the Stokes drift contribution from small wind waves that were above 1 Hz (shorter than $\lambda \approx 1.6$ m). In wind-wave equilibrium, the contribution of unresolved waves to the total surface Stokes drift is about 15%, although the relative importance decays rapidly with depth (Lenain and Pizzo 2020). For a fetch-limited breeze in the absence of swell, the unresolved Stokes drift contribution is much larger.

As an attempt to correct for unresolved wind waves, the Stokes drift was also calculated form a wind-based parametrization of the wave spectrum. Pizzo et al. (2019) (hereafter, P19) give the surface Stokes drift u_{s0} based on parametrization of the wave spectrum for equilibrium and saturation ranges developed in Lenain and Melville (2017). While estimates of the depth profile of Stokes drift based on the surface magnitude, such as the Phillips spectrum profile, are commonly used (Breivik et al. 2016; Breivik and Christensen 2020), we instead extend the surface Stokes drift approximation in P19 equation 11 to arbitrary depth by adding an exponential decay with depth inside the integral, giving

$$u_s(z) = 1.6 \int \phi(k) \sqrt{gk} k e^{2kz} \, \mathrm{d}k \,, \tag{1.7}$$

with the wave spectrum given by

$$\phi(k) = \begin{cases} \phi_E(k) = \frac{1}{2}\beta u_{*\mathrm{air}} g^{-1/2} k^{-5/2} & k \in (k_p, k_n), \\ \phi_S(k) = Bk^{-3} & k \in (k_n, k_M), \\ 0 & \text{otherwise}, \end{cases} \tag{1.8}$$

where k_p is the peak wave frequency, determined from the wave glider observations, while the parameters β, a constant scaling for the equilibrium range, also called Toba's constant, and B, the saturation constant, are empirically determined by Lenain and Melville (2017) to be 0.08 and 7×10^{-3} rad respectively. The contribution of low wavenumbers $k < k_p$ is ignored following Breivik et al. (2014) since the wave slopes are small, as is the contribution above the high frequency cutoff $k > k_M$. The Stokes drift magnitude calculated from this omnidirectional spectrum is reduced by 20% relative to a monochromatic wave to account for wave spreading (Webb and Fox-Kemper 2015). Our best estimate of the in-situ Stokes drift is constructed by adding the Stokes drift from the observed directional wave spectrum, integrated up to the wave glider resolution limit of 1 Hz, with a wind wave Stokes drift from the P19 parameterized spectrum, integrated between 1 Hz and the isotropic high-frequency cutoff k_M.

For computational efficiency in the LES run, the Stokes drift is prescribed entirely from the parameterized wave spectrum. To better match the observed wave spectra in fetch-limited winds across the full frequency range, we rescale the parametrization constants to $\beta = 0.048$ and $B = 2.4 \times 10^{-3}$, as a given wind friction predicts too much low-frequency energy, and much of the wind energy input goes into growing surface waves rather than breaking-driven dissipation. Furthermore, k_p is set to a constant $k_p = 0.036 = 2\pi/173$ m to simplify inputs to the LES run. We assume the wave direction to be the same as the wind direction, removing any misalignment effects between wind waves and the remote swell in the LES.

Figure 1.4 compares the Stokes drift calculated from (1) the uncorrected omnidirectional spectrum from wave glider observations, (2) the observed directional spectrum with a tail correction out to isotropic wavenumbers, (3) the observed directional spectrum with additional wind waves above 1 Hz from the P19 wind-based parametrization, and (4) the adjusted P19 parameterized wave spectrum, used for the LES run. The average Stokes drift profiles for the observation period agree well, with the wind parametrizations larger than observation near the surface due to the added wind wave contribution. During low wind conditions, the surface stokes drift u_{s0} timeseries agree, but the wind-based parametrizations respond more rapidly to the

changing wind forcing. At around 2130 UTC, the addition of parameterized wind waves to the observed waves results in a 3x larger surface stokes drift versus direct observations.

Phase diagrams characterizing the relative importance of wind, wave, and buoyancy forcing have been constructed by Li et al. (2005), Belcher et al. (2012), and Li et al. (2019), who find that open-ocean fully developed sea states typically correspond to a wave-driven upper ocean with $\mathrm{La}_t \approx 0.3$. To contextualize our study, we plot the distribution of observations in the $\mathrm{La}_{\mathrm{SL,proj}}$ versus Λ parameter space (Figure 1.5) following Chor et al. (2021). In the Catalina experiment on 20 November the buoyancy flux is strongly stabilizing until about 1830 UTC when the wind increases at the location of the wave glider. At about 2315 UTC the buoyancy stability changes sign to convectively cooling ($\Lambda > 0$), but does not dominate over Langmuir turbulence. During the offshore experiment, wind and wave forcing was much greater.

An alternative to regime diagrams is constructed by Gargett (2022) using the surface buoyancy flux and LC growth rate g_*,

$$g_* = \left[\left\langle \frac{\mathrm{d}u_s}{\mathrm{d}z} \right\rangle_{\mathrm{SL}} \frac{u_*}{h} \right]^{1/2}, \tag{1.9}$$

where we have chosen to use the surface-layer average Stokes drift shear (from 0 to $0.2h$) rather than the shear at a fixed depth (Gargett and Grosch 2014). The forcing space highlights the peak in the combined wind and wave forcing in the Catalina experiments coincident with the onset of the sea breeze (Figure 1.5 c). Indeed, as we see later this peak is coincident with the fastest deepening of the diurnal warm layer. In the offshore region, the LC growth rate is largest at the wind peak, when we observe mixed layer deepening. Despite the stronger wind and wave forcing, the LC growth rate was smaller than in the Catalina basin because of the deeper boundary layer and the larger relative contribution of longer waves, which reduced the Stokes drift shear. We understand the regime diagrams and forcing space diagrams to be complimentary. While the regime diagrams are useful in understanding the dominant contribution to turbulent processes, the forcing space diagrams are more predictive of the effect of forcing one expects to observe.

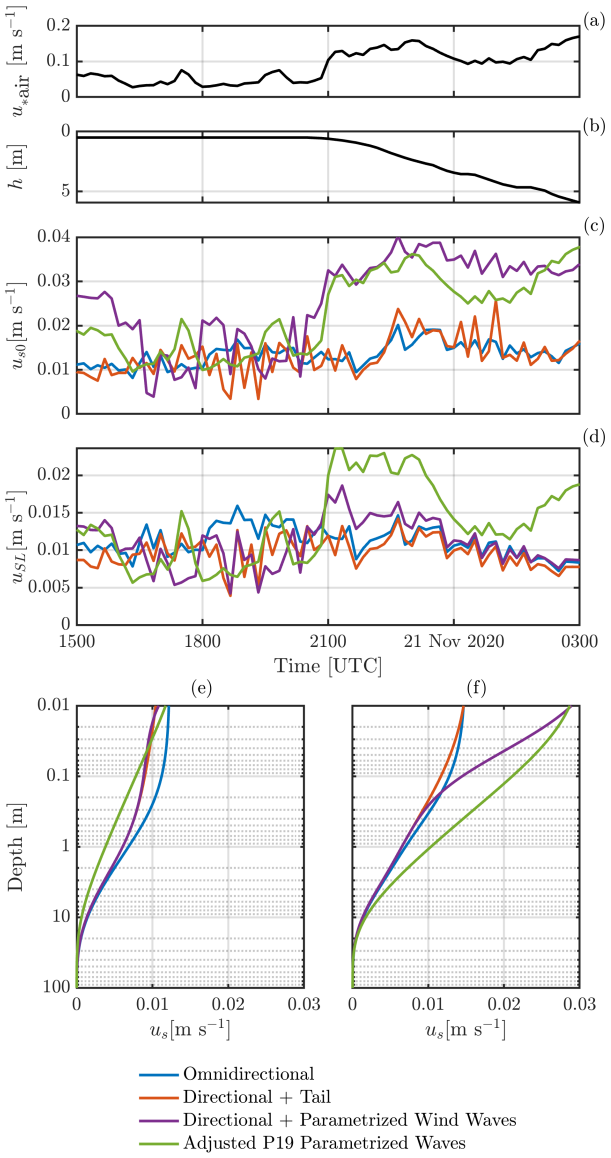

Figure 1.4. Timeseries of (a) wind friction velocity in air $u_{*\mathrm{air}}$, (b) boundary layer depth h, (c) Stokes drift at the surface, and (d) the surface-layer average Stokes drift. (e) Stokes drift profiles averaged over the low-wind period from 1500 UTC to 2030 UTC 20 Nov 2020 and (f) the high-wind period from 2130 UTC 20 Nov to 0300 UTC 21 Nov 2020. Stokes drift is computed from (blue) the observed omnidirectional wave spectrum, (red) the observed directional wave spectrum with added high-frequency tail, (purple) the observed directional wave spectrum with wind waves from the P19 parametrization, used to compute the Langmuir number in Figure 1.5, and (green) the tuned P19 wind-based parametrization used in the LES run.

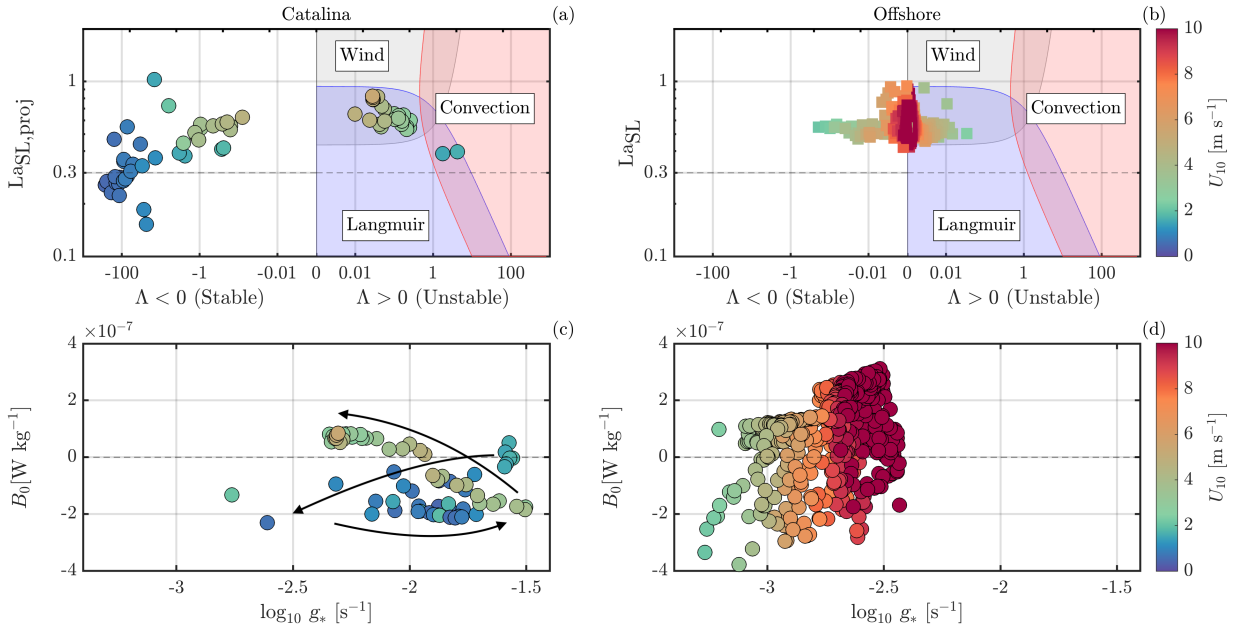

Figure 1.5. Scale analysis of the forcing in (left) the Catalina basin and (right) the Offshore experiment, shown as a scatter plot of 10-minute binned observations, colored by the 10-meter wind speed. (a,b) The non-dimensional parameter space $La_{SL,proj}$ vs. Λ The x-axis is divided into regions of stable buoyancy forcing on the left ($\Lambda < 0$) and unstable convective forcing on the right ($\Lambda > 0$). For unstable buoyancy forcing, colored regions show where a forcing mechanism contributes at least 25% of TKE production, for wind (gray), wave (blue) and convective (red) forcing for the parameter space La_t vs. Λ. The dashed line traces the wind-wave equilibrium at $La_t = 0.3$. These characterizations of the parameter space have not been rescaled to account for the difference between using the surface value of Stokes drift instead of the surface layer average. The plot is logarithmic except in the region $|\Lambda| < 0.01$, where the x-axis is linear. (c,d) Forcing parameter space B_0 vs. g_*. Arrows in (c) indicate the time progression of forcing, from morning wind bursts, to stabilizing heating with low winds, to the onset of wind, and the transition to nighttime convection. Timeseries of the forcings are provided in the Appendix (Figure A.2).

1.2.4 Large-eddy simulation

A large body of work uses large-eddy simulations to study Langmuir turbulence (Skyllingstad and Denbo 1995; McWilliams et al. 1997; Skyllingstad et al. 2000; Tejada-Martinez and Grosch 2007; Kukulka et al. 2009; Van Roekel et al. 2012; Sullivan and McWilliams 2017; Wang and Kukulka 2021a). LES is a model that resolves motions of a low-pass spatial filter of the Navier-Stokes equations while parametrizing small-scale turbulence motions (Smagorinsky 1963; Deardorff 1970; Moeng 1984). In the case of LES for LT, the equations are temporally averaged over irrotational surface gravity waves and include a CL vortex force (McWilliams et al. 1997). Simulations can either be idealized, to study specific physical processes, or forced with realistic conditions, to study real-world behavior of LT and compare with observations (Kukulka et al. 2009; Fan et al. 2020).

The LES setup used here is based on the NCAR model used in Sullivan et al. (2012). Lateral boundaries are periodic, with prescribed momentum and density fluxes at the surface and outward wave radiation with zero stress at the bottom. Unresolved subgrid scale motions (SGS) are parameterized following Deardorff (1970) and Sullivan et al. (2007). The domain size is 300 m x 300 m x 50 m, with 1024 x 1024 horizontal grid cells and 128 vertical levels, giving lateral spacing $\Delta x = \Delta y = 0.29$ m and varying vertical spacing from $\Delta z = 0.08$ m at the surface, to 1.12 m at the bottom, with the top grid cell at 0.0375 m and the bottom at 49.435 m depth. The model may be under-resolved for the Stokes drift shear from the shortest wind waves, which have cm-scale e-folding depth. The model uses an adaptive time stepping scheme with a time step chosen to maintain the CFL condition, which ranged from a maximum of about 4 seconds to a minimum of around 1 second for the more energetic periods.

The LES model requires a subgrid scale parametrization for turbulent length scales smaller than the mixing length l. The mixing length depends on the grid spacing and the stability of the boundary layer. For an unstable or neutral boundary layer, then l is simply a measure of

the mean grid spacing,

$$l_{\text{unstable}} = \Delta = (\Delta x \Delta y \Delta z)^{1/3}. \tag{1.10}$$

For a *stable* boundary layers, however,

$$l_{\text{stable}} = 0.76 \frac{e^{1/2}}{N}, \tag{1.11}$$

which depends upon the Brunt-Väisälä frequency N and the SGS turbulent kinetic energy e. To capture turbulence scales below the filter scale l, the evolution of the SGS turbulent kinetic energy is given by an advection diffusion equation

$$\partial_t e + (\mathbf{u} + \mathbf{u}_s) \cdot \nabla e = S_s + S_b + S_d - \epsilon, \tag{1.12}$$

where S_s is the shear production of turbulence, S_b is the buoyancy production, $S_d = \nabla \cdot (\nu_m \nabla e)$ is the TKE diffusion, and ϵ is the viscous dissipation (Sullivan et al. 2016). To close the evolution equation for e, the dissipation ϵ needs to be parameterized in terms of e and the mixing length. This is modeled as

$$\epsilon = \left(0.19 + 0.5 \frac{l}{\Delta}\right) \frac{e^{3/2}}{l}. \tag{1.13}$$

Two LES model runs are presented here: an idealized run, to study the onset of LCs in section 1.3, and a realistic run forced from observations to study the growth of LCs during boundary layer deepening in section 1.4. The initialization and forcing of the runs is detailed in their respective sections. In both runs, wave forcing is included through a parameterized Stokes drift profile based on the observed wind friction (Figure 1.4). Radiative heating in the model is only applied at the top grid cell. The sensitivity of model response to radiative heating and attempts to correct those effects are described in later sections. In brief, confining heat flux to the top grid cell results in higher temperature and stratification than observations. A better parametrization for the radiative forcing (see Pham et al. 2023) is needed to address the

significant sensitivity in the LES model presented here, but its implementation is beyond the scope of this work.

1.3 Onset of Langmuir Circulations

1.3.1 Fetch-limited wind forcing

On the morning of 20 November 2020, between 1700 and 1800 UTC (0900 to 1000 local time), aircraft transects were performed over the experiment region (Figure 1.6 a). Wind speed along the flight track is determined from mean square wave slope observations (Lenain et al. 2019). The plotted wind direction along the flight track is computed spectrally from the orientation of the observed Langmuir cells in the infrared imagery, where they are present. On the eastern side of the experiment region, winds were up to 3 m s^{-1} towards the south-west. Further west, wind speeds decreased to less than 1 m s^{-1} and rotated towards the west. The wind pattern is indicative of a weak land breeze that was partially blocked by Catalina Island, forming a wind shadow over the experiment region.

1.3.2 Airborne infrared observations

Sea surface temperature was collected in transects across the experiment region using an airborne infrared camera (Figure 1.7). In areas of low wind speeds (< 1 m s^{-1}) the sea surface exhibited large-scale incoherent convective patterns (Figure 1.8 a,b) broadly attributable to surface renewal processes (Gargett et al. 2004). In regions of moderate winds of 1 - 2 m s^{-1}, Langmuir cells started to appear (Figure 1.8 c). Narrow bands associated with convergent and downwelling regions are colder than the broader upwelling areas. This pattern is attributed to the convergence and thickening of the surface cool skin above the downwelling sites while warmer water from the shallow warm layer is upwelled to areas of surface divergence, resulting in a thinner and thus relatively warmer skin temperature (Marmorino et al. 2005). The cells first appear in patches of about 50 m in diameter, interspersed between areas of uniformly colder surface temperature

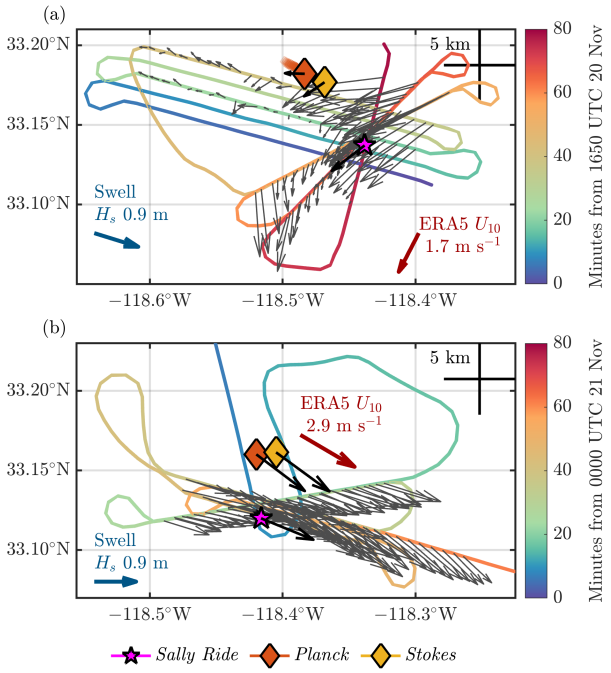

Figure 1.6. Flight track of aircraft transects and positions of assets with wind vectors for (a) the morning flight during a weak land breeze and (b) the afternoon flight during the stronger sea breeze. The width of the flight track shows the area imaged by the IR camera, and is to scale geographically. Arrows indicate wind velocity. Light gray arrows are the 10-meter wind magnitude derived from the mean-squared wave slope using airborne LIDAR, with wind direction reconstructed from the orientation of Langmuir cells, where they are present. Bold black vectors are 10-meter winds derived from direct observations of wind speed from meteorological instruments on the wave gliders and *Sally Ride*. The red arrow is the ERA5 reanalysis 10-meter wind, interpolated to the center point of the experiment region. The blue arrow indicates the peak wave direction.

(Figure 1.7 b,c,d). Within patches of LCs, temperature streaks have a cross-cell spacing of about 2 m (Figure 1.8 d). In regions of winds at 3 m s^{-1} the cells become more organized and uniform, with few patches of interruption, and are spaced by about 5 m (Figure 1.8 e,f).

Spatial inhomogeneity of LC onset

For initial wind forcing, the surface signature of LCs appears non-uniformly. A close-up of one composite IR frame (Figure 1.9) highlights the sharp contrast between a cold patch of unbroken cool skin and streaked temperature signatures of LCs around it, with an especially sharp contrast on the downwind side of the cold patch.

Thermal signatures of surface gravity waves with about 10 m wavelengths can be seen within the cold patch. The temperature signal of surface waves is likely due to mechanical straining of the surface (Veron et al. 2008b). Rapid distortion theory (Teixeira and Belcher 2002) predicts that for a sufficiently weak surface turbulence field, orbital wave motions can become the dominant surface strain signal, stretching and contracting the surface skin. Stretching of the cool skin in wave troughs would result in positive temperature anomalies as slightly warmer cool skin water comes to the surface. In areas where LCs have developed, turbulence is higher, obscuring the surface wave temperature signal. These may be the first ocean observations showing the contrast between two regimes of surface straining.

The dampening of turbulence and signature of relatively long surface waves in regions of unbroken cool skin layers is suggestive of theory by Longuet-Higgins (1996) describing the exclusion of shorter wavelength surface waves in regions of convergence and downwelling. If large-scale incoherent temperature structures seen at low wind speeds (Figure 1.7 a) correspond to convective patterns, with convergent regions having colder, thicker cool skin, then shorter and steeper wind waves, responsible for the onset of LCs, may be excluded from the colder convergent regions. The stronger near-surface Stokes drift of shorter waves would drive LCs to first appear away from cold patches. This pattern of LCs at their onset is also reminiscent of laboratory experiments by Veron and Melville (2001) showing larger wave slopes in regions of warmer

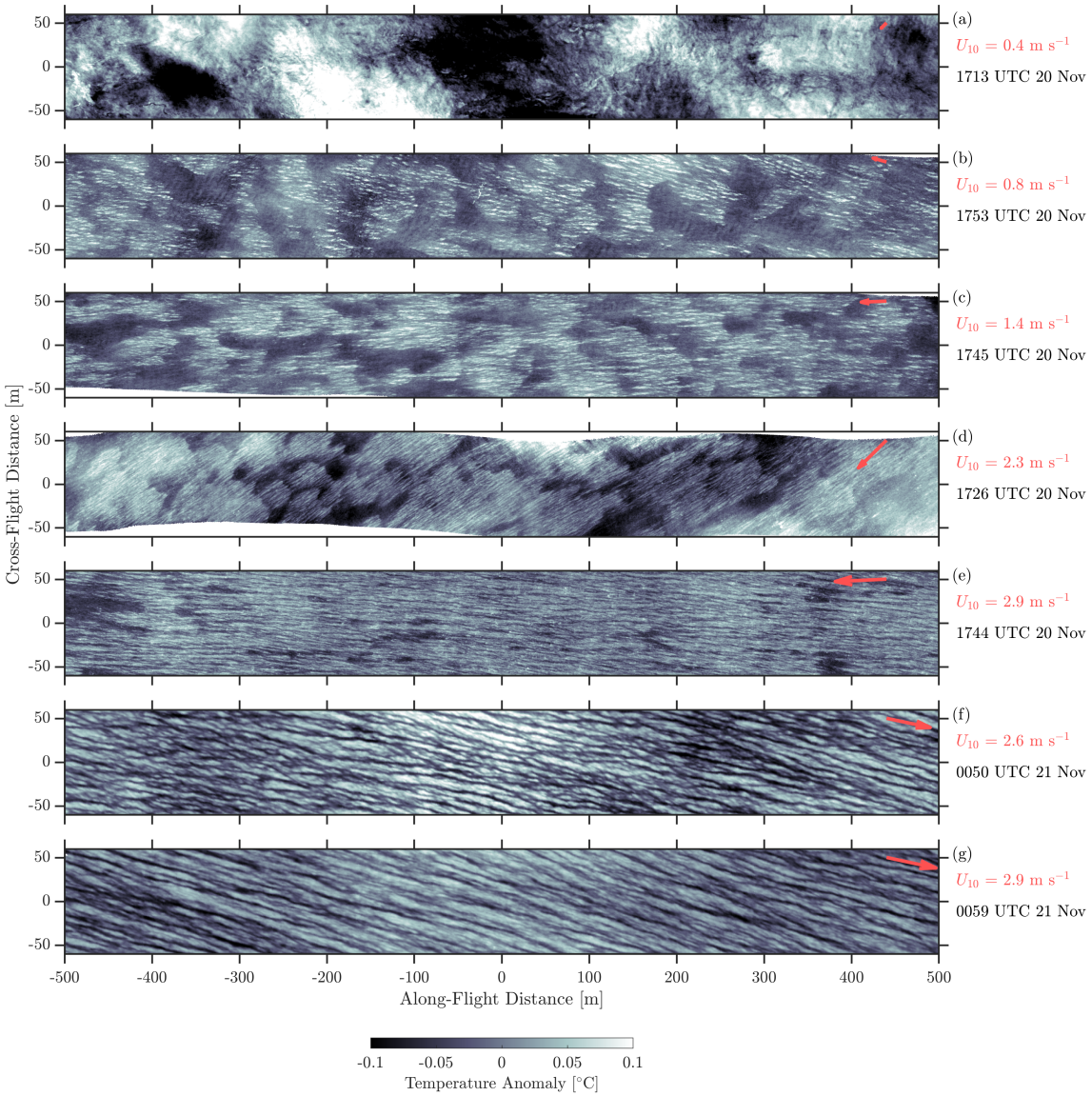

Figure 1.7. Surface temperature from transects of airborne infrared imagery. (a) Before the onset of wind, temperature is characterized by large-scale structures and convective turbulence. (b,c,d) The onset of wind forcing leads to the appearance of Langmuir circulations, interspersed with unbroken patches of colder surface skin. (e) Under stronger wind forcing, cold patches disappear and the LC field homogenizes. (f,g) After several hours of sustained wind forcing and mixed layer deepening, LCs have formed larger, coherent streaks. The temperature anomaly is relative to the 2-D plane fit of temperature to each panel, to remove background variations in temperature across the survey region. Areas of surface convergence and downwelling appear as negative temperature anomalies due to the convergence and thickening of the cool skin layer (Marmorino et al. 2005). Red arrows indicate wind magnitude, determined from mean square wave slope in each panel (Lenain et al. 2019), with flight-mean directions -150° (a-e) and -28° (f,g) obtained from nearby wave glider observations.

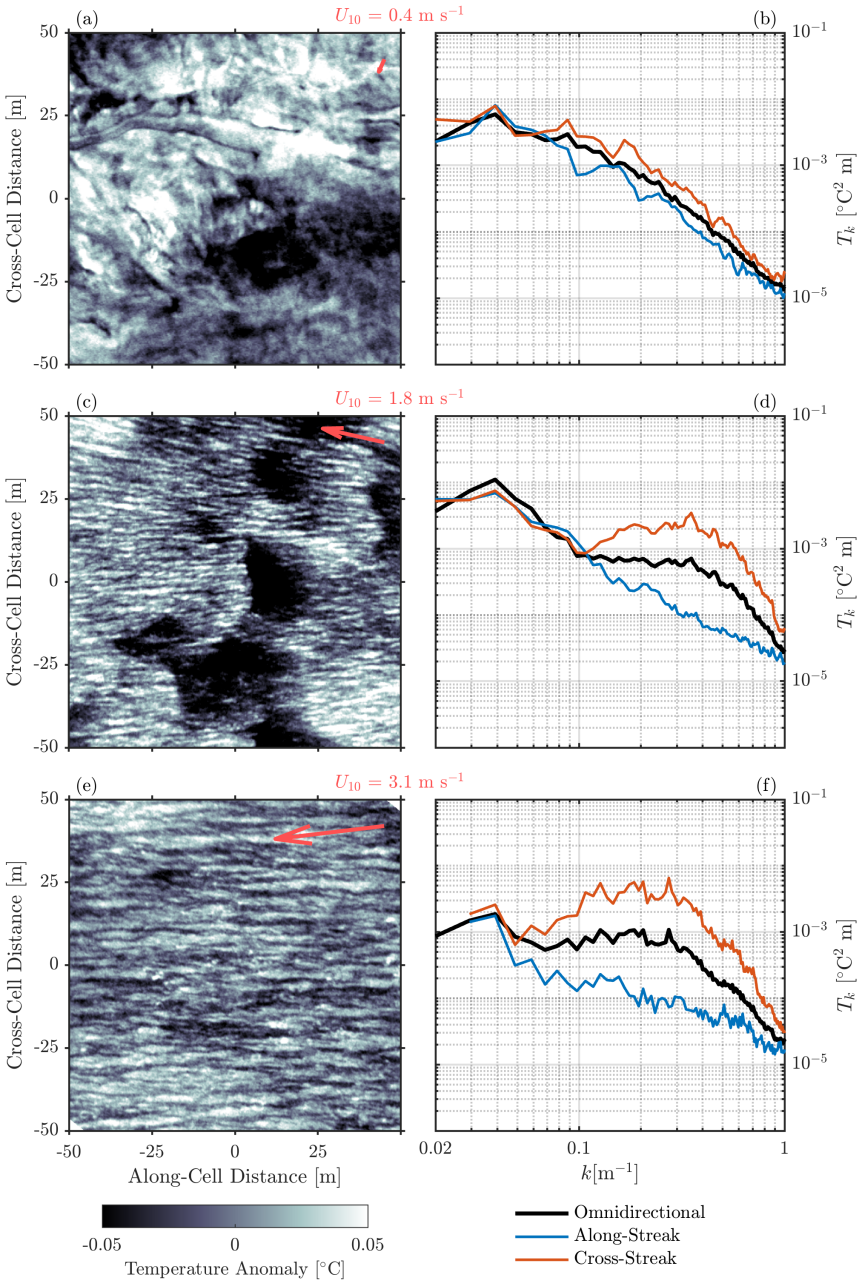

Figure 1.8. Representative samples of surface temperature from the airborne IR camera for (a) low winds with no LCs, (c) the onset of LCs, and (e) organized LCs at moderate wind speeds. The associated temperature wavenumber spectra (b,d,f) compare the (black) omnidirectional spectrum with the (red) cross-cell and (blue) along-cell components. Temperature anomaly is relative to the 2-D plane fit of temperature in each panel. Red arrows indicate wind magnitude, determined from mean square wave slope in each panel (Lenain et al. 2019), with flight-mean direction -150° obtained from nearby wave glider observations.

temperature at the onset of LCs. A conceptual schematic of our understanding of this process is shown in Figure 1.10. Note that these observations occur during a period of stabilizing surface buoyancy flux, so conventional depth scaling for possible convective patterns does not apply. We hypothesize that a mechanism for near-surface convective patterns during daytime heating comes from the balance between heat loss at the surface from latent cooling heat flux and outgoing longwave radiation with more distributed heating from incident shortwave radiation. For typical daytime values of surface heat loss (100 W m^{-2}) and shortwave radiation (500 W m^{-2}), the net buoyancy flux, computed from the double exponential irradiance model of Paulson and Simpson (1977), is destabilizing to $O(0.1$ m) depths, which would suggest the formation of near-surface convection to those depths. The Stokes drift e-folding depth $\delta = \lambda/(4\pi)$ of short $O(\lambda = 1$ m) wind-waves is similarly $O(0.1$ m), which would suggest the ability of this near-surface convection to influence the waves. Other processes that might lead to inhomogeneous appearance of LCs include atmospheric turbulence that creates variability in the wind field or surface buoyancy flux, and the clumping of surfactants in convergence regions, causing dampening of very short waves. The patchy appearance of LCs warrants further study of the coupled feedback between wave-forced turbulent instability and the wave field (Wagner et al. 2023).

Sea surface temperature wavenumber spectra

To quantify the evolution of LC scales, temperature wavenumber spectra are constructed for the composite images (detailed in Appendix A). The temperature spectra are separated into their cross-cell and along-cell components (Figure 1.8 b,d,f). This spectral procedure is repeated over 733 independent square segments of IR images, and the resulting spectra are binned by wind speed (Figure 1.11). At low wind speed, before the appearance of LCs, the temperature wavenumber spectrum is isotropic and closely follows a k^{-2} slope. As winds increase, temperature variance is enhanced in the cross-wind direction, starting at 2 m scales and growing to 5 m scales. As the peak of the cross-wind variance grows, we see a simultaneous decrease in along-wind variance. We interpret this spectral signature as the stretching of temperature features in the

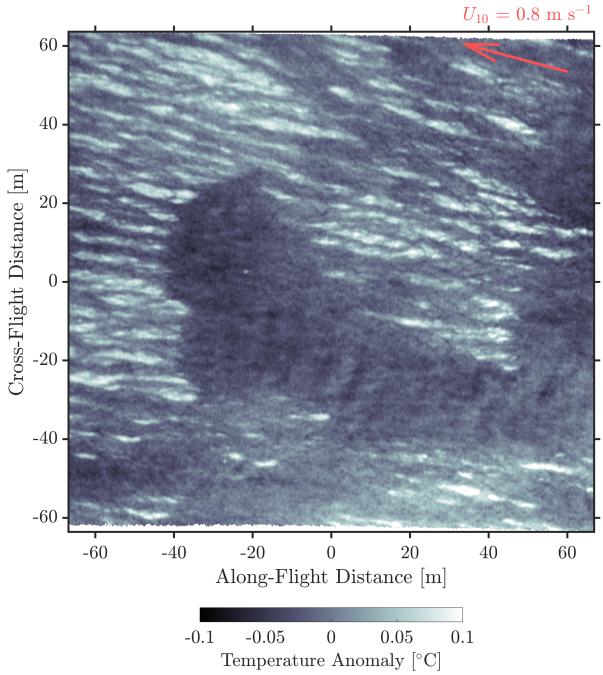

Figure 1.9. Composite IR camera frame showing the sharp contrast between regions with LCs and a patch of unbroken cool skin. Wind (red arrow) is oriented towards the top left, with magnitude derived from mean square slope and flight-mean direction -150° obtained from nearby wave glider observations. The signature of surface waves with about 10 m wavelength oriented in the direction of the wind can be seen in the cold patch. Temperature anomaly is relative to the 2-D plane fit of temperature.

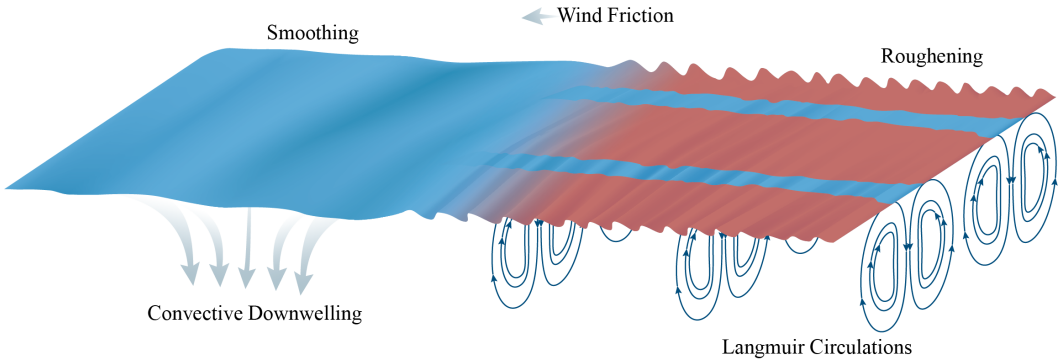

Figure 1.10. Conceptual schematic showing the spatial filtering effect of a convective downwelling region on surface gravity waves, leading to a suppression of high-wavenumber waves within the convective region, and enhancing high-wavenumber energy outside the patch. The higher near-surface Stokes drift outside of the downwelling region leads to earlier onset of Langmuir circulations.

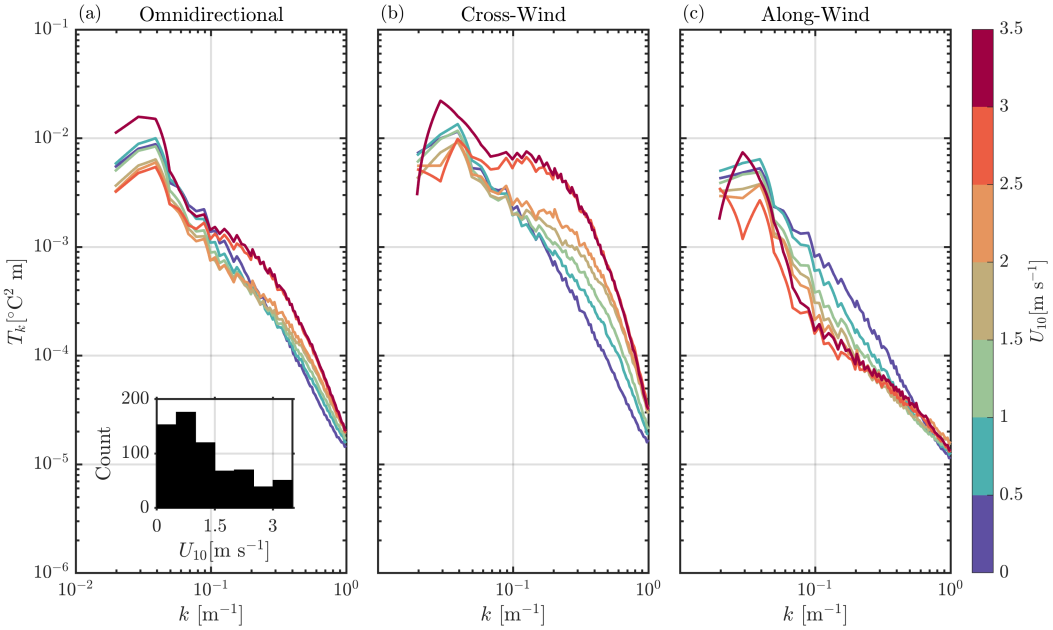

Figure 1.11. Spectra of observed sea surface temperature in the (a) omnidirectional, (b) cross-wind, and (c) along-wind directions, binned by wind speed. The inset shows a histogram with the number of spectra in each wind bin.

along-wind direction, emphasizing gradients in the cross-wind direction. At 5 m scales, this redistribution of spectral power results in a 7x increase in cross-wind power and a 3x decrease in along-wind power over the growth from 0 to 3.5 m s^{-1} winds.

1.3.3 Comparison with idealized LES

The observed dependence of temperature spectra on wind speed is compared with the appearance of LCs in an idealized LES run (Figure 1.12). The idealized run is initialized with zero velocity and uniform 17.3 °C temperature, and forced with a constant 90 W m^{-2} heat flux at the top grid cell, representative of the heating leading up to the morning observations. Wind forcing is ramped using a tanh function from 0 to 3.5 m s^{-1} over the course of an hour. An attempt was made to use distributed shortwave forcing (Paulson and Simpson 1977), which resulted in a deeper initial boundary layer with reduced stratification, but this configuration did not show the appearance of LCs during wind forcing. We attribute this to overly-active convective instability in the model, which is introduced by the surface cool skin.

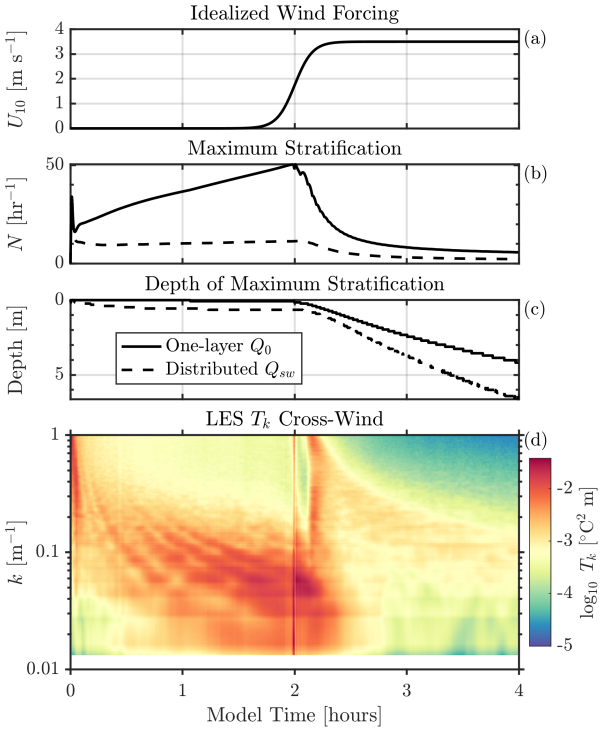

Figure 1.12. (a) Idealized wind ramp from 0 to 3.5 m s^{-1} used in the idealized LES run. (b) Maximum stratification and (c) the depth of the stratification maximum from (solid) the one-layer heat flux model and (dashed) distributed shortwave model. (d) Cross-wind spectra of temperature from the surface grid cell from the one-layer heat flux run. The sharp variance peak at 2 hours into the run is attributed to insufficient vertical resolution during the most highly stratified time window.

Figure 1.13 shows x-y snapshots of temperature in the top grid cell and the associated horizontal spectra of temperature, analogous to the observations in Figure 1.8. Note that that the colormap for LES temperature is inverted; since the LES does not have a cool skin, we expect divergent upwelling regions to have negative temperature anomalies and convergent downwelling regions to have positive temperature anomalies. At low wind speeds, the model shows random temperature fluctuations associated with incoherent turbulence. Organized streaks associated with LCs first appear in the LES at larger wind speeds than in observations, and they appear at much smaller scales, likely due to the shallower warm layer. We attribute the increase in cross-streak temperature variance and decrease in along-streak variance at 1 m length scales in Figure 1.13 (d) to early LCs. The peak in the cross-cell spacing at this early stage in their evolution may be at scales smaller than 1 m that are poorly resolved. As the wind continues to ramp, the peak in the cross-wind spectra shifts to lower wavenumber, as in the observations (compare Figure 1.8 f with Figure 1.13 f). Coherent streaks are visible in the surface temperature of Figure 1.13 (e), but their along-wind coherence appears to be shorter than in observations. In upwelling (cold) regions, temperature patterns appear to more strongly resemble convection, possibly associated with overly-active model convection.

1.4 Growth of Langmuir circulations and diurnal warm layer deepening

1.4.1 Afternoon sea breeze

Following the morning land breeze, winds decreased and generally remained under 1 m s^{-1} during the day, while solar heating continued to stratify the shallow diurnal warm layer. On the afternoon of 20 November 2020, a northwesterly sea breeze ramped wind speeds from 1 to 4 m s^{-1} over 15 minutes, after which winds remained at a consistent 2 - 3 m s^{-1} for several hours into the evening. The wind direction was towards the south-east through the channel, aligned in the same direction as the swell (Figure 1.6 b).

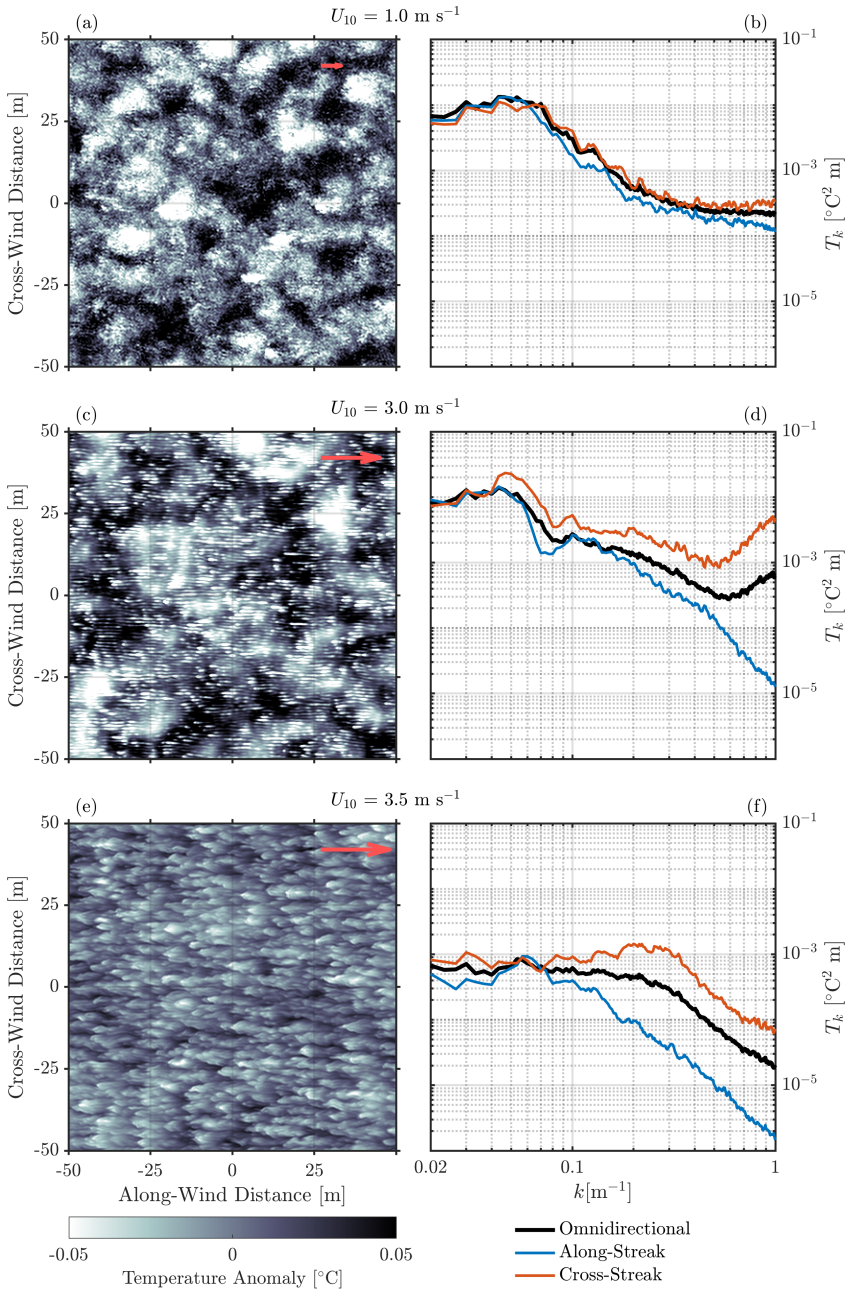

Figure 1.13. (a,c,e) Representative samples of surface temperature from the idealized LES and (b,d,f) the corresponding temperature wavenumber spectra, with omnidirectional, along-cell, and cross-cell components. Note that the colormap has been inverted relative to plots of observed surface temperature to preserve the interpretation of dark areas being associated with downwelling. Temperature anomaly is relative to the 2-D plane fit of temperature in each panel. Wind forcing is oriented in the positive x-direction.

Over the duration of these sustained winds, the diurnal warm layer was observed to deepen from 1 to 5 m (Figure 1.14). To quantify the deepening rate we compute two measures of the diurnal warm layer depth (DWLD). One estimate is based on the depth of the maximum stratification, H_N, computed from the temperature gradient on the wave glider T-Chain. The deepening rate from 2100 to 0200 UTC, as determined by the depth of the maximum stratification, averaged 1 m hr^{-1} (Figure 1.18). Our ability to quantify the strength and depth of the DWL is limited by the vertical spacing of temperature measurements. The CTD on the wave glider surface platform recorded temperature at 0.31 m depth, while the shallowest thermistor on the wave glider T-Chain was installed at 0.70 m relative to the surface, meaning that DWLD shallower than 0.7 m could not be resolved. Until the onset of wind, the maximum stratification was recorded between the CTD and the shallowest thermistor, reaching a maximum value of 40 hr^{-1}. Another estimate of DWLD is defined by the potential energy anomaly, H_ϕ, following Reichl et al. (2022) and Wang et al. (2023). To emphasize the shallow warm layer depth, we choose $\phi = 0.3$ J m^{-1}, which matches the two depth estimates towards the end of the observations, but results in an overestimate of DWLD for $H_N < 2$ m.

1.4.2 Airborne infrared and subsurface observations

After three hours of sustained winds at 3 m s^{-1}, an aircraft flight from 0000 to 0100 UTC 21 November observed coherent Langmuir circulations throughout the experiment region (Figure 1.7 f,g). Cross-cell scales were about 15 m throughout the experiment region (Figure 1.15 a,b), roughly 2.5 times the depth of the shallow warm layer at that time, whose maximum stratification had decayed to 10 hr^{-1} (Figure 1.18).

The T-chain on the wave gliders can provide a subsurface view of lateral and vertical LC scales. To convert time from the thermistor record to distance, the vehicle's position over ground and the relative ocean velocity from the upward-looking ADCP are combined to calculate the distance through water, projected onto the cross-wind direction. Figure 1.16 shows the observed temperature relative to the cross-wind distance, along with the backscatter intensity from the

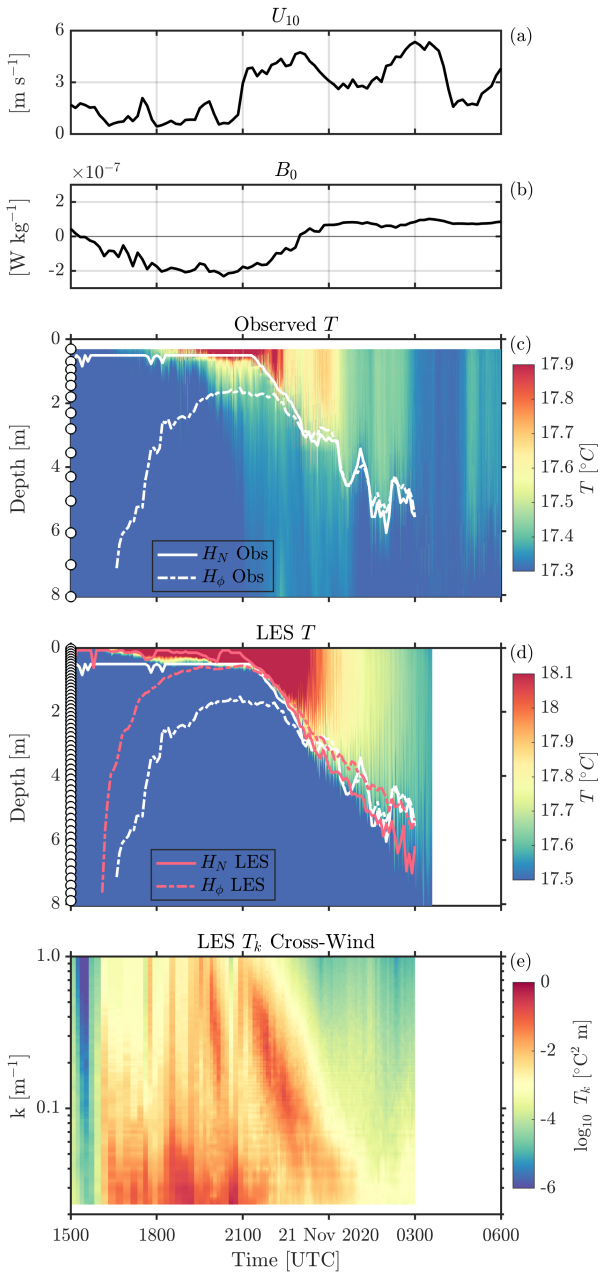

Figure 1.14. Observed (a) 10-meter wind speed and (b) surface buoyancy flux. (c) The evolution of temperature in the boundary layer as seen by wave glider *Planck* compared to (d) LES at its center point. (e) LES cross-wind surface temperature wavenumber spectrogram. The temperature range is 0.6 °C in both (c) and (d). The solid (dashed) line indicates the depth of the maximum stratification (depth of ϕ = 0.3 J m^{-1}) with a 1-hour moving mean for the observations (white) and LES (red). Thermistor spacing in observations and grid spacing in LES is indicated with white circles on the y-axis.

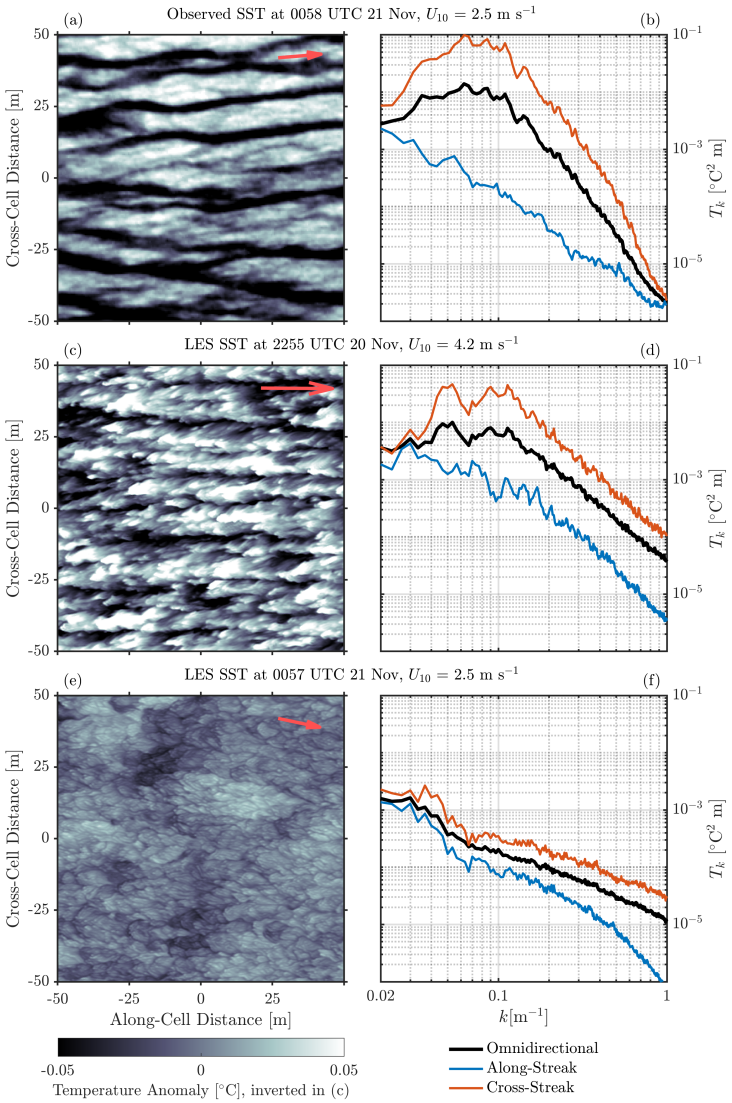

Figure 1.15. (a) Surface temperature from airborne IR observations during the afternoon aircraft transects after several hours of sustained wind forcing and mixed layer deepening. (c,e) LES temperature at the top grid cell, with (c) during mixed layer deepening and towards the end of stabilizing buoyancy forcing, and (e) at the time of the observations in (a). (b,d,f) The corresponding temperature wavenumber spectra showing the omnidirectional spectrum (black), cross-cell (red), and along-cell (blue) components. Temperature anomaly is relative to the 2-D plane fit of temperature in each panel. The colormap in (c) has been inverted such that convergent and downwelling areas of temperature appear dark for direct comparison with cool-skin observations in (a). Red arrows indicate wind, where observations (a) use magnitude determined from mean square wave slope (Lenain et al. 2019) and flight-mean direction -28° obtained from nearby wave glider observations, while LES wind (c,e) is set by the forcing from wave glider *Planck*.

echosounder. Before the wind event, a shallow diurnal warm layer <1 m deep forms as a result of daytime solar heating, with small lateral gradients in temperature, and active mixing throughout, as indicated by the uniform backscatter intensity from the shallow thermocline to the surface.

During the wind event and deepening of the boundary layer, cell-like temperature structures are seen, with a spacing of about 5 m and vertical extent of around 2.5 m, consistent with pairs of LC vortices. Here we expect downwelling regions to be associated with positive temperature anomalies of warm diurnal water, while cold anomalies upwell water from the base of the boundary layer. Note that this pattern is opposite to that observed form the surface, where temperature patterns are set by LCs interacting with the cool skin. The echosounder reveals patterns of bubble entrainment up to about 2 m depth, much deeper than would be expected from only wave breaking entrainment at 3 m s^{-1} wind speeds, indicating regions of active downwelling due to LCs (Zedel and Farmer 1991b; Osborn et al. 1992; Gemmrich and Farmer 1999; Thorpe, Osborn, Jackson, et al. 2003; Thorpe, Osborn, Farmer, et al. 2003). While some downwelling regions are coincident with temperature maxima, the correlation is not absolute, suggesting that temperature cells could be leftover from previous mixing, while new downwelling regions can appear without having yet developed a temperature signature.

Finally, toward the end of the deepening period, temperature structures have broadened and deepened to reach 8 m depth. Bubble entrainment streaks are narrower and shallower than the temperature cells, limited by the bubble's buoyancy (Thorpe, Osborn, Farmer, et al. 2003). Horizontal wavenumber spectra of temperature from the T-chain record were computed, but because the glider's heading is at an angle relative to the LC orientation, and because it frequently changes, the evolution of scales with time could not be decomposed into components to compare with surface IR spectra.

1.4.3 Comparison with LES forced from observations

The realistic model run is initialized with vertical profiles of observed temperature and demeaned horizontal velocity on 1200 UTC 20 November using basin-representative profiles

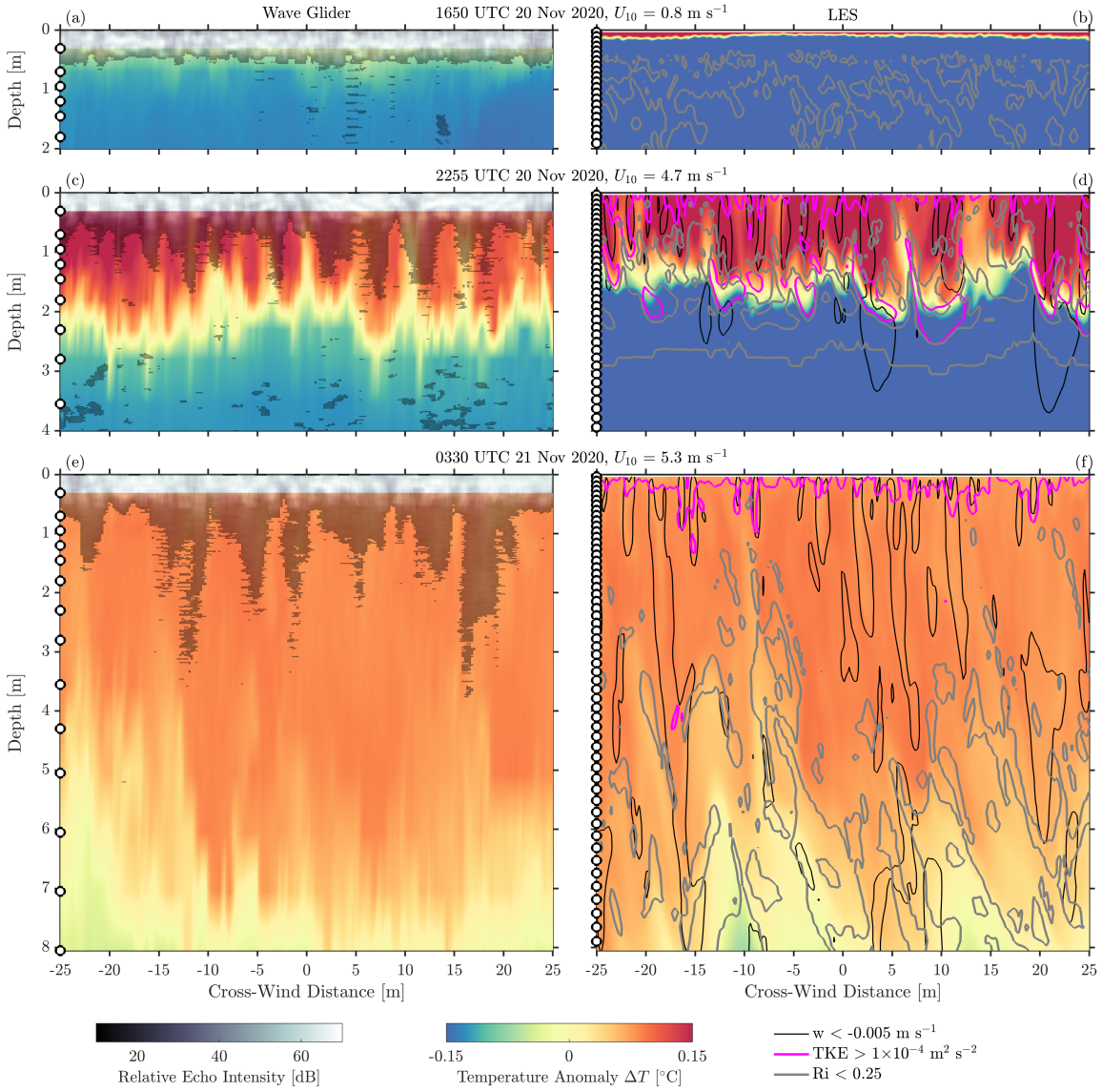

Figure 1.16. (left) Wave glider temperature and echosounder backscatter (shaded), and (right) LES temperature vs. cross-wind distance from (a,b) before the wind event, (c,d) during the wind forcing and mixed layer deepening, and (e,f) after the wind event during the transition to convective surface cooling. Temperature colors are relative to the y-z 2D mean temperature within the diurnal warm layer. The colorbar range is $\Delta T = 0.3$ °C in all plots. Backscatter amplitude in echosounder data is relative to a background attenuation. A scattering signal below the boundary layer in (c) is attributable to biological scatterers. Thermistor depths are indicated on the left axis as circles. For the LES, contours of downward vertical velocity exceeding 0.005 m/s are shown in black, contours of TKE exceeding 1×10^{-4} m^2 s^{-2} are shown in pink, and contours of Ri < 0.25 are shown in gray. Thermistor spacing in observations and grid spacing in LES is indicated with white circles on the y-axis.

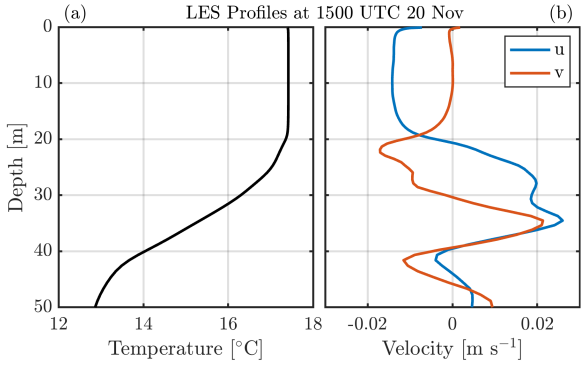

Figure 1.17. LES profiles of (a) temperature and (b) horizontal velocity, after a 3-hour spinup initialized from observations.

obtained from Wirewalker and FastCTD observations. Figure 1.17 shows profiles of LES temperature and velocity at 1500 UTC after a 3-hour spinup. Surface wind stress and buoyancy forcing are set by observations from wave glider *Planck* (Figure 1.2) while wave forcing is included through a parameterized Stokes drift profile based on the observed wind friction (Figure 1.4). Again, radiative heating was applied only at the top grid cell by setting the surface heat flux equal to the total heat flux Q_0. As a result, the modeled surface warm layer is warmer and more strongly stratified during daytime solar heating than can be resolved from the observations (Figure 1.18). An attempt to reduce incoming radiation using a scale factor of 0.63 resulted in near-surface temperature and stratification values that agreed better with observations, but the approach was rejected because DWL deepening rates diverged from observations, possibly due to the earlier onset of convective instability.

The LES initialized and forced from observations reproduces the formation of a diurnal warm layer which deepens toward the afternoon during the increase in wind forcing (Figure 1.19). Weak wind forcing drives a mean flow confined to the diurnal warm layer, known as a diurnal jet (Hughes et al. 2020). The observed values of near-critical Richardson number suggest that shear instability driven by the mean flow contributes to diurnal warm layer deepening (Gargett et al. 2014; Hughes et al. 2020). The LES shows local values of enhanced shear instability at the base of LCs (Figure 1.16), supporting previous studies of LCs enhancing shear-driven mixing

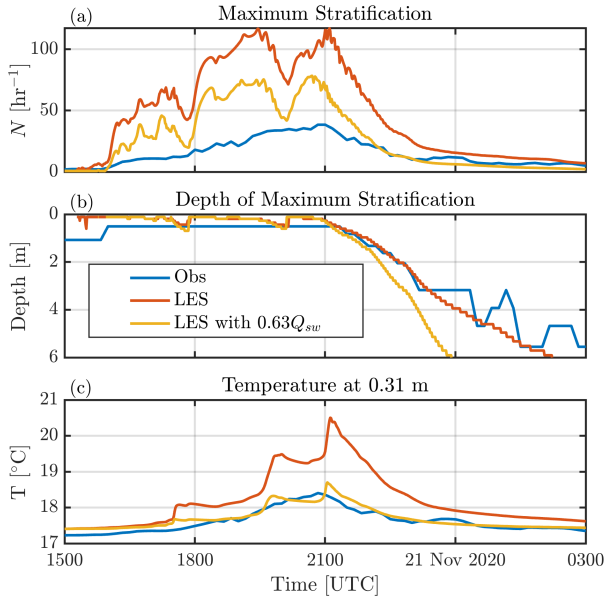

Figure 1.18. (a) The maximum stratification, (b) its depth, and (c) temperature at 0.31 m depth from (blue) observations, (red) LES with single-layer heating, and (yellow) LES with single-layer heating using shortwave flux scaled by 0.63. Note that the observed stratification magnitude is limited by thermistor spacing, particularly near the surface, where the two thermistors nearest the surface are at 0.31 m and 0.70 m depth.

through downward transport of horizontal momentum (Kukulka et al. 2010).

As in the idealized LES run, LC-like streaks appear here at the onset of wind forcing and grow in scale with sustained winds and boundary layer deepening (Figure 1.15 c). The enhanced temperature variance at small scales relative to observations might be due to insufficient model dissipation, or resolution limitations in aircraft data. Subsurface, modeled temperature structures are similar to observations, with downwelling velocity co-located with temperature maxima, and TKE maxima at the base of these structures. As surface buoyancy flux weakens and becomes convectively destabilizing, the LES experiences an abrupt shift in the subsurface temperature structure at 2335 UTC (not shown), which we attribute to overly-active convection in the model. As a result, by the time of the second flight, the LES surface temperature showed patterns of convective turbulence, with no clear directional peak in the 2D spectrum (Figure 1.15 e,f). Subsurface, downwelling regions are now associated with negative temperature anomalies, with enhanced TKE confined to near the surface.

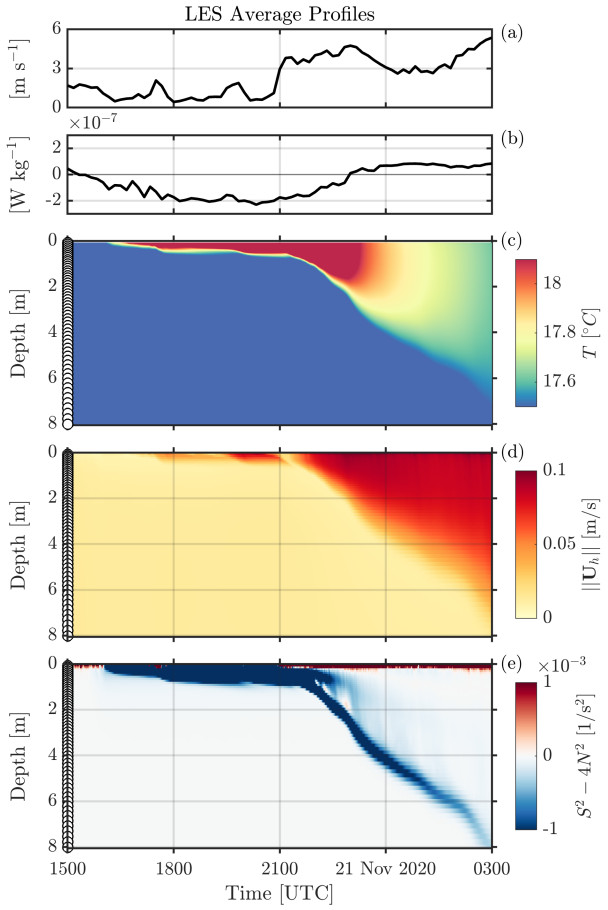

Figure 1.19. LES domain-averaged (c) temperature, (d) horizontal velocity, and (e) reduced shear. Grid spacing is indicated with white circles on the y-axis. Forcing timeseries of (a) 10-meter wind speed U_{10} and (b) surface buoyancy flux B_0 are provided for reference.

Following the methodology to identify LC scales from horizontal temperature spectra of SST in the previous section, we compute the evolution of LC scales in the cross-wind direction from snapshots of the LES at the top grid cell. The peak of the cross-wind spectrum grows from 2 m to 10 m scales over an hour and a half, during which time the wind was steady at around 4 m s^{-1} (Figure 1.14 e). Over the same period the total temperature variance also decayed by about an order of magnitude due to turbulent mixing.

1.4.4 Subsurface observations of full mixed-layer depth LCs

The observations and numerical simulations discussed so far are focused on relatively weak wind and wave forcing conditions, with a shallow warm layer which sets the stratification for the LC mechanics. In contrast, most prior observational studies of Langmuir circulations have focused on stronger wind forcing events with deep mixed layers. To contextualize our results with more energetic open-ocean conditions, we compare our measurements from the Catalina basin to those from the offshore deployment. On 6 November 2020 winds increased from 8 m s^{-1} to a maximum of 15 m s^{-1}, followed by a decay to 4 m s^{-1} by 14 November. The storm generated waves, with significant wave height increasing from 2 m on 5 November to over 5 m by 8 November (not shown). The air temperature was consistently cooler than sea surface temperature during this time, leading to predominantly destabilizing surface buoyancy forcing, except during a short daytime solar maximum. Observations made from the drifting T-chain during the offshore deployment (Figure 1.20) show patterns of temperature anomalies consistent with LC signatures seen in the Catalina experiment, but now extending down through nearly the full depth of the mixed layer. The dominant cell spacing is consistent with twice the mixed layer depth. The transition from stabilizing daytime surface heating in Figure 1.20 (c) to nighttime cooling in (d) shows the appearance of negative temperature anomaly in the upper mixed layer that interrupt the vertical coherence of the temperature anomaly associated with LCs.

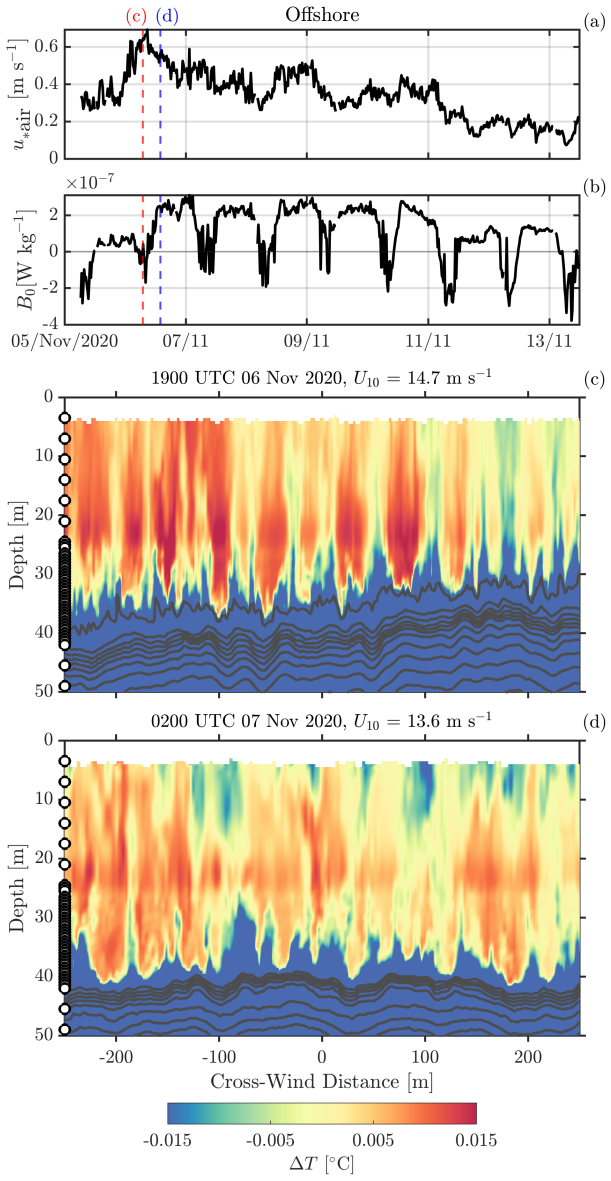

Figure 1.20. Observations of Langmuir circulations from the offshore thermistor chain. (a) Wind friction in the air and (b) surface buoyancy flux. (c,d) Temperature vs. depth and cross-wind distance, obtained from the velocity of the drifting T-Chain relative to the average mixed layer velocity from the upward-looking ADCP, scaled by the angle relative to the wind direction. The selected times in panels (c) and (d) are indicated by the red and blue dashed lines in the forcing timeseries. Thermistor spacing is indicated with white circles on the y-axis.

1.5 Summary and Discussion

We present novel observations of Langmuir circulations collected simultaneously from an airborne instrument (SIO MASS) and autonomous surface vehicles. During a morning fetch-limited land breeze in the wind shadow of Catalina Island, with weak remote swell and stabilizing surface buoyancy forcing, we observe the appearance of LCs at wind speeds of about 1 - 2 m s^{-1}, in agreement with previous observations of conditions under which Langmuir circulations appear and diurnal warm layers begin to deepen (Weller and Price 1988; Hughes et al. 2020). A strongly stratified diurnal warm layer with a depth shallower than 0.7 m constrained LCs to appear at cross-cell separation scales of about 2 m, as determined from 2D wavenumber spectra of surface temperature.

The onset of LCs is non-uniform in space and is characterized by patches of relatively uniform, colder water in between regions with LCs. We hypothesize that underlying convective structures within the diurnal warm layer induce a filtering effect on the early wind wave field, excluding shorter and steeper wind waves from surface convergence zones (Longuet-Higgins 1996), thereby delaying the onset of LCs due to the reduced near-surface Stokes drift. As discussed by Wagner et al. (2023), this pattern of non-uniform LC onset suggests that wave-averaging LES models are incomplete in their treatment of LT as they cannot represent the two-way coupling between turbulent structures and surface waves.

Over several hours of consistent 2 - 3 m s^{-1} wind forcing we observe the deepening of the shallow surface warm layer at about 1 m hr^{-1} to 6 m depth, while LCs grow to cross-cell scales of about 15 m. Subsurface observations of temperature show cell-like patterns of warm temperature anomalies during the deepening of the diurnal warm layer. Echosounder backscatter records show colocated patterns of bubble entrainment, roughly consistent with the spacing and scale of the temperature anomalies. As the region transitions to destabilizing buoyancy forcing, subsurface temperature anomalies become less pronounced. Patterns of bubble entrainment at the surface remain, though at smaller than expected scales for Langmuir circulations and no

longer correlated with temperature intrusions, suggesting a transition to convective circulation. The subsurface temperature structures observed during the shallow diurnal warm layer deepening are similar in character to those seen during a much stronger wind forcing event with a deep mixed layer, a regime more representative of previous observational and LES studies of LCs.

We report the observed ocean and atmospheric forcing in terms of the non-dimensional scaling parameters $La_{SL,proj}$ and Λ to contextualize our observations in relation to prior studies. To include Stokes drift from high-wavenumber wind waves that are not resolved with wave gliders, we expand on previous work from Pizzo et al. (2019) that parametrizes the wave spectrum from wind friction by including a calculation for the depth-dependent Stokes drift profile. Adding the Stokes drift from parameterized wind waves to the Stokes drift obtained from observed directional wavenumber spectrum allows us to capture the rapid growth of the near-surface Stokes drift in response to wind forcing while preserving the swell contribution at depth. Numerous recent studies have addressed the impact of wind-wave misalignment and fetch limitation on the strength of LT (Wang et al. 2019; Wang and Kukulka 2021a; Wang and Kukulka 2021b; Wang et al. 2022). For our observations, a weak remote swell meant that the dominant contribution to the surface Stokes drift came from short wind waves, even for weak wind bursts. While we use the projected surface layer Langmuir number, (Van Roekel et al. 2012), we note that its validity breaks down under conditions when wind-waves oppose the remote swell, leading to an inversion of the Stokes drift shear in the surface layer. An alternative characterization of the system in the forcing space B_0 versus g_* (Gargett 2022) reveals the large LC growth rate associated with the onset of wind forcing in the Catalina observations, and relatively weaker LC growth in the offshore experiment, despite the stronger wind-wave forcing.

Observations of LC appearance and growth are compared to a large-eddy simulation run with the observed meteorological and ocean forcing. The simulation reproduces the timing and rate of the diurnal warm layer deepening for the observed afternoon wind event. General similarity in boundary layer deepening is expected for the same wind forcing due to wind-driven shear instability, with the inclusion of LT serving to enhance the deepening rate (Kukulka et al. 2010;

Gargett et al. 2014). Surface temperature patterns at the onset of the wind event resemble observed LC. Due to overly-active convection in the model, however, at the time of afternoon aircraft LC observations, the model surface temperature structure is dominated by convection. Subsurface temperature patterns are generally comparable to observations, and downwelling velocity patterns are comparable to the bubble entrainment signature, with the exception of large downward velocities well below the base of the diurnal warm layer. In agreement with previous studies, TKE is enhanced at the base of downwelling structures during boundary layer deepening.

An idealized run to study the onset of LCs shows their appearance at larger wind speeds and with much smaller cross-cell scales than observations. The model appears to be sensitive to the treatment of solar radiation, which inputs heat at the top grid cell, resulting in stronger DWL stratification. Attempts to reduce the solar radiation or apply a two-term solar model with distributed shortwave heat input reduced stratification but resulted in an overactive boundary layer deepening. The treatment of solar forcing in LES, particularly for shallow diurnal warm layers, requires further investigation. We caution studies of near-surface LT in LES to scrutinize the sensitivity of their models to the implementation of radiative forcing and sensitivity to convective instability.

The relation between the depth of LCs and their cross-cell spacing is important for understanding how the surface signature of Langmuir circulations relates to boundary layer dynamical processes. While our observations of cross-cell spacing versus boundary layer depth (Figure 1.21) generally agree with the expected scaling of between 2-3 times h (Smith 1992; Thorpe 2004), we also identify several important considerations to make when applying this scaling. First, in the presence of a strong diurnal warm layer there is a large difference between the definition of the boundary layer depth that most closely relates to the dynamics of LC spacing compared to other more general mixed layer depth definitions. Our observations show the shallow diurnal warm layer deepens from < 0.7 m to about 6 m over the course of the wind forcing, while the larger-scale mixed layer depth remained constant at about 25 m. Next, it appears that the depth defined by the maximum stratification H_N better relates to the LC spacing than a definition

based on the potential energy anomaly H_ϕ. Even with a potential energy anomaly criterion tuned to reproduce the depth of the maximum stratification towards the end of the wind event, the potential energy boundary layer depth estimate overestimates the depth at the onset of deepening. At the time when LCs at 3 m scales were observed, the potential energy estimate gave a boundary depth of 3 m, while the depth of maximum stratification was shallower than 1 m. Further, the ratio of cross-cell spacing appears to be sensitive to the strength of the stratification at the base of the LCs. In the limit of shallow-water full-depth Langmuir circulations, observations of cross-cell spacing of three to ten times the water depth have been reported (Gargett et al. 2004; Marmorino et al. 2005; Gargett and Wells 2007; Kukulka et al. 2011). In our LES run, surface solar heating input at the top grid cell resulted in a stratification profile that was up to three times stronger than the observations at the onset of wind forcing. The resulting spacing of 5 times H_N over the course of the DWL deepening versus the observed spacing of about 2 times might be attributable to the stronger stratification.

Another contributing factor to the wider spacing is that turbulence in the shallow diurnal warm layer is almost entirely sustained by the subgrid turbulence model. SGS models are not designed to operate when the filter scale $l > l_O$ (Sullivan et al. 2016), where the Ozmidov scale $l_O = \left(\epsilon/N^3\right)^{1/2}$ characterizes the largest eddy that has sufficient kinetic energy to overturn. For example, during the peak daytime heating regime, SGS turbulence is generated with dissipation values $\epsilon \sim 10^{-6}$ m^2/s^3 and $N \sim 50$ hr^{-1}, leading to an Ozmidov scale of $l_O < 0.04$ m, which is well below the minimum grid spacing at the surface of $\Delta = 0.2$ m. Further increasing model resolution near the surface could improve the performance of the SGS model and therefore correct for the overly dissipative LES energetics in the upper few meters, and is a topic for future work.

This work has leveraged the capability of simultaneous multi-platform observations of the OSBL to describe the onset and evolution of Langmuir circulations. These observations offer a benchmark for future LES studies that aim to improve the representation of coherent temperature structures. The relation between diurnal warm layer stratification, coherent LC

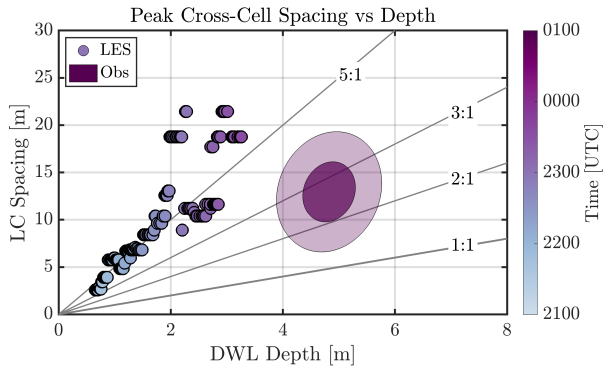

Figure 1.21. The cross-cell spacing determined from spectra of sea surface temperature from LES (scattered circles) and observations (ellipse). The ellipse gives the 1σ (solid) and 2σ (light) spread of observations of cross-cell spacing from 81 images and the range of DWL depths from three subsurface wave glider T-Chains at the same time. For large values of LC spacing in the LES, length scale resolution is limited by the wavenumber resolution in the spectra of temperature wavenumber. Lines trace ratios of spacing to boundary depth. LES values after 2335 UTC are omitted due to the model's overly-active transition to convection.

spacing, deepening rates, and LT strength across a variety of forcing regimes remains unresolved and should be explored in future studies.

1.6 Acknowledgments

Thank you to everyone at the Multiscale Ocean Dynamics group, the Air-Sea Interaction Laboratory, the Coastal Observing Research and Development Center, and the groups of William Hodgkiss and Bill Kuperman, as well as the crews of the *R/V Sally Ride* and the *R/V Bob and Betty Beyster* for the data collected during the TFO 2020 observational campaign. The illustrative schematic was produced by Jennifer Matthews. Thanks to Jerry Smith, Sutanu Sarkar, Nick Pizzo, Baylor Fox-Kemper, Bethan Wynne-Cattanach, and Pascal Polonik for guidance and productive discussions about the research. Two reviewers, an anonymous reviewer and Ann Gargett, provided constructive and instructional comments that greatly improved this paper. This research was supported by grants from ONR (N00014-19-1-2635) and NSF (OCE; Grant OCE-2219752 for LL).

All presented data are available at the UCSD Library Digital Collection Andriatis et

al. (2023, doi:10.6075/J0VQ32W2).

Chapter 1, in full, is a reprint of the material as it appears in Andriatis, Alexander, Luc Lenain, Matthew H. Alford, Nathaniel Winstead, and Joseph Geiman. "Observations and Numerical Simulations of the Onset and Growth of Langmuir Circulations." *Journal of Physical Oceanography* 54.8 (2024): 1737-1763. The dissertation author was the primary investigator and author of this paper.

Chapter 2

Observations of turbulent structures at the base of the ocean mixed layer

We report novel observations of temperature structures associated with ocean mixed layer and transition layer turbulence from a drifting thermistor chain. Following a storm featuring 15 m/s wind speeds, the mixed layer is observed to deepen from 35 to 45 m depth. At the base of the mixed layer, we observe temperature fluctuations consistent with turbulence in a stratified shear layer resulting from a mixture of Kelvin-Helmholtz and Holmboe instabilities. We examine the size and frequency of these structures in the context of the surface forcing, highlighting four distinct regimes - wind-wave dominated conditions with destabilizing surface heat loss, wind-wave forcing with stabilizing radiative heating, convectively-dominated turbulence with weak wind forcing, and a regime with stabilizing surface forcing and weak winds that supports the formation of a diurnal warm layer. For the duration of our observations, an array of drifting instruments allows us to constrain a one-dimensional energy budget. We find Thorpe scale estimates of entrainment velocity can explain the observed mixed layer deepening when averaging over the turbulent portion of the transition layer. The outer scale of the turbulent region, as characterized by the height of the reduced stratification patches in the transition layer and the heave of the top of the transition layer, is correlated to the wind forcing. This observational dataset of turbulent structures can be compared to numerical simulations to better understand the mechanisms and efficiency of mixing at the base of the mixed layer.

2.1 Introduction

The ocean surface boundary layer (OSBL) is the interface between the atmosphere and the ocean, exchanging momentum, heat, and chemicals such as carbon dioxide. The exchange between the boundary layer and the interior of the ocean is governed by turbulent processes at the base of the mixed layer, a region commonly referred to as the transition layer (TL). Here, turbulent forcing interacts with strong stratification of the upper thermocline, leading to mixing between surface waters and the ocean interior. Mixing in the TL is particularly complicated because surface forcing, such as surface wind stress, surface heating and cooling, and wave forcing (Langmuir turbulence) interacts with subsurface forcing such as shear from internal waves in the thermocline, subsurface ocean currents, and submesoscale eddies, to produce a rich variety of turbulent velocity production. This turbulent production leads to a variety of instabilities at the base of the mixed layer such as Kelvin Helmholtz (KH) billows, Holmboe (H) instability scouring, and convective plumes (Smyth and Moum 2012). Understanding the conditions under which these instabilities arise and their effect on modifying the structure of both the mixed layer and the thermocline below it is essential to accurately model the mixed layer.

A popular method to study boundary layer turbulence has been through numerical simulation, including large-eddy simulation (LES) and direct numerical simulation (DNS). In DNS, stratified turbulence has historically been modeled as a shear layer at the interface of two water masses (Smyth and Moum 2000; Peltier and Caulfield 2003). More recent work has included simulating shear layers with continuous stratification profiles (Pham et al. 2009; Watanabe et al. 2018; Sarkar and Pham 2019; VanDine et al. 2021), which show the importance of the transition layer at the edges of the shear layer, supporting a rich field of secondary instabilities during the transition to turbulence and large variations in the associated mixing efficiency. DNS is however very limited in its ability to represent the richness of stratification and shear profiles present in a real ocean, such as at the base of a mixed layer. Recent simulations by Kaminski and Smyth (2019) have shown that pre-existing turbulence in a shear layer significantly affects

the behavior of the turbulent field, limiting the growth of KH billows and reducing the mixing efficiency.

LES can provide more realism in investigating boundary layer turbulence by adding surface forcing and more complex shear and stratification profiles. As the gradient in stratification across an interface increases, the shear instability changes character from a Kelvin-Helmholtz (KH) to Holmboe (H) mode (Pham and Sarkar 2014). As the stratification below the shear interface increases, the maximum vertical scale of billows decreases and their growth rate decreases. Turbulent instability at the base of the mixed layer interacts with the stratified interior, with internal wave energy released by the instability, substantially influencing the behavior of the instability (Pham et al. 2009). Numerous recent LES studies have investigated specific boundary layer processes and their effect on turbulence such as the evolution of diurnal warm layer (Sarkar and Pham 2019; Hughes et al. 2020), the effect of Langmuir circulations (Kukulka et al. 2009; Andriatis et al. 2024), and the effect of cyclones (Reichl et al. 2016; Wang et al. 2018; Lucas et al. 2019).

While numerical simulations are well suited for studying specific turbulent dynamics, in-situ observations of turbulence in the OSBL are necessary for understanding the effects of combining a multitude of forcing mechanisms. For instance, Dohan and Davis (2011) compare the mixed layer and transition layer evolution following two storms with similar wind forcing. In one storm, the mixed layer deepens through thermocline erosion due to enhanced mixed layer turbulence. Another storm, by contrast, sees the shoaling of the mixed layer but a widening of the transition layer, due to the excitement of more near-inertial oscillations, which mixed deeper in the thermocline.

Few available observations resolve turbulent structures at the base of the mixed layer. The most directly comparable study to the present work is Kaminski et al. (2021), who used a neutrally-buoyant drifting profiler with a dense thermistor chain (T-chain) to sample the transition layer with 6 cm vertical spacing. Using a one-dimensional Thorpe scale analysis, they found that a multitude of small, highly-stratified overturns at ≤ 10 cm vertical scales can account for the

observed mixed layer deepening. While their observations also hinted at large-scale KH-type instabilities, as inferred from a broadening of the thermocline isopycnals and increased interface motions, their observations were limited by a vertical aperture of 1.4 m.

This study complements previous observations by using a 100 m T-chain, sampling the water column from near the surface to well below the transition layer, while maintaining high vertical resolution (25 cm) and time resolution (10 s). This is enabled by using the freely drifting thermistor chain as a profiling instrument, taking advantage of surface wave motion on the surface buoy to create synthetic vertical resolution. An additional innovation is that the thermistor chain is tethered to a Wirewalker which gives profiles of T and S over the whole range of thermistors, at comparable vertical resolution, every 15 minutes. In comparison to Kaminski et al. (2021), we have less vertical resolution, because the thermistors are spaced further apart, but have a much larger aperture for studying both the transition layer, as well as the mixed layer and stratified interior.

Using observations of temperature from a drifting thermistor chain, we observe the deepening of the mixed layer following a storm. We identify large-scale coherent turbulent structures in the transition layer based on the presence of unstable temperature overturns, the heave of stratified waters upwards into the mixed layer, and from negative strain anomalies associated with reduced stratification, all of which we interpret as signs of turbulence. The relationship between the mean shear and stratification in this transition layer further supports our observations as capturing the turbulent region at the base of the mixed layer. We relate the vertical and horizontal scales of these structures to the dominant forcing regime. During a storm, we observe wind-wave dominated turbulence in the presence of both stabilizing surface heat flux and convective cooling. As the storm passes, winds decrease sufficiently to allow for the formation of diurnal warm layers, which isolate the transition layer from wind forcing. Leveraging an array of drifting instruments, remotely-piloted wave gliders, and shipboard measurements, we constrain a one-dimensional energy budget. Estimates of entrainment velocity derived from Thorpe scales in the transition layer are consistent with the observed deepening. These observations of coherent

turbulent structures at the base of the mixed layer provide a valuable comparison for idealized numerical simulations of stratified turbulence, furthering our understanding of mixing in the ocean surface boundary layer.

2.2 Methods

2.2.1 Experiment

The data used in this paper were collected as part of the Task Force Ocean (TFO) "Platform Centric ASW Processing with Through-the-Sensor Data Assimilation and Fusion" experiment off the coast of Southern California in November 2020. The experiment was conducted in deep water off the continental shelf between 5 November and 14 November 2020. A second leg to this expedition was conducted between 15 November and 24 November in the Catalina Basin, with observations of Langmuir circulations published in Andriatis et al. (2024). The experiment was based aboard the *R/V Sally Ride*, from which we deployed an array of five drifting Wirewalkers (Pinkel et al. 2011), initially arranged in a cross measuring 7 km on each side. The middle Wirewalker was tethered to a drifting thermistor chain (T-chain). A remotely-piloted wave glider supported the experiment by performing box-shaped transects around the array of drifting instruments. Instruments were purposefully deployed at the edge of a cyclonic eddy so that they drifted coherently to the north-west. Inertial oscillations as a result of the wind forcing can be observed in the instrument drift trajectories (Figure 2.1).

Instruments were deployed on 05 November in anticipation of an incoming storm. Between 06 November and 07 November, winds increased from about 9 m s^{-1} to a peak of about 15 m s^{-1}, gradually falling to below 5 m s^{-1} by the 14 November (Figure 2.2). Significant wave height rose from 1 m to around 5 m, lagging the peak in wind speed by about a minute. At their peak, the wind and waves were consistently coming from the north-west. During the storm net surface buoyancy forcing was destabilizing during most of the day, except for about a 3-hour peak during the solar maximum, when the surface heat flux was weakly stabilizing. Towards the end of the

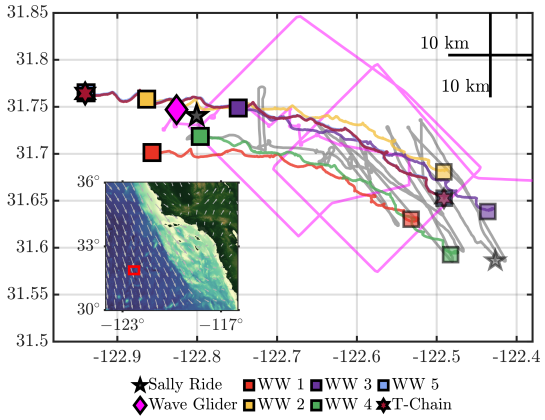

Figure 2.1. Map showing the experiment region and trajectories of deployed assets. The positions of assets on 06 November, shortly after their deployment, are indicated by translucent markers in the south-east. The Wirewalker and T-chain array drifts to the north-west during the deployment. The *Sally Ride* performs transects within the array as it drifts, while the wave glider is remotely piloted to perform box transects around the outside of the array. Note that the wave glider does not enter the plotted area until 09 November. The final positions of the assets on 13 November shortly before their recovery are indicated by solid markers in the north-west. The inset shows the larger California coast region, with the experiment area outlined in red. Grey arrows indicate the 10-meter wind velocity from ERA5 reanalysis at the time of the maximum observed wind speeds on 2000 UTC 06 Nov.

observations, net surface heat flux was more strongly stabilizing during the day, giving rise to diurnal warm layers. As a result of the storm, the mixed layer depth was observed to deepen from about 35 m depth to about 45 m depth.

2.2.2 Instrumentation

The main platform used in this study is a drifting thermistor chain (T-chain), consisting of 58 thermistors attached to a cable between the surface float and 100 m depth. Nominal thermistor spacing was every 3.5 m, with a denser section of 0.5 m spacing near the base of the mixed layer. The T-chain used 29 Seabird SBE56, 9 RBRsolo^3 T, 15 RBRsolo^3 T|deep, and 3 RBRsolo^3 T|fast16 thermistors, along with 2 RBRduet^3 T.D|fast16 which also recorded pressure. The two Duets, numbers 21 and 48 counting from the surface, were deployed at mean depths of 32.0 m and 66.0 m respectively. The depth of the other 56 thermistors was derived from the observed pressure at the depth of the duets and the planned spacing between thermistors. The

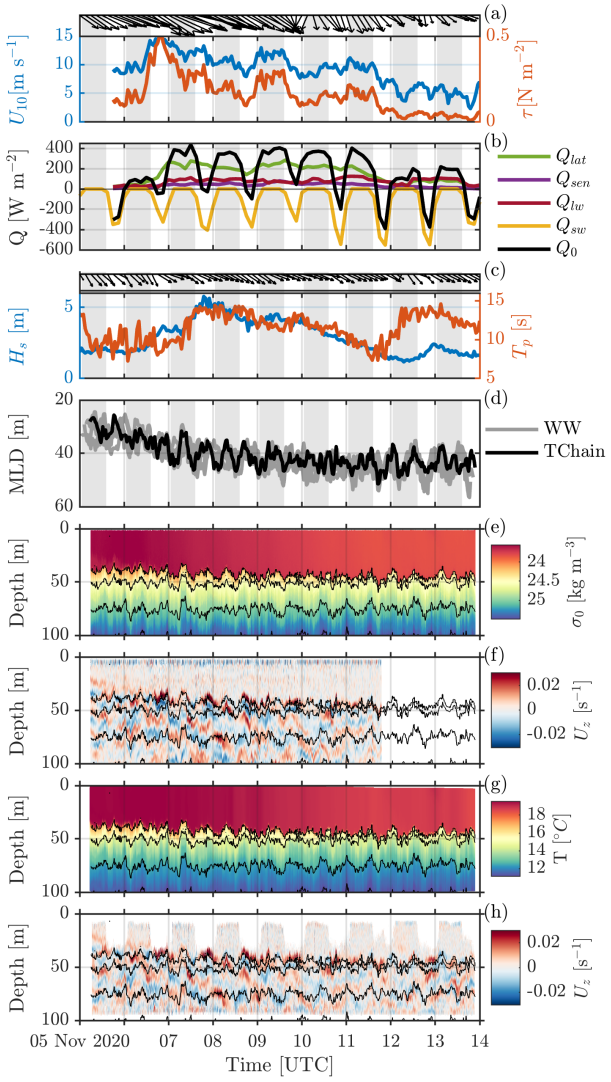

Figure 2.2. Data summary: (a) Wind speed at 10 meters U_{10} (blue) and derived surface wind stress τ (red) and direction (arrows). (b) Total surface heat flux Q_0 (black) and its constituent components, latent (green), sensible (purple), outgoing longwave (red) and incoming shortwave (yellow) radiation. Radiation components are measured from the *R/V Sally Ride*, with the remaining components derived from observations from the wave glider. (c) Significant wave height (blue), the period of the peak frequency (red), and the direction of the peak frequency (arrows). (d) Mixed layer depth from each of the Wirewalkers (gray) and the T-chain (black). (e) Wirewalker 5 CTD observations of potential density relative to the surface σ_0. (f) Wirewalker 5 ADCP observations of vertical shear of zonal velocity U_z. (g) T-chain observations of temperature, binned to a 15-minute grid for plotting. (h) T-chain observations of vertical shear of zonal velocity, binned to a 1-minute grid for plotting. Black contours in (e-h) represent 0.5 kg m^{-3} contours of the WW5 potential density in (e) for comparison.

top thermistor was deployed at a mean depth of 4.0 m, and the deepest thermistor was at a mean pressure of 97.6 m during the deployment. The dense thermistor region was between 21.5 m and 42.2 m. The sampling frequency of most thermistors was 2 Hz, with fast16 thermistors sampling at 16 Hz. Seabird SBE56 have a temperature response time constant <0.5 seconds and factory accuracy of ±2 mK. All RBR thermistors used have a temperature response time constant <0.1 seconds and factory accuracy of ±2 mK. The calibration procedure to improve thermistor accuracy is described below.

The T-chain drifts freely, supported by a buoyant surface float with a GPS transponder. In the presence of surface waves, the surface float drags the thermistor chain through the water column. We leverage this wave driven vertical displacement to use the T-chain as a profiling float, gaining vertical resolution at the expense of temporal resolution in the gridded product. The pressure records of the two duets are coherent and observe pressures matching the expected deployment depths, allowing us to assume that the T-chain is under sufficient tension to be near-vertical in the water column, and to treat the line as a solid body. During the storm, the peak wave period was about 10 s, with up to 5 m significant wave height. Even with 3.5 m thermistor spacing,the T-chain samples across its entire aperture approximately every 10 seconds, as long as the wave amplitude is at least 1.75 m. To construct a gridded product, data are binned into a 0.25 m vertical grid over a 10 second time window. If those 10-second records occur during a large wave event, the water column is well-sampled, with some depth bins having measurements from multiple thermistors. All the available data in a given depth bin are averaged via a simple mean. At times of low wave amplitude and especially for sections of the array with coarse thermistor spacing, some depth bins have no observations, in which case the binned product is filled by vertical interpolation. Note, our choice of 0.25 m vertical grid resolution was constrained by the thermistor response time constant. For a 10 second wave period and 5 m amplitude, thermistor vertical velocities exceed 2 m s^{-1}. The SBE 56 thermistors, with a time constant of $\tau = 0.5$ s, cover approximately one meter per time constant. RBR thermistors, with a faster time constant of $\tau = 0.1$ s, cover approximately 0.2 m per time constant.

Several calibration steps are applied to the thermistors before the gridding process. First, a constant time offset between the two Duets is removed by cross-correlation between the duet pressure records. The pressure records are coherent up to 1 Hz, with a difference in the gain at surface wave frequencies, owing to the decay of wave orbital velocity with depth. That is, the shallower Duet at 32 m depth observed about a 10% lower pressure amplitude at peak wave frequency because of the greater wave orbital amplitude at shallower depth. While a fit could have been done to fully remove the wave orbital motion based on the two observed depths and a constant free surface, we instead opted to use the pressure record of the deeper Duet as the "orbital-free" pressure record, equating the perturbation in pressure to the inverse of the height of the free surface η. A pressure record for each Duet is constructed by adding η to its position on the T-chain relative to the known depth of Duets 21 and 48. A constant time offset and linear drift is applied to the time record of each thermistor using the cross-correlation between the observed temperature and the timeseries of η. This method relies on the assumption that the dominant temperature perturbation for each thermistor is its being dragged vertically through stratified water by the wave motion. For regions of stable stratification, η is correlated with temperature, as a positive η (shallower depth) will be associated with warmer temperature. However, during a significant portion of the record, the in-situ temperature in the mixed layer is colder near the surface, leading to anti-correlation between η and the observed temperature. Thus, to calculate the time offset, we identify the time lag for which the magnitude of the cross-correlation has a maximum, to account for both regimes. For each thermistor, a linear trend is fit to the time lags, calculated over one-hour segments, resulting in a mean clock offset and drift correction. This proved to be an important step as some thermistors turned out to have clock offsets on the order of 10 s, significantly affecting the combined gridded product, despite our best care in synchronizing clocks when setting up the thermistors prior to deployment. Thermistor calibration for a constant temperature offset was performed by attaching the T-chain, rolled up, to the ship's CTD Rosette, which was lowered to 100 m depth for 15 minutes. A constant temperature difference is subtracted from each thermistor to match the observed Rosette temperature. Thermistor accuracy drift over

the duration of the deployment is negligible based on manufacturer specifications. Finally, a small (order mK) post-gridding temperature offset was applied to the thermistors. The mixed layer has temperature gradients on the same order as the error remaining after in-situ calibration. This results in apparent lines in the observed temperature in the weakly stratified mixed layer. To remove this error, we examine 10-s time periods where, for a given thermistor, the top of its profile overlaps with the bottom of the thermistor above it, and similarly for the thermistor below it. If a given thermistor is, on average over the deployment, biased warm relative to both the thermistor above and below it, a constant temperature offset is removed, equal to the mean of these anomalies.

An upward-looking Teledyne Workhorse 300 kHz ADCP was mounted at 100 m depth at the base of the T-chain. ADCP data have 2 m vertical resolution and recorded at 0.5 Hz. During the day, biological scatterers move to the base of the mixed layer, resulting in low correlation values in the mixed layer. The low correlation data threshold was programmed at 64 prior to deployment, limiting our ability to recover daytime mixed layer velocities. At night, scatterers move back up throughout the mixed layer, giving us full 100 m depth velocity data (Figure 2.2 h). For much of the analysis, we equate observation time with a lateral distance by assuming that the observed temperature is swept past the T-chain at a fixed velocity for a given time window. Because ocean velocity is sheared over the aperture of the T-chain, and because the T-chain is tethered to a Wirewalker with a different drag profile, the T-chain does not move with the flow. The ADCP observes the ocean velocity relative to the T-chain. When analyzing processes in the transition layer, we use the average of the T-chain-relative velocity from ± 5 m relative to the thermocline depth, averaged over a time window of interest, to find the transition layer velocity relative to the T-chain and from there compute the observed lateral distance.

Five drifting Wirewalkers (Pinkel et al. 2011), vertically profiling wave-powered instruments, were deployed featuring a CTD and upward-looking ADCP (Zheng et al. 2022). Four of the instruments profiled to 500 m while the fifth, Wirewalker 5 (WW5) profiled to 200 m. The profile repeat times vary with wave conditions, with typical repeat times every 7 minutes for

WW5. The Wirewalker data complement the T-chain data by providing temperature and salinity data at high vertical resolution, with less frequent profiles. WW5 was tethered to the drifting T-chain by a 200 m long chain stretching between the base of the T-chain and the base of the Wirewalker. The T-chain and Wirewalker have different drag profiles. On average, the T-chain was south-west of the Wirewalker, but their relative positions occasionally reverse depending on the magnitude and phase of inertial oscillations. While 200 m separation between the instruments is too great to measure the same coherent turbulent structures, the instruments do observe the same general stratification and shear patterns.

We use the T-S relation observed by WW5 to build confidence in the temperature - dominated stratification of the transition layer, and to exclude periods of salinity-dominated stratification from the analysis. The T-S curve is very linear except for the beginning of the deployment at the ML base. Furthermore, the close similarity in the shear field observed from the T-chain and WW5 ADCPs increases confidence in the T-chain observations despite using a long-range ADCP with lower vertical resolution.

Atmospheric and surface forcing observations were collected from the *Sally Ride* and a remotely-piloted Liquid Robotics SV3 wave glider. The wave glider was equipped with a meteorological package and flow-through CTD, an upward-looking Signature 1000 ADCP on the subsurface platform and downward-looking ADCP mounted on the surface float (Grare et al. 2021; Hodges et al. 2023). The wave gliders also measure the directional wave field using high-precision GPS and inertial measurement units (IMUs) (Colosi et al. 2023). The *Sally Ride* provided observations of atmospheric conditions - air temperature, humidity, pressure, and precipitation, along with downwelling solar shortwave and longwave radiation. A flow-through CTD system recorded ocean temperature and salinity at 5 m depth. The wave glider arrived in the experiment region shown in Figure 2.1 on Nov 09, but was within 200 km of the T-chain for the duration of the observations. Given the large synoptic scale of the atmospheric forcing and the similarity between the *Sally Ride* and wave glider meteorological observations, we take the wave glider observations as sufficiently representative of the forcing present at the T-chain, and

prefer to use wind speed from the wave glider, as the *Sally Ride* wind observations are sometimes contaminated by wind shadow effects due to its hull.

2.3 Qualitative observations of transition layer coherent structures across forcing regimes

A primary objective of this study is to investigate the relationship between OSBL forcing, i.e. wind, waves, and heat flux, with mixing processes at the base of the mixed layer. The T-chain is well suited for analyzing the coherent turbulent structures apparent in the temperature record because of its large aperture, and high temporal and spatial resolution.

To categorize the surface forcing regimes, we compare the relative importance of turbulent processes using non-dimensional parameters relating the scaling of turbulent velocities. The turbulent velocity scalings for wind-shear driven turbulence, convective turbulence, and Stokes drift-shear driven Langmuir turbulence are

$$\text{Wind:} \quad u_*, \tag{2.1}$$

$$\text{Buoyancy:} \quad w_* = (B_0 h)^{1/3}, \tag{2.2}$$

$$\text{Waves:} \quad w_{*L} = (u_*^2 u_{s0})^{1/3}, \tag{2.3}$$

where u_* is the wind friction velocity, B_0 is the surface buoyancy flux, h is the mixed layer depth, and u_{s0} is the surface Stokes drift. u_* an B_0 are obtained from wave glider observations using the COARE algorithm for calculating air–sea fluxes (Fairall et al. 2003), while u_{s0} is determined from observed wave spectra, with a correction for unresolved wind-waves (Pizzo et al. 2019). Details of these calculations are provided in Andriatis et al. (2024). Mixed layer depth is defined as the depth at which the temperature is 0.2 C colder than the mean temperature of shallower water (Boyer Montégut et al. 2004).

The relative contribution to TKE production from these three turbulence processes is given by the non-dimensional parameters Langmuir number, La_t, comparing the ratio of

wind-forced to wave forced TKE production, the Langmuir stability length h/L_L, giving the ratio of buoyancy-forced production to wave-forced production, and the stability parameter Λ, comparing wind-forced to convective turbulence:

$$\mathrm{La}_t^2 = \frac{u_*^3/h}{w_{*L}^3/h} = \frac{u_*}{u_{s0}}, \tag{2.4}$$

$$\frac{h}{L_L} = \frac{w_*^3/h}{w_{*L}^3/h} = \frac{B_0}{u_*^2 u_{s0}/h}, \tag{2.5}$$

$$\Lambda = -\frac{h}{L_O} = \kappa \frac{w_*^3}{u_*^3} = \kappa \frac{B_0 h}{u_*^3}, \tag{2.6}$$

where L_O is the Monin-Obukhov length. Note that these three parameters are not independent. The largest La_t is experienced at the peak of the wind forcing, with the relative importance of convection and Langmuir turbulence enhanced at lower wind speeds (Figure 2.3). The relative dominance of wind, wave, and buoyancy forcing can be visualized in a phase diagram, following Li et al. (2005), Belcher et al. (2012), and Li et al. (2019) (Figure 2.4).

To contrast the effects of different surface forcing, we identify four characteristic regimes:

(A) strong wind-wave forcing with surface convective cooling, which characterizes the majority of the forcing during the storm,

(B) strong wind-wave forcing with stabilizing surface heating, which occurs around the solar maximum each day during the storm,

(C) weak wind-wave forcing with destabilizing surface cooling, characteristic of the nighttime regime after the storm, and

(D) weak wind-wave forcing with stabilizing surface heating, which leads to the formation of a diurnal warm layer.

Using 3-hour samples of thermistor chain data, we identify temperature features within the OSBL that characterize each of these forcing regimes (Figure 2.5). In (B), winds are at their

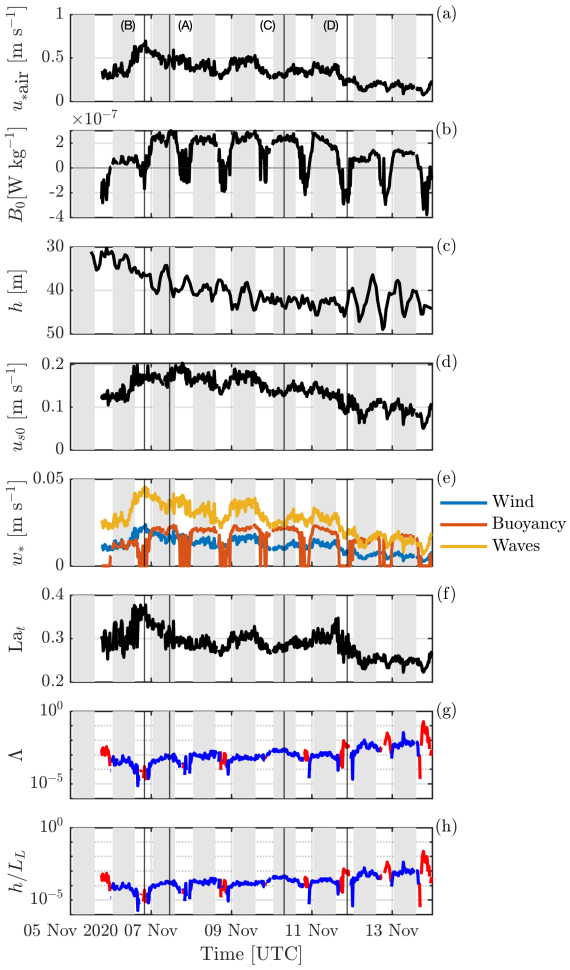

Figure 2.3. Components of the calculation of non-dimensional TKE production scaling. (a) Friction velocity in air. (b) Surface buoyancy flux. (c) Mixed layer depth. (d) Surface Stokes drift. (e) Turbulent velocity scaling for wind (blue), buoyancy (red), and wave (yellow) forcing. Sections of stabilizing buoyancy are plotted as zero convective turbulent velocity. (f) Turbulent Langmuir number. (g) Stability parameter. (h) Langmuir stability length. Stabilizing forcing in (g,h) is shown in red, destabilizing in blue. The times of four selected timeseries representative of different forcing regimes, plotted in Figure 2.5, are indicated by vertical lines.

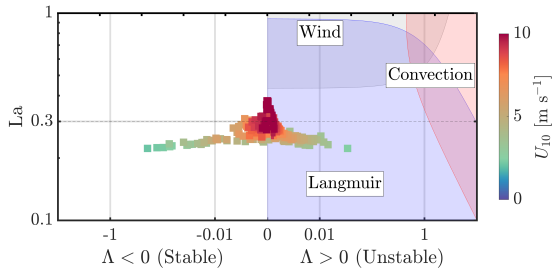

Figure 2.4. Scale analysis of the forcing, shown as a scatter plot of 10-minute binned observations, colored by the 10-meter wind speed, using the non-dimensional parameter space La_t vs. Λ. The x-axis is divided into regions of stable buoyancy forcing on the left ($\Lambda < 0$) and unstable convective forcing on the right ($\Lambda > 0$). For unstable buoyancy forcing, colored regions show where a forcing mechanism contributes at least 25% of TKE production, for wind (gray), wave (blue) and convective (red) forcing for the parameter space La_t vs. Λ. The dashed line traces the wind-wave equilibrium at $La_t = 0.3$. The plot is logarithmic except in the region $|\Lambda| < 0.01$, where the x-axis is linear.

peak, and surface buoyancy forcing is weakly stabilizing, so we expect a mixed layer mixing regime dominated by wind stress and Langmuir turbulence. Indeed, we observe patterns of alternating, vertically coherent temperature anomalies, with warm anomalies consistent with the downwelling phase of Langmuir circulations (Andriatis et al. 2024). At the base of the mixed layer, we find stratified scouring structures. In (A), winds are still strong, and nighttime cooling creates a weak temperature inversion near the surface. Coherent temperature patterns are absent from the upper mixed layer, likely due to the effect of surface cooling obscuring temperature anomalies from Langmuir circulations. In (C) the wind has decreased from its peak but nighttime convective cooling is strong, characterizing this regime as convection-dominated. The upper 10 m feature a consistent temperature inversion, with plumes qualitatively resembling Rayleigh-Bénard convection instabilities. In (D), winds are weak, with stabilizing surface buoyancy forcing, giving a wave-dominated regime in a diurnal warm layer. Coherent warm temperature anomalies scouring the base of the diurnal warm layer are attributed to the effect Langmuir circulations, which locally increase downward momentum flux, enhancing shear instability (Kukulka et al. 2010).

We now shift our attention to characterizing turbulent structures in the stratified transition

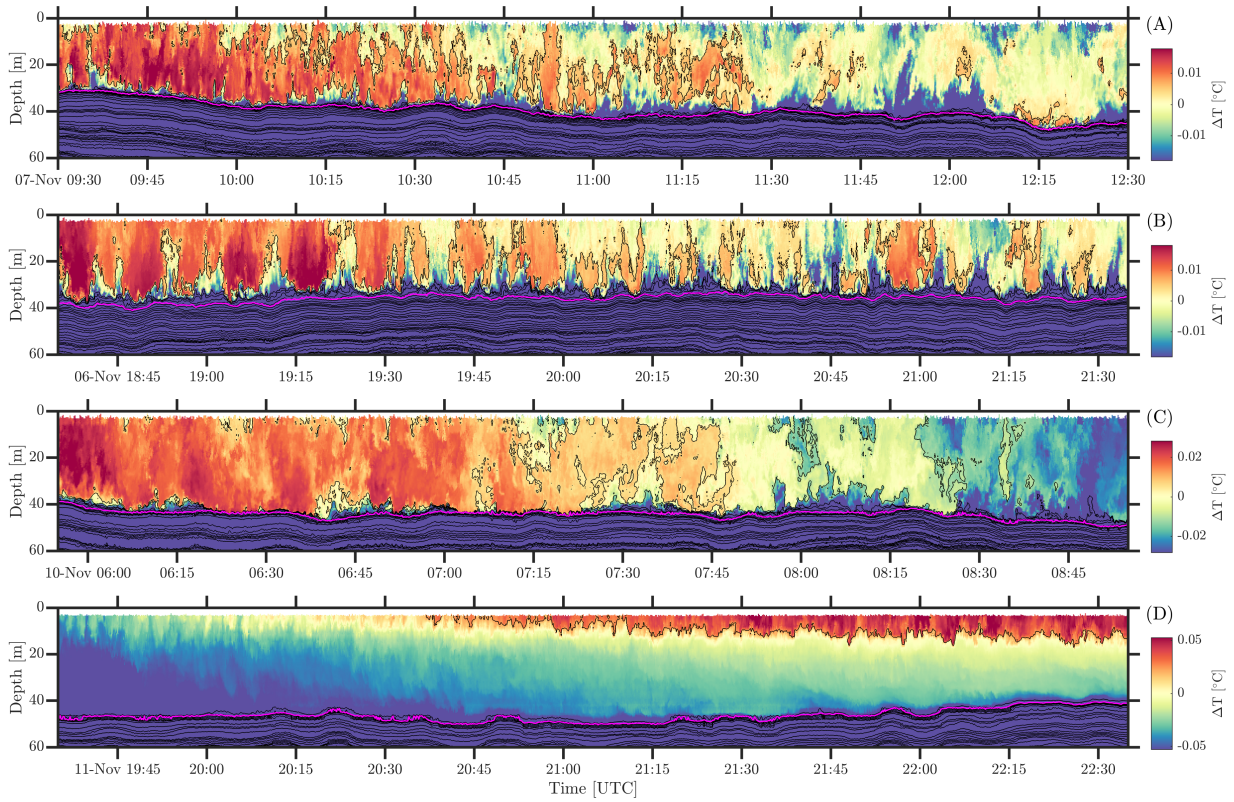

Figure 2.5. 3-hour temperature timeseries showing the behavior of the upper mixed layer for four selected times based on turbulent velocity scaling in Figure 2.4. (A) Wind-wave dominated forcing with destabilizing buoyancy flux. (B) Wind-wave dominated forcing, with weakly stabilizing surface buoyancy flux. (C) Convectively-dominated period with weaker wind forcing. (D) Strongly stabilizing surface buoyancy forcing, with weak winds. Magenta line indicates the mixed layer depth. Black lines are isothermal contours, spaced equally in depth every 1 m, with the requirement that neighboring contours are separated by at least 0.01 °C. The color range varies between plots and is chosen based on the central 99% of the temperature range between 5 to 20 m depth, to highlight features within the mixed layer, while he rest of the temperature range is saturated. These profiles should be considered keeping in mind the evolution in both space and time.

layer. The vertical extent of the transition layer can be defined in many ways (Johnston and Rudnick 2009; Kaminski et al. 2021). Generally, the region of interest starts from a depth where the stratification begins increasing below the well-mixed OSBL, all the way to the depth of the main pycnocline, representing the start of the ocean interior. The depths of maximum stratification and maximum shear are contained within the transition layer. We define the top of the transition layer as the deepest depth for which the vertical gradient of the sorted temperature profile is < 0.01 K m^{-1}. We find that this definition consistently selects for the upper limit of stratified water. To simplify nomenclature, we will here refer to the top of the transition layer as the boundary layer depth h_b. The base of the transition layer is more challenging to distinguish from the ocean interior. The ocean interior, supporting a rich internal wave field, is layered, with steps in temperature. We define the base of the transition layer here as the depth of the first local minimum in the stratification profile, below the depth of maximum stratification. This definition allows us to select a transition layer containing the the stratification peak while avoiding the internal wave field in our analysis. We refer to the bottom of the transition layer as the cutoff depth h_c in the following.

The transition layer covers a wide range of stratification, complicating its visualization in temperature space. For any given choice of temperature range, information is obscured in more or less stratified regions of the TL. We use several alternative diagnostic tools to identify patterns of coherent turbulent structures. First, because the TL is heaved up and down by internal wave motions, we analyze the data in a reference frame that follows the depth of the maximum stratification, which we refer to as the thermocline-relative depth coordinate. At every time step, we find the depth of the maximum stratification and apply a 10 minute low-pass filter to construct the reference depth. In this reference frame it is easier to distinguish heaving of isotherms associated with turbulent patches from internal wave displacement.

We quantify the scale of turbulent temperature structures using three methods. First, we use a classical Thorpe scale analysis on patches of unstable stratification. At every time step, the temperature profile is adiabatically sorted, in the range between the boundary layer depth and the

bottom of the profile, into statically stable profiles. The Thorpe scale L_T is given by the RMS of the vertical displacement d of a parcel away from its statically stable depth,

$$L_T = \left\langle d^2 \right\rangle^{1/2}. \tag{2.7}$$

Each individual overturning event is ascribed a single Thorpe scale. Overturning events are identified using the vertical cumulative average of displacement lengths, with a single patch being a series of consecutive points with non-zero cumulative overturning lengths. There can be several overturning events within a single profile. This definition allows us to exclude non-overturning regions from the Thorpe length calculation while including points with zero displacement length within an overturn, such as at the center of a KH instability.

Next, we look at the heave associated with the displacement of the boundary layer depth upwards into the well-mixed OSBL. In stratified turbulence, mixing events have a characteristic wispy scouring signature where waters affected by a turbulent overturn are pushed upwards into weak stratification (Sarkar and Pham 2019; VanDine et al. 2021). A simple metric to track the behavior of the transition layer boundary heave is the change in its variance, computed over a given time window, over the course of the observations. We expand on this metric by identifying individual displacement events, and fitting to their height and width using a Gaussian profile. We identify an event as the series of continuous points for which the boundary layer depth is shallower than its own mean over a given time window. These points are fit by a Gaussian profile, using the 90^{th} percentile of the boundary layer depth as the base of the fits. The amplitude of the Gaussian gives a vertical scale and the FWHM gives lateral scale. An example of the Gaussian fitting procedure given in Figure B.1.

Finally, we use patterns of stratification anomaly to identify regions of turbulence. Consider the roll-up of a KH instability and subsequent transition to developed turbulence - while we may only be able to resolve overturns during the initial rollup of a KH instability, the turbulent patch as a whole heaves isopycnals upwards at its top half, while depressing isopycnals

downwards around its bottom half, leaving a center of reduced stratification (Sarkar and Pham 2019). By identifying patches of stratification which follow this pattern, and computing their vertical and horizontal scales, we can estimate the outer scale of a turbulent patch as a complement to the overturning scale as given by Thorpe scales. Specifically, we select for turbulent patches in the transition layer as having negative strain ξ, given by

$$\xi = \frac{N^2 - < N^2 >_\theta}{< N^2 >_\theta}, \tag{2.8}$$

where the reference stratification $< N^2 >_\theta$ is given by the mean stratification at the same temperature as the observation. We identify patches of $\xi < -0.1$ using a binary contouring algorithm. The vertical and lateral scales for a given negative strain patch are given by its bounding box.

2.3.1 Wind-wave forcing with surface cooling

Examples of TL temperature structures during wind-wave dominated forcing with surface cooling are shown in Figure 2.6. In each selected time segment there are several distinct events of upwards boundary layer heave, each of which is associated with overturning patches, as indicated by profiles of Thorpe scale. These patches of instability are mostly confined to between the boundary layer and mixed layer depths, centered on the peak of the boundary layer intrusions. Patches of reduced stratification extend vertically from the boundary layer depth to below the thermocline beneath these intrusion events. Temperature contours below the TL show an energetic internal wave field, with strong isopycnal heaving and layering.

2.3.2 Wind-wave forcing with weak surface heating

Examples of TL structures during wind-wave dominated forcing with weakly stabilizing surface heating are shown in Figure 2.7. As with case (A), the boundary layer depth is periodically heaved upwards. In this regime, however, there are more coherent temperature anomalies in

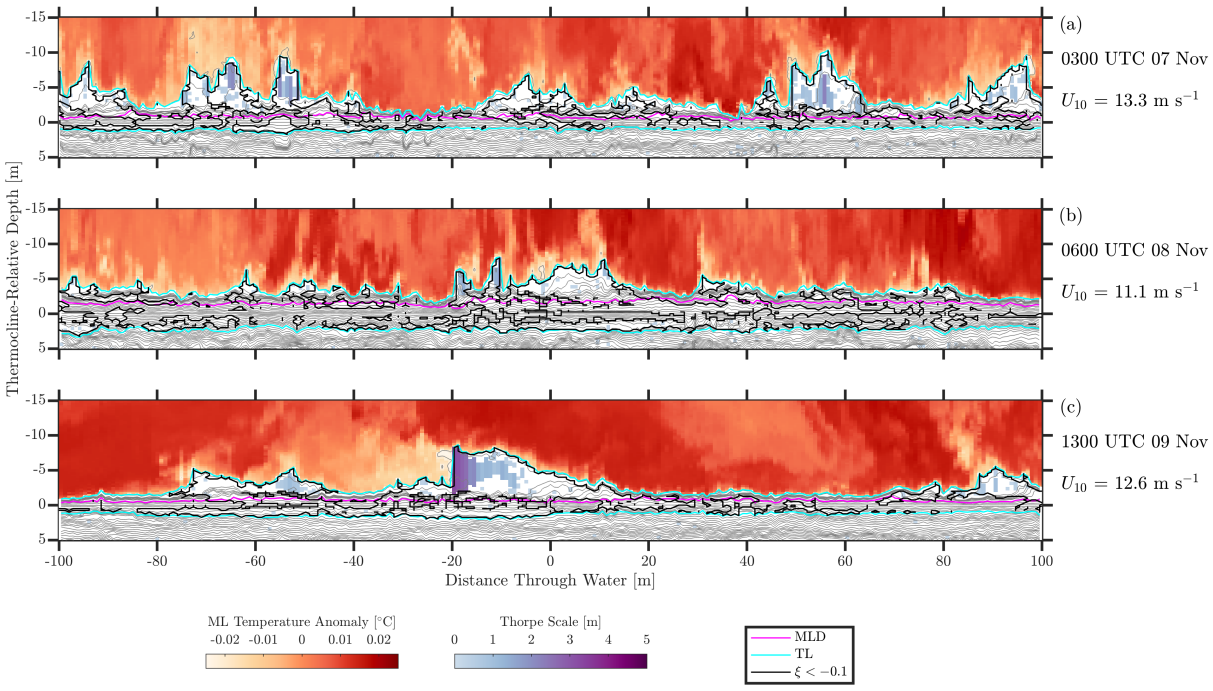

Figure 2.6. Observations of the transition layer during wind-wave dominated forcing with surface cooling. Mixed layer temperature is plotted in color for temperatures above the boundary layer isotherm, with the color range saturated to show a range of $\Delta T = 0.05$ °C relative to the mean temperature in the well-mixed layer. Below the boundary layer isotherm, temperature is contoured in thin gray contours, spaced equally in depth every 0.25 m, with the requirement that neighboring contours are separated by at least 0.01 °C. Overturns below the boundary layer are plotted in color representing their associated Thorpe scale L_T. The boundaries of the transition layer (cyan) trace the isotherms whose mean depths in the sorted temperature profile equal h_b and h_c respectively. Thick black contours outline patches of reduced stratification, $\xi < -0.1$. The magenta line is the mixed layer depth. The amount of time represented by each plot is about 1 hour, with some variation according to the relative velocity between the transition layer and the T-chain, thus these profiles should be considered as transects that include time evolution.

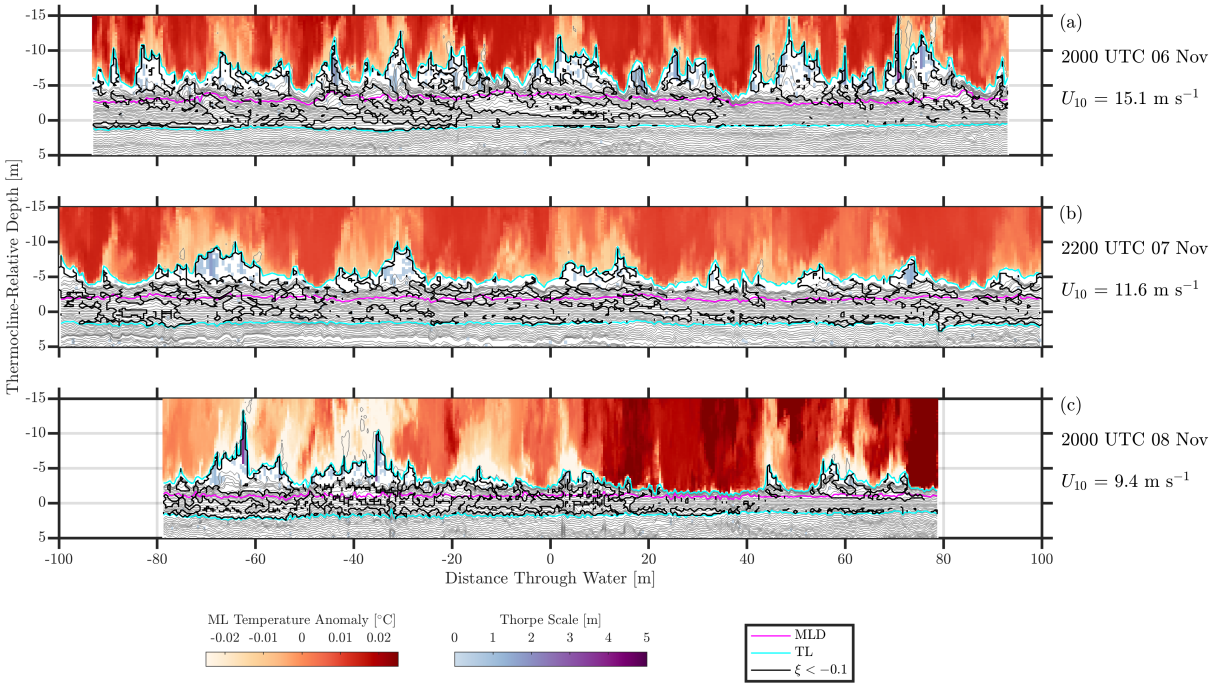

Figure 2.7. Observations of the transition layer during wind-wave dominated forcing with weak surface heating. Plot elements are the same as in Figure 2.6.

the mixed layer above, and the upwards heave appears to be correlated with minimums in the mixed layer temperature, separated by warm ML anomalies displacing the boundary layer depth downwards. We attribute these warm temperature patterns to Langmuir circulations. In the absence of convective turbulence, warmer waters near the surface, heated by shortwave radiation, are swept downwards by the downwelling component of Langmuir circulations. While we also expect Langmuir circulations to be present in Figure 2.6, surface convection might be mixing away their associated warm temperature anomaly.

2.3.3 Convective cooling with weak wind forcing

Examples of TL structures during convectively-dominated forcing with weak wind forcing are shown in Figure 2.8. In these segments, the boundary layer depth is much less energetic. Where there is an upward anomaly in the boundary layer depth, it tends to be broader, and associated with fewer overturns and smaller Thorpe scales where an overturn exists. There

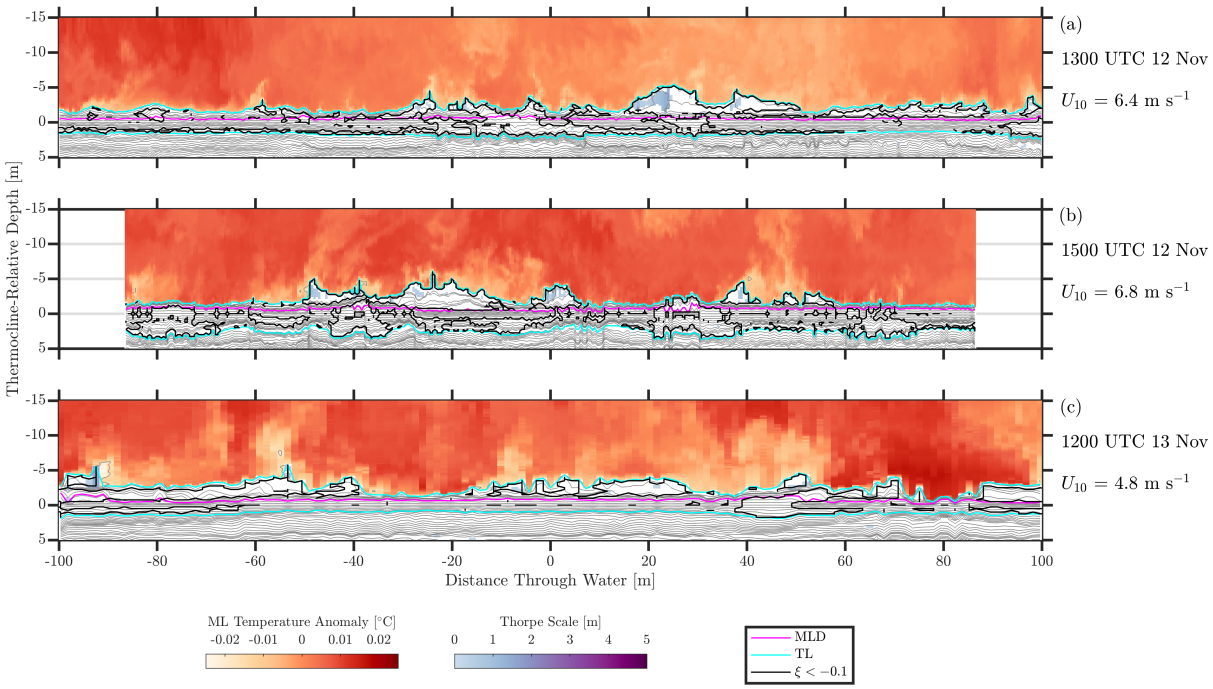

Figure 2.8. Observations of the transition layer during convectively-dominated forcing with weak wind forcing. Plot elements are the same as in Figure 2.6.

appears to be much more separation between boundary layer depth anomalies.

2.3.4 Diurnal warm layer with weak wind forcing

We also examine turbulence at the base of the mixed layer in the presence of a diurnal warm layer (Hughes et al. 2020; Zeiden et al. 2024), which isolates the mixed layer base from atmospheric forcing (Wijesekera et al. 2020). In the absence of wind-driven shear, we view turbulent structures at the mixed layer base as being induced by either the mean shear or internal wave breaking. Examples of the transition layer during stabilizing buoyancy forcing with weak winds, in the presence of an overlying diurnal warm layer, are shown in Figure 2.9. Again, the boundary layer depth is not energetic, and the several observed overturning patches have much broader horizontal scales than during the wind-forced regions.

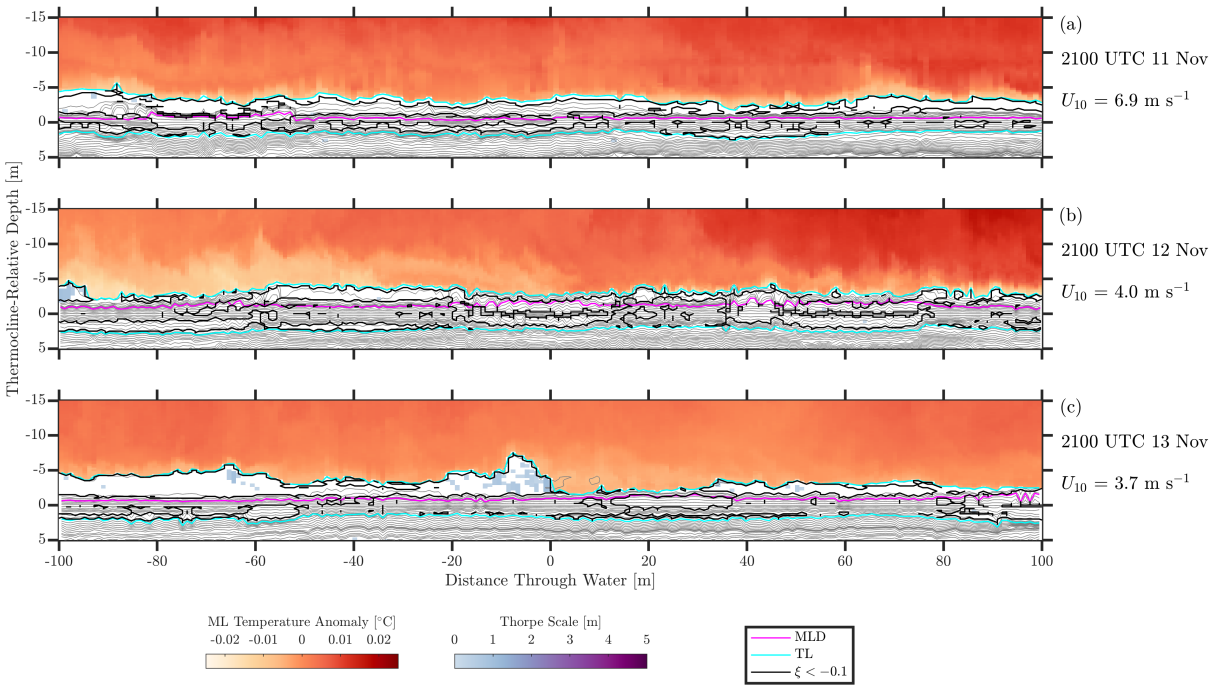

Figure 2.9. Observations of the transition layer below a diurnal warm layer during stabilizing buoyancy forcing with weak wind forcing. Plot elements are the same as in Figure 2.6.

2.4 Scaling of the transition layer turbulence

We contextualize the observed features and spatial scales of the transition layer turbulent structures by comparing characteristics of the transition layer to previous literature of experiments and numerical simulations of stratified turbulence. A common numerical setup is to use a hyperbolic tangent shear layer with a velocity change, ΔU, over a thickness δ, in combination with a number of possible stratification profiles (Pham and Sarkar 2014; Sarkar and Pham 2019). These parameters form a characteristic Reynolds number for the system

$$Re = \frac{\Delta U \delta}{\nu}, \tag{2.9}$$

with molecular viscosity $\nu \approx 1 \times 10^{-6}$ m^2 s^{-1}. Previous literature has demonstrated a large dependence of turbulent characteristics on Re, including the flux coefficient Γ (VanDine et al. 2021).

In our observations, the transition layer is characterized by a shear maximum located just beneath the boundary layer depth and mostly above the mixed layer depth, and a stratification profile that grows sharply from near-zero in the mixed layer to a maximum that consistently occurs deeper in the transition layer than the shear maximum (Figure 2.10).

In order to directly compare the non-dimensionalized scales between our observations and simulations, we estimate approximate values for ΔU and δ in our measurements. Using the mean profiles of shear for each hour of observations, we define the velocity scale as the integrated shear over the transition layer,

$$\Delta U = \int_0^{h_b} < ||u_z|| > \mathrm{d}z, \tag{2.10}$$

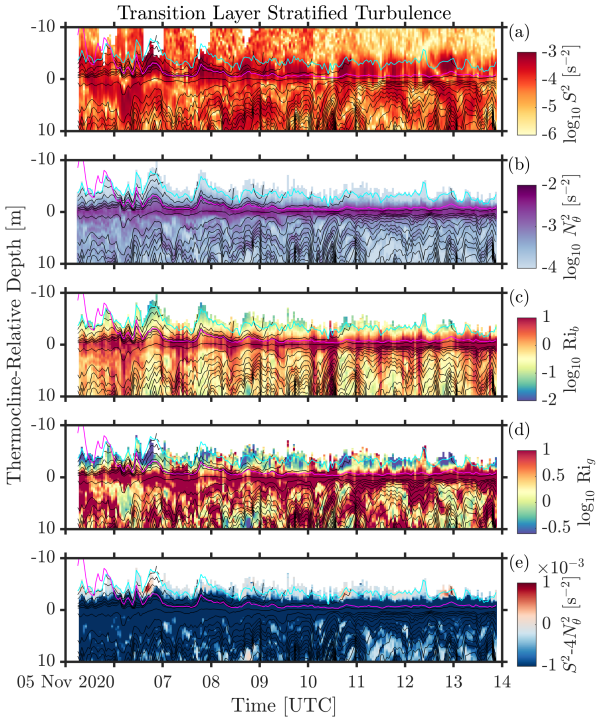

Figure 2.10. Shear and stratification scaling for the transition layer, using one-hour averages of T-chain data. (a) Squared shear magnitude $S^2 = ||u_z||^2 + ||v_z||^2$. (b) Stratification from temperature, $N_\theta^2 = g\alpha\theta_z$. (c) Bulk Richardson number Ri_b. (d) Gradient Richardson number Ri_g. (e) Reduced shear, $S^2 - 4N_\theta^2$, saturated to emphasize regions near or below the critical value $Ri_g = 0.25$. In all plots black contours are of temperature, spaced on average every 1 m, the cyan contour is the boundary layer depth h_b, and the magenta line is mixed layer depth.

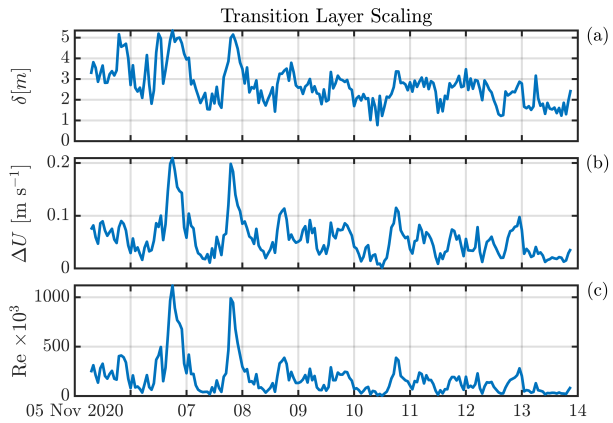

Figure 2.11. Scaling parameters for stratified turbulence in the transition layer. (a) Shear layer height (vorticity thickness), (b) velocity difference across the shear layer, and (c) Reynolds number, constructed from one-hour average profiles of the transition layer.

and the length scale as the velocity scale divided by the maximum shear in the transition layer,

$$\delta = \frac{\Delta U}{\max(< ||u_z|| >)|_0^{h_b}}. \tag{2.11}$$

This method yields typical vertical length scales of 2 to 4 m, velocity gradients of 5 cm s^{-1}, and Re$\approx \mathcal{O}(10^5)$ (Figure 2.11). This vertical scaling is comparable to the size of coherent temperature structures seen at the top of the transition layer.

Further, the behavior of the turbulent flow can be characterized according to the initial bulk and gradient Richardson numbers of the flow,

$$\mathrm{Ri}_b = \frac{N^2\delta^2}{\Delta U^2}, \tag{2.12}$$

$$\mathrm{Ri}_g = \frac{N^2}{S^2}. \tag{2.13}$$

In the case of a shear layer in a constant background stratification, these parameters are initially equal at the center of the shear layer. For increasing asymmetry in stratification between the top and bottom of the shear layer, Pham and Sarkar (2014) find a transition from symmetric KH billows to Holmboe wisps and cusps which scour the upper portion of the shear layer. Typical

transitional values of $\mathrm{Ri}_b \approx 0.25$ are found near the top of the transition layer, with a large asymmetry in Ri_b between the top and bottom of the transition layer (Figure 2.10). Near-critical average values of ($\mathrm{Ri}_g \approx 0.25$) are also observed near the top of the transition layer, while the bottom of the transition layer is strongly stably stratified. The large asymmetry in Ri_b across the transition layer suggests that these observations should be evaluated against numerical simulations such as Pham and Sarkar (2014), rather than more typical simulations with uniform or weakly asymmetrical stratification, keeping in mind that this system is also in a high Re regime.

The scaling of our transition layer observations relative to previous studies of stratified turbulence demonstrates that the observed temperature structures at the top of the transition layer are the signature of the dominant turbulence region between the mixed layer and the interior. It is the contribution of this transition layer turbulence that we expect is the leading mechanism for mixed layer deepening through thermocline entrainment and the exchange of heat between the mixed layer and ocean interior.

2.5 Mixed Layer Deepening, Entrainment Rate, and Heat Budget

Having characterized the large scales of coherent turbulent structures in the transition layer, we want to understand their relationship with the mixed layer energy budget and the observed rate of mixed layer deepening, to ultimately connect surface forcing with mixing. The change in mixed layer depth due to turbulence at the base of the mixed layer is given by

$$\frac{\mathrm{d}h}{\mathrm{d}t} \approx w_e, \tag{2.14}$$

where w_e is the entrainment velocity, the vertical velocity of the mixed layer based due to entrainment of denser water in the transition layer (Price 1979). The entrainment velocity is defined as

$$w_e = \frac{\mathcal{B}}{g'}, \tag{2.15}$$

where $\mathcal{B}$ is the diapycnal flux of buoyancy due to mixing (Winters and D'Asaro 1996) and $g' = g\Delta\rho/\rho_0$ is the reduced gravity. Fitting a linear slope to the observed change in mixed layer depth during the peak of its deepening period between 6 Nov and 11 Nov gives an average entrainment velocity of 2 m day^{-1} when averaging the T-chain and Wirewalker observations.

In non-Lagrangian observations, the mixed layer depth can appear to change due to lateral advection of a depth gradient. We rule out the effect of advecting spatial gradients in MLD as a significant contribution in the changing mixed layer depth by using spatial gradients across the instrument array. By fitting a plane to the observed mixed layer depths at the five Wirewalkers and the T-chain locations, and multiplying by the observed ocean velocity past the T-chain, we derive a mean advective term of $\mathbf{u_h} \cdot \nabla h = 0.1$ m day^{-1},corresponding to a small contribution relative to the observed deepening.

Over short time scales, the mixed layer depth is also affected by adiabatic processes including the heave of isopycnals due to internal waves and eddies, leading to $O(10$ m) variations in our data (Johnston and Rudnick 2009; Lucas et al. 2019; Kaminski et al. 2021). This isopycnal heave velocity can be represented by the displacement of a reference isopycnal below the transition layer that is likely to be affected by the same dynamics. We choose the 13 °C isotherm, with a mean depth of 62 m, as our reference. We use the MLD change averaged over all instruments, after removing the reference isopycnal heave, for comparison with estimated deepening rates (Figure 2.13 (b)).

Direct observation of the turbulent buoyancy flux is difficult because it requires measurements of turbulent velocity and buoyancy anomalies at small turbulence scales. Recent progress has been made in developing instrumentation for such observations, but they remain challenging and rare (Polzin et al. 2021). With sufficient temperature resolution, Winters and D'Asaro (1996) outline a method to calculate diascalar flux from scalar gradients.

In the absence of direct observations, buoyancy flux can be calculated from the TKE

dissipation rate ϵ by assuming a mixing efficiency

$$\mathcal{B} = \Gamma\varepsilon, \tag{2.16}$$

with the turbulent flux coefficient traditionally estimated as $\Gamma \approx 0.2$ (Osborn 1980; Gregg et al. 2018). Direct observations of ε have previously been obtained in the literature using shear probes via the Kolmogorov spectrum and high-resolution ADCPs (Lueck et al. 2024; Zippel et al. 2021). Unfortunately, our data collection plan did not include any observations of ε.

We therefore rely on one-dimensional parametrizations to estimate ε based on a turbulent length scale L,

$$\varepsilon \approx 0.64 L^2 N^3, \tag{2.17}$$

with $L \approx L_T \approx L_E \approx L_O/0.8$, where L_O is the Ozmidov scale (Osborn 1980), L_T is the Thorpe scale, and L_E is the Ellison scale. In the following sections we describe the estimate of buoyancy flux from temperature gradients and Thorpe scales before comparing their implied deepening rates with observations. While Ellison scale estimates were also computed, the fast buoyancy period at the thermocline (about 1 minute) compared to the time resolution of our gridded product (10 s), limited our confidence in these estimates.

2.5.1 Diascalar flux from temperature gradients

Following Winters and D'Asaro (1996), we estimate the mixing attributable to individual overturning events by computing the diapycnal flux. Winters and D'Asaro (1996, eq.7) relate diapycnal flux to the squared density gradient averaged over the isopycnal surface,

$$\phi_d = -\kappa \frac{\mathrm{d}z_*}{\mathrm{d}\theta} \left\langle |\nabla\theta|^2 \right\rangle_{z_*}, \tag{2.18}$$

where ϕ_d is the diapycnal flux, $\kappa = 1.4 \times 10^{-7}$ m^{2}s^{-1} is the constant of molecular diffusivity, z_* is a coordinate representing height of an isopycnal surface after adiabatic resorting, $\nabla\theta$ is

the density gradient along the isopycnal surface, and $\langle\rangle_{z_*}$ represents a spatial average along the constant isopycnal surface. The method for computing the diathermal flux estimate from multiple temperature profiles is described in Winters and D'Asaro (1996) section 7. First, the temperature gradient is computed in both the vertical and horizontal directions, one again using a frozen field hypothesis to convert time to distance by using an average velocity of flow past the T-chain using the ADCP over the time window of interest. Next, the adiabatically-sorted profile of temperature is constructed by sorting all the observed temperatures in a given time window into a stable profile. Practically, this is implemented by assigning the k^{th} temperature in the sorted profile as the average of the $n(k-1)$ through nk warmest temperatures, where n is the number of time steps in the selected time period. This method of computing the mean sorted temperature profile is substantially different from laterally averaging individually sorted profiles. The isopycnal average of temperature gradients $\left\langle |\nabla\theta|^2 \right\rangle_{z_*}$ is then found for each z_* by averaging all the temperature gradients whose corresponding observed temperature falls into the temperature class associated with the given z_*.

The turbulent diffusivity of temperature K_θ is then given by

$$K_\theta \equiv -\phi_d \frac{\mathrm{d}z_*}{\mathrm{d}\theta}. \tag{2.19}$$

Finally, the relation between diathermal flux and buoyancy flux is given by

$$\mathcal{B} = \langle w'b' \rangle = g/\rho_0 \langle w'\rho' \rangle = g\alpha \langle w'T' \rangle = g\alpha\phi_d. \tag{2.20}$$

.

2.5.2 Thorpe scales

The methodology for calculating Thorpe scales was described in Section 2.3. An important detail of our methodology here is that we obtain a profile of Thorpe scales for every

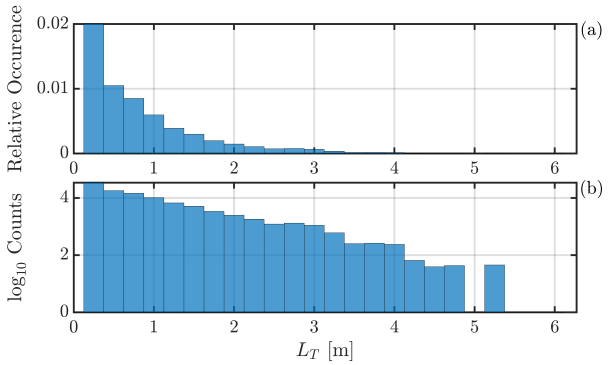

Figure 2.12. Histogram of Thorpe scales L_T observed in the transition layer. (a) Relative occurrence for a given bin is given by the bin counts divided by the total number of grid points within the transition layer. (b) Total counts plotted in log scale to emphasize the slope of the decay and the sparse occurrence of large values.

time, instead of a single value for the transition layer. This allows us to potentially distinguish between two overturns at different depths that are both within the transition layer, or to average over different regions of the transition layer when computing entrainment velocity. Figure 2.12 shows a histogram of Thorpe scales observed in the transition layer. The relative occurrence of 0.25 m overturns, the smallest observable scale, agrees well with Kaminski et al. (2021) for observations of ≥0.25 m overturns. The decay with frequency in overturn size is logarithmic with increasing scale. Note that by binning in two dimensions, we are weighting the observations towards larger scales, since the number of points within a single overturn is proportional to its height.

Estimates of mixing are sensitive to the method for calculating the stratification against which turbulence is working (Winters et al. 1995; Arthur et al. 2017; Kaminski et al. 2021). Convection in the upper mixed layer resulting in mean unstable stratification, the heaving of isotherms at the boundary layer depth due to turbulence, and the heaving of isotherms at the thermocline due to internal waves all complicate the calculation of a mean stratification. We take the following multi-step approach to calculate a reference stratification profile, with the aim of representing stratification computed on isopycnal coordinates. First, we follow the methodology from Winters and D'Asaro (1996) to compute a sorted mean profile from all the temperature

observations within a 1-hour window. A profile of temperature vs mean isotherm depth is constructed by binning depth according to the temperature class of its corresponding unsorted temperature. This profile is sorted to result in a stable profile of temperature vs mean isotherm depth. The vertical temperature gradient at every point is similarly binned by temperature to give a profile of vertical temperature gradient vs mean isotherm depth. The height of the boundary layer is then defined as described in section 2.3 by finding the temperature corresponding to the deepest depth for which the mean temperature gradient exceeds 0.01 K m^{-1}. The boundary layer depth is found at each time as the deepest depth at which this target isotherm appears. Finally, this process is refined by masking the temperature and temperature gradient fields above the boundary layer depth and re-computing the profiles of temperature and temperature gradient vs mean isopycnal depth, along with the boundary layer depth. We find that this approach results in stratification values of up to an order of magnitude higher near the top of the transition layer as compared to more traditional approaches of computing stratification by depth-averaging sorted temperature profiles.

To construct an estimate of $\varepsilon = 0.64 L_T^2 N^3$, the Thorpe scale at every point is combined with the reference stratification corresponding to the observed temperature at that point. This is an important distinction compared to using a depth-based stratification, as a large overturn at the top of the transition layer could be associated with an isopycnal heave of up to 10 m, significantly affecting the reference stratification value used in this calculation.

2.5.3 Comparison of entrainment estimates

We compare the entrainment velocity from the observed mixed layer deepening with that derived using temperature gradients and Thorpe scales, to identify if the turbulent structures observed in the transition layer can explain the mixed layer deepening. Because we observe the transition layer with a large vertical aperture, we need to decide how to ascribe a value to buoyancy flux for every timestep. Based on the scaling in section 2.4 and the shape of the strain and velocity profiles, we expect turbulence and entrainment to be concentrated in the top

of the transition layer. The goal is to average over the turbulence that is contributing toward entrainment. If we look too far into the mixed layer or too far below the transition layer, then the turbulence estimates will not be representative of mixed layer entrainment. The entrainment velocity calculation is also sensitive to the reduced gravity g'. At each timestep, we define

$$g' = g\alpha\Delta T, \tag{2.21}$$

where α is the coefficient of thermal expansion derived from the reference temperature profile and ΔT is the temperature difference in the reference profile over the depth range used to compute buoyancy flux.

The predicted change in mixed layer depth as given by the entrainment velocity is therefore

$$\Delta h(t) \approx \int_0^t w_e(t')\,\mathrm{d}t' = \int_0^t \frac{B(t')}{g'}\,\mathrm{d}t', \tag{2.22}$$

where both B and g' are computed by averaging over some portion of the transition layer. Figure 2.13 (d) compares the observed mixed layer deepening with the deepening rate derived from averaging the temperature gradient method over the whole transition layer, the Thorpe scale estimate averaged over the whole transition layer, and the Thorpe scale method averaged just over the top 5 m of the transition layer. We find that, while averaging over the whole transition layer underestimates the entrainment velocity, confining our estimates to just the top 5 m matches the mixed layer deepening. While the estimates of turbulent diffusivity from these two averaging intervals for Thorpe scales closely agree (Figure 2.13 (d)), their difference in the resulting entrainment velocity calculation are explained by the difference in reduced gravity used in the estimate of entrainment velocity. By confining our estimate to the top of the transition layer in an area of much weaker stratification, the temperature difference is significantly reduced, leading to larger estimated entrainment.

We compare these estimates of entrainment velocity to those calculated from Thorpe

scales by Kaminski et al. (2021), who observed the upper range of the transition layer with an aperture of 1.4 m. Their methodology for calculating Thorpe scales averages sorting distance vertically, resulting in a single Thorpe scale at each time. They find that the bulk of overturning features contributing to their entrainment estimate have vertical scales 10 cm and smaller, which we cannot resolve. We hypothesize that our observations are complementary and both result in reasonable estimates of entrainment velocity because we are resolving different scales and stages of turbulence. Our observations of Thorpe scales are well suited to observing larger overturns in the upper transition layer working against weak stratification, while Kaminski et al. (2021) can only observe smaller overturns in greater stratification due to their limited aperture. Both of these processes may be present during the same mixing, and as they are driven by the same forcing, result in comparable estimates.

By contrast, the temperature gradient estimates following Winters and D'Asaro (1996) underestimate the entrainment velocity, no matter our choice of aperture for the transition layer. The method assumes that the observed gradients are those over which molecular diffusivity is acting to produce a turbulent eddy diffusivity. If the turbulent eddy scale that is driving much of the diffusivity is of a much smaller scale than our resolved overturns, we would not expect to reproduce the correct temperature diffusivity. This interpretation is supported both by previous observations of a rich field of small overturns (Kaminski et al. 2021) as well as by numerical simulations, which show that small secondary instabilities are a primary driver of dissipation (Sarkar and Pham 2019).

2.6 Discussion and Summary

We observe temperature structures at the base of the mixed layer during a variety of forcing conditions using a thermistor chain. Over the course of a storm, we characterize the surface forcing into four regimes based on the relative contribution of wind, wave, and buoyancy forcing to TKE production. During each of those regimes we compare the characteristics of

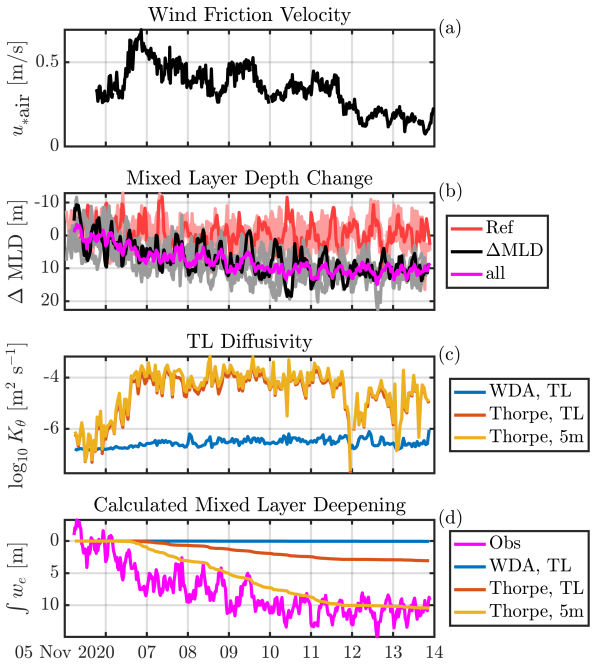

Figure 2.13. Summary of the mixed layer deepening budget. (a) Wind friction velocity. (b) Observed change in mixed layer depth from the T-chain (black) and each of the Wirewalkers (gray), after subtracting internal wave heave of the 13 °C isotherm from the T-chain (red) and Wirewalkers (light red). The average of the observed mixed layer depth change from all instruments is plotted in magenta. Change in mixed layer depth is plotted relative to the initial value of the average from all instruments after applying a three-day lowpass filter. (d) The calculated turbulent diffusivity K_θ from (blue) the Winters and D'Asaro (1996) temperature gradient method averaged over the transition layer, (orange) Thorpe scales, averaging over the transition layer, and (yellow), Thorpe scales, averaging over the range ± 5 m around the depth of the maximum ε. (d) The observed change in mixed layer depth from all instruments (magenta) compared to the integrated entrainment velocity using each of the methods in (c).

coherent turbulent structures in the transition layer. By comparing the bulk shear and stratification profiles, we show that the turbulence is concentrated near the top of the transition layer, and that the observed turbulent structures are comparable to simulations featuring a shear layer in highly asymmetric stratification. Using estimates of buoyancy flux from Thorpe scales, we show that these turbulent structures can account for the observed mixed layer deepening, when confining the entrainment estimate to the top of the transition layer.

In section 2.3, we calculated vertical scales associated with coherent transition layer temperature structures from Gaussian fits to anomalies in boundary layer depth, and to patches of reduced stratification. If these temperature features are indeed related to turbulent overturns, we can think of them as an outer scale to turbulent structures. The timeseries of the amplitudes of boundary layer intrusions seems to follow the wind forcing (Figure 2.14). This observed close relation between the wind forcing amplitude and the amplitude of isothermal heave is consistent with a turbulent length scale driven by wind forcing, $l_e = \frac{u_*}{N_0}$ (Sarkar and Pham 2019).

Using estimates of buoyancy flux from temperature gradients and Thorpe scales, we compare the observed mixed layer deepening rate to the estimated entrainment velocity. We find that our comparison is sensitive to the definition of the transition layer. When averaging over the whole transition layer, Thorpe scales underestimate the entrainment velocity, but when considering only the top of the transition layer, Thorpe scales can explain the entrainment velocity due to a larger reduced gravity over which the buoyancy flux is acting. In comparison to Kaminski et al. (2021), which found that observed mixed layer deepening could be explained by small overturns of < 10 cm scales in high stratification, our deepening rate is explained by large Thorpe scales in much weaker stratification at the top of the transition layer. We consider these observations to be complementary, observing similar mixing dynamics at different scales. Indeed, the existence of an inertial subrange requires equivalence of Ozmidov and Kolmogorov scales when sufficiently averaged. We also attempt to estimate buoyancy flux following the temperature gradient method described in Winters and D'Asaro (1996), but find estimates of temperature diffusivity that are too small to match the entrainment velocity. Higher vertical and

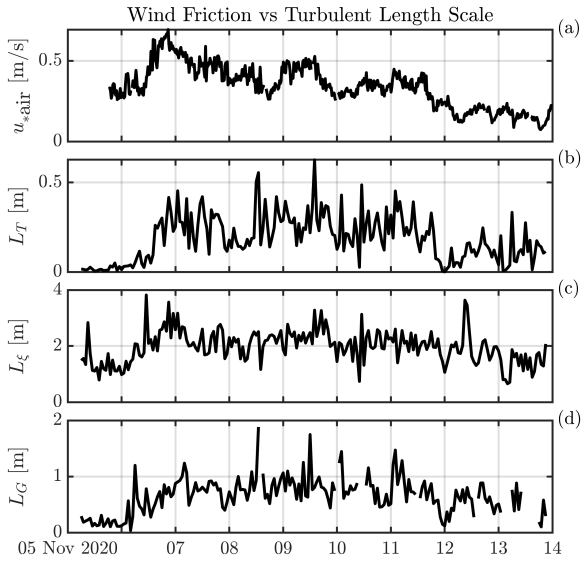

Figure 2.14. Comparison between wind friction velocity (a) and the vertical turbulent length scale from (b) Thorpe scales, (c) the height of negative strain anomaly patches and (d) the amplitude of Gaussian fits to the heave of the top of the transition layer, using 1-hour averages of observed length scales .

temporal resolution would be needed to characterize the small gradients over which diffusion acts to correctly estimate the turbulent diffusivity.

Our findings support a greater need for a diversity of instrumentation and sampling methods for observing the mixed layer. While our T-chain's large aperture enabled us to observe large ($O(10\text{ m})$) coherent structures, we had insufficient vertical resolution to resolve smaller ($O(< 10\text{ cm})$) overturning scales thought to be responsible for high dissipation in high-Re stratified shear turbulence. Our observations complement ongoing modeling efforts to understand mixed layer turbulent dynamics and highlight the need for realistic simulations in complex forcing conditions, like the highly asymmetrically stratified shear layer with varied surface forcing conditions observed here.

2.7 Acknowledgments

Thank you to everyone at the Multiscale Ocean Dynamics group, the Air-Sea Interaction Laboratory, the Coastal Observing Research and Development Center, and the groups of William Hodgkiss and Bill Kuperman, as well as the captains and crews of the *R/V Sally Ride* and the *R/V Bob and Betty Beyster* for the data collected during the TFO 2020 observational campaign. Discussions with Alexis Kaminski, Eric D'Asaro, Sam Lewin, Jerry Smith, and Sutanu Sarkar were very helpful. This research was supported by grants from ONR (N00014-19-1-2635) and NSF (OCE; Grant OCE-2219752 for LL).

Chapter 2, in part, is being prepared for submission for publication fo the material. Andriatis, Alexander, Matthew H. Alford, Luc Lenain, Andrew J. Lucas, Sophia Merrifield. "Observations of turbulent structures at the base of the ocean mixed layer". The dissertation author was the primary investigator and author of this paper.

Chapter 3

Observations of near-inertial wave generation and ζ-refraction from a drifting array

We report observations of near-inertial waves from an array of drifting profiling instruments. Velocity coherence between five drifting Wirewalkers deployed in a 7 km cross pattern is used to estimate inertial wave energy flux and to estimate the impact of array-scale vorticity gradients on near-inertial wave generation and propagation. Near-inertial internal wave kinetic energy is approximately equally partitioned into upward and downward-propagating waves. The downward-propagating waves have significant differences in energy despite the same synoptic wind forcing. The strongest downward-propagating wave is observed towards the side of the array with the most negative vorticity. Upward-going waves, by contrast, are much more coherent across the array. By combining observations of atmospheric forcing with subsurface observations, we construct an inertial kinetic energy budget. We find that about 20% of inertial wind work is radiated into the interior as internal waves. The remaining inertial kinetic energy that is dissipated in the mixed layer accounts for about 10% of the total turbulent kinetic energy production. These observations are complementary to modeling efforts to understand the transfer of wind energy from the ocean surface to the interior.

3.1 Introduction

In the ocean interior, diapycnal mixing is primarily driven by the breaking of internal gravity waves, whose total power input is roughly consistent with averaged turbulent dissipation rates (Waterhouse et al. 2014; MacKinnon et al. 2017). Near-inertial gravity waves (NIWs) are estimated to input a comparable amount of power in the ocean interior ($\mathcal{O}(1$ TW); Alford 2001, 2003a; Watanabe and Hibiya 2002), to internal tides (Melet et al. 2016), and lee waves (Nikurashin and Ferrari 2011). The distribution of internal-wave driven mixing affects its impact on the meridional overturning circulation and the broader climate (MacKinnon et al. 2017).

NIWs are internal gravity waves with frequency near the inertial frequency and a large aspect ratio (Alford et al. 2016), giving a slow vertical group velocity and a preferentially equatorward horizontal group velocity (Alford 2003b), refracted towards regions of lower planetary frequency (D'Asaro et al. 1995). Wind stress at the surface can resonantly force inertial velocities in the OSBL. The finite horizontal scales of a wind event, along with the background mesoscale eddy field (Weller 1982) and variation of inertial frequency with latitude (D'Asaro 1989), lead to horizontal divergences in the inertial velocities that pump the stratified base of the mixed layer at the inertial frequency, with lateral scales of $\mathcal{O}(100$ km) (Gill 1984). This forcing at the base of the mixed layer generates anticyclonic circularly-polarized downward-propagating near-inertial waves. The energy carried by these waves is partitioned according to the vertical modal structure into dissipating locally through wave breaking by strong vertical shear in high wavenumber modes, or into long-range propagation through low wavenumber modes with higher group velocity (Alford 2020a).

Global estimates of the amount of wind work going into NIW generation have large uncertainties due to the treatment of the forcing stress profile in 1-D models (Stokes et al. 2024), the amount of energy lost to turbulence (Alford 2020b), and the effect of the interaction of the submesoscale with inertial oscillations (Asselin and Young 2020). There are few observations which simultaneously observe all the components needed to construct a near-inertial kinetic

energy budget for the conversion of wind work to downward NIW propagation into the interior. Plueddemann and Farrar (2006) construct an IKE balance for observations, a damped slab model, and the PWP model, but did not have observed turbulence estimates. Alford et al. (2012) observed the generation of NIW and their energy flux from a fixed mooring, but without being able to resolve lateral scales of variability. Alford et al. (2017) investigated the space-time scales of shear and NIW flux variability from an array of profiling mooring, finding large lateral coherence scales in NIWs by measuring along isopycnals, but did not relate the energy flux to wind work observations. Recent observations have shown that vorticity gradients in the submesoscale modulate the horizontal wavenumber and direction of NIWs, enhancing downward energy flux in areas of negative vorticity gradient (Thomas et al. 2020; Thomas et al. 2023; Voet et al. 2024).

This study aims to improve our understanding of the relation between wind work and NIW generation by capturing the ocean's response to a storm in the presence of lateral submesoscale vorticity gradients. Our observational campaign is unique in its ability to (1) relate atmospheric forcing to the mixed layer response, turbulence at the base of the mixed layer, and the near-inertial wave field in the ocean interior and (2) to resolve lateral differences in the mixed layer and wave field, along isopycnals, at 7 km scales, all while observing in a semi-Lagrangian reference frame relative to the mean upper-ocean velocity, limiting the effect of lateral advection of spatial gradients.

3.2 Methods

3.2.1 Experiment

The data used in this paper were collected as part of the Task Force Ocean (TFO) "Platform Centric ASW Processing with Through-the-Sensor Data Assimilation and Fusion" experiment off the coast of Southern California in November 2020. The experiment was conducted in deep water off the continental shelf between 5 November and 14 November 2020. This dataset has been used for a complementary study on observations of turbulent structures at the base of the mixed layer

(Andriatis et al., *in prep.*). A second leg to this expedition was conducted between 15 November and 24 November in the Catalina Basin, with observations of Langmuir circulations published in Andriatis et al. (2024). The experiment was based aboard the *R/V Sally Ride*, from which we deployed an array of five drifting Wirewalkers (WWs) (Pinkel et al. 2011), initially arranged in a square measuring 7 km on each side, along with a drifting thermistor chain (T-chain), which was tethered to the central Wirewalker. A remotely-piloted wave glider supported the experiment by performing box-shaped transects around the array of drifting instruments. Instruments were purposefully deployed at the edge of a cyclonic eddy so that they drifted coherently to the north-west for operational requirements. The array deformation and differential drift velocity over the course of the deployment gives a rough estimate of the vorticity, and individual instrument tracks exhibit inertial oscillations in response to wind forcing (Figure 2.1).

3.2.2 Instrumentation

The primary data used in this study come from an array of five drifting Wirewalkers (Pinkel et al. 2011), vertically profiling wave-powered instruments equipped with a CTD and upward-looking ADCP (Figure 3.1). Four of the instruments profiled to 500 m while the fifth went to 200 m. The profile repeat times vary with wave conditions from every 7 minutes for the 200 m configuration during the largest swell to as long as one profile per hour for the 500 m configuration in calm conditions. The array was initially deployed in a square configuration, measuring 7 km on each side. As the array drifted to the north-west in a jet on the edge of a cyclonic eddy, the array both rotated cyclonically and deformed due to a vorticity gradient across the array scale, with WW3, initially on the eastern corner of the array, traveling a smaller distance. The central WW5, which was tethered to a 100 m T-chain, drifted faster than the rest of the array due to its shorter depth and stronger near-surface velocities.

Wirewalker records consist of CTD data during the upward phase of the profiling, and ADCP data during both up and downcasts (Figure 3.2). shows the temperature, salinity, and velocity data from one WW and is representative of the array measurements. During qc, several

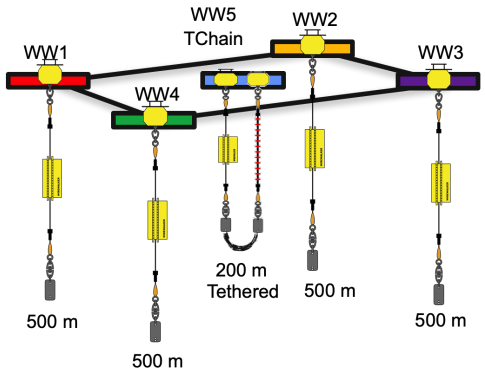

Figure 3.1. Schematic of the drifting Wirewalker and T-chain array. The initial deployment configuration was in a square shape measuring 7 km on each side, with the WW5 and T-chain system at the center. Note that only WW5 and the T-chain are tethered - the other instruments drift independently of one another.

sections of anomalous salinity data at depth, possibly the result of biological contamination, are removed replaced by linear interpolation in time. The gridded ADCP product is constructed by averaging the high-resolution ADCP in time during the up and down profiles, and combining the platform-relative velocity recorded by ADCP with the float motion from GPS (Zheng et al. 2022). Vertical shear is computed from the centered-difference of the velocity, then vertically low-pass filtered with an 8 m cutoff.

For studying internal wave dynamics, data are transformed into isopycnal coordinates (Pinkel 1985) and WKB scaled (Leaman and Sanford 1975). At each timestep, density profiles are sorted to have stable stratification. The reference density profile is constructed from the time-mean of the sorted WW records over the whole deployment (Figure 3.3). To map data into isopycnal coordinates, each variable of interest is binned onto the profile of mean density vs depth using the sorted density field, producing data with a 0.25 m vertical grid for CTD and 1 m vertical grid for ADCP data.

WKB scaling of velocity if given by $u_N = u/\sqrt{\tilde{N}}$, and scaling of shear by $u_{zN} = u_z\sqrt{\tilde{N}}$, where $\tilde{N} \equiv \bar{N}(z)/N_0$ is the scaled stratification profile, computed from the 10-m smoothed mean stratification profile (Figure 3.4). The WKB-scaled depth coordinate is given by $z_N = \int_0^z \tilde{N}\,\mathrm{d}z$. Note that for WW5, the scaling is not strictly WKB, because the total scaling does not vertically

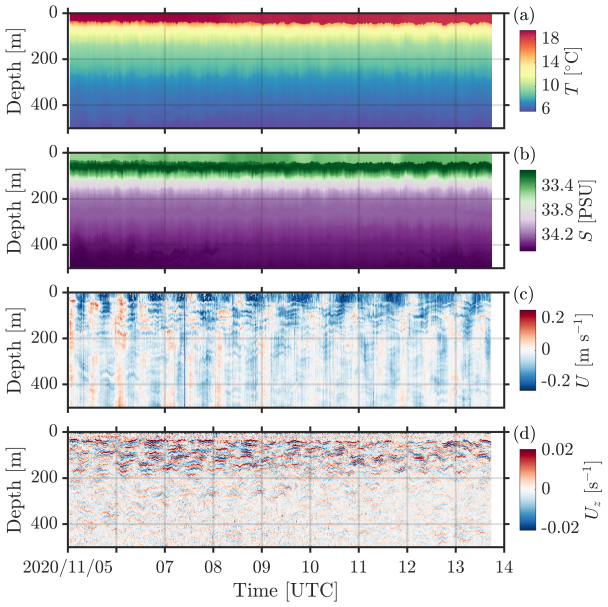

Figure 3.2. Summary of observed fields for WW1, representative of all WW observations. (a) In-situ temperature, (b) salinity, (c) zonal velocity, and (d) vertical shear of zonal velocity.

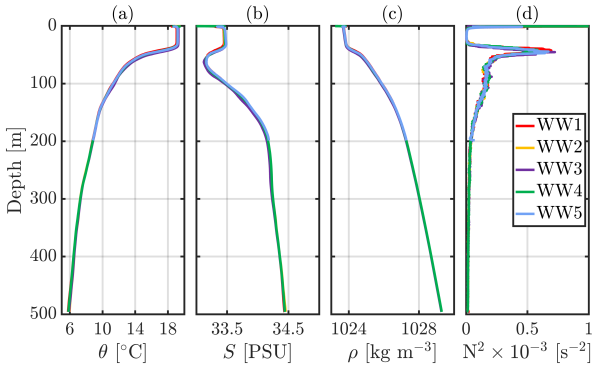

Figure 3.3. Mean profiles of sorted CTD variables for each WW. (a) Conservative temperature, (b) absolute salinity, (c) density, and (d) stratification.

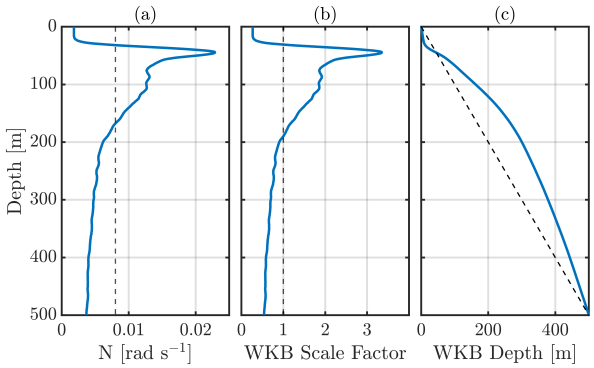

Figure 3.4. Reference profiles used for WKB scaling for all of the Wirewalkers. (a) Mean stratification across all the observations $\bar{N}(z)$, with vertical mean stratification N_0 (dashed line). (b) WKB scale factor $\tilde{N}$. (c) WKB-scaled depth coordinate z_N, compared to unscaled depth (dashed line).

average to zero. However, by using the same scaling across the array we are able to directly compare velocities along isopycnals at the same scaled depth.

A T-chain consisting of 58 thermistors was tethered to WW5 by a 200 m long chain connecting the base of the two instruments. Thermistors were placed between the surface float and 100 m depth with nominal thermistor spacing was every 3.5 m, with a dense section of 0.5 m spacing near the base of the mixed layer. An upward-looking Teledyne Workhorse 300 kHz ADCP was mounted at 100 m depth at the base of the T-chain, giving velocity data with 1 m vertical bins at 0.5 Hz. During the day, biological scatterers move to the base of the mixed layer, resulting in low correlation values in the mixed layer. A gridded temperature product with 0.25 m vertical bins and 10 s time bins is constructed from the thermistor data by using the heave of the T-chain by surface waves as a synthetic profiler. Further details on the T-chain data are provided in Andriatis et al., *in prep.*. The main data used from the T-chain in this study are estimates of turbulent kinetic energy dissipation, ε, from Thorpe scales in the transition layer to use in the kinetic energy budget.

Atmospheric and surface forcing observations were collected from the *Sally Ride* and a remotely-piloted Liquid Robotics SV3 wave glider. The wave glider was equipped with a meteorological package and flow-through CTD, an upward-looking Signature 1000 ADCP on

the subsurface platform and downward-looking ADCP mounted on the surface float (Grare et al. 2021; Hodges et al. 2023). The *Sally Ride* provided observations of atmospheric conditions - air temperature, humidity, pressure, and precipitation, along with downwelling solar shortwave and longwave radiation. A flow-through CTD system recorded ocean temperature and salinity at 5 m depth. The wave glider arrived in the experiment region shown in Figure 2.1 on Nov 09, but was within 200 km of the array for the duration of the observations. Given the large synoptic scale of the atmospheric forcing and the similarity between the *Sally Ride* and wave glider meteorological observations, we take the wave glider observations as representative of the atmospheric forcing at the array, and prefer to use wind speed from the wave glider, as the *Sally Ride* wind observations are sometimes contaminated by wind shadow effects due to its hull.

3.3 Mixed Layer Kinetic Energy Budget

The mixed layer inertial kinetic energy budget is constructed by combining observations of atmospheric forcing from the wave glider and *Sally Ride* with observations of the inertial mixed layer response from Wirewalkers, turbulence estimates from the T-chain and estimates of downward NIW energy flux into the ocean interior from Wirewalkers. The OSBL near-inertial kinetic energy (IKE) budget can be written as

$$\frac{\partial \mathrm{IKE}}{\partial t} = \Pi_I - P_M - F_I, \tag{3.1}$$

where Π_I is power input into near-inertial oscillations by the wind, P_M is the rate of energy lost to turbulence, and F_I is the power of energy flux into the interior, carried by near-inertial waves (D'Asaro 1985; Crawford and Large 1996; Plueddemann and Farrar 2006; Alford 2020b).

Shortly after instruments were deployed, a storm passed by the experiment region. Winds (U_{10}) increased from about 8 m s^{-1} to a maximum of 15 m s^{-1} during 6 November, followed by a decay to 4 m s^{-1} on 14 November (Figure 3.6 (a)). A wind stress at the surface will accelerate horizontal velocity, transferring wind energy into the ocean at a rate Π_I, with time-varying stress

near the inertial frequency having the greatest resonant effect. The near-inertial wind power is given by

$$\Pi_I = \boldsymbol{\tau} \cdot \boldsymbol{u}_I \tag{3.2}$$

where $\boldsymbol{\tau}$ is the wind stress vector and $\boldsymbol{u}_I$ is the near-inertial surface current, defined as having frequencies within $\{0.9, 1.15\}\, f$ following Alford et al. 2012. Stress has units of $[\tau] = \text{N m}^{-2}$, giving $[\tau u] = \text{W m}^{-2}$.

Wind stress is calculated from wave glider wind observations using the COARE algorithm (Fairall et al. 2003). Near-inertial surface currents are derived from observations of velocity in the mixed layer from the Wirewalker ADCP records. The repeat time of Wirewalker profiles ($\sim$ 15 minutes) is short relative to the inertial period ($\sim$ 23 hours), giving well-resolved inertial currents and isopycnal displacements. Velocity is generally uniform throughout the mixed layer and oscillates at approximately the inertial frequency plus a background velocity associated with the submesoscale jet. The rotation of currents can be seen by taking the rotary spectrum of horizontal velocity, $z = u + iv$ (Figure 3.5) (Mooers 1970; Gonella 1972). Near $\omega \approx 1/23$ hr^{-1}, clockwise (anticyclonic) rotation is an order of magnitude more energetic than counter-clockwise motion, with the difference diminishing at both low frequencies ($\omega < 1/2.5$ day^{-1}) and high frequencies ($\omega > 1/5$ hr^{-1}).

To isolate the near-inertial velocities $\boldsymbol{u_I}$ the rotary velocity is band-pass filtered around the clockwise inertial frequency. The near-inertial wind work Π_I is then calculated as the inner product of wind stress and near-inertial velocity. Wind work inputs energy into inertial motions when inertial velocity is aligned with the stress direction, and extracts energy when stress and velocity are opposed. The cumulative energy input by the wind is given by the time integral of wind work $\int \Pi_I \, \mathrm{d}t$ (Figure 3.6(b)). Total observed energy input was about 250 J m^{-2}.

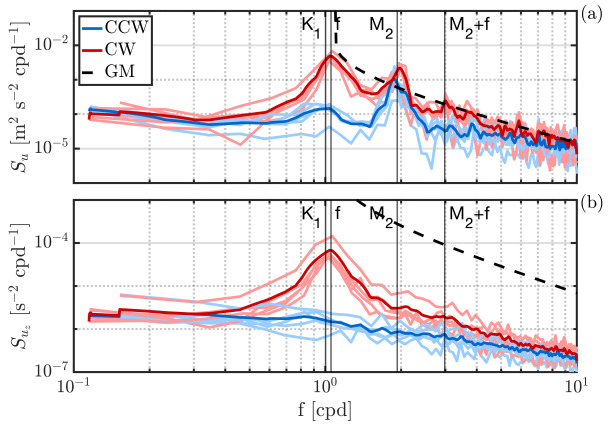

Figure 3.5. Rotary frequency spectrum of velocity (a) and shear (b) from each of the Wirewalkers (thin) and average across instruments (bold), separated into clockwise (red) and counter-clockwise (blue) rotations. The reference Garret-Munk (GM) spectrum is given in a dashed black line, and selected frequencies of interest are highlighted.

The inertial kinetic energy is

$$\text{IKE} = \frac{1}{2}\rho_0 h\left(u_I^2 + v_I^2\right), \tag{3.3}$$

where ρ_0 is the mixed layer average density and h is the mixed layer depth, giving units of J m^{-2} so that its time derivative is consistent with the other budget terms. IKE computed from mean mixed layer inertial currents increased due to the energy input by the wind during the storm and decayed as winds subsided (Figure 3.6(c)). The initial rate of increase in IKE is comparable to the energy input over the same time period, but reached a maximum of about half the total integrated wind work before decaying.

Because our observations started only shortly before the peak of the wind, in already moderately strong wind forcing (10 m s^{-1}), we compare our observed cumulative wind work and IKE response with a damped slab model (Pollard and Millard 1970). We force a slab model using wind speed from ERA5 reanalysis, interpolated onto the center of the experiment region, starting on 25 October during wind speeds < 1 m s^{-1}, until the end of the observation period on 14 November, using a Rayleigh damping of $r = 1/6.6$ days. ERA5 wind speed closely matches observations. The slab model does not produce a significant wind work input or IKE response

until 06 Nov (Figure 3.6(c, gray)). The timing of the inertial response to wind forcing, and the absence of a response in the 10 days prior to the start of observations establishes confidence that pulses of downward-propagating NIWs seen in the observations just below the mixed layer would not have been generated from a previous wind event not captured by observations. The damping parameter was chosen so that the maximum IKE response is of approximately the same magnitude as observations. The IKE increase occurs a day earlier than observations however, and decays more rapidly. The total inertial wind work input as a result of the storm is about twice the observed amplitude.

The rate of turbulent kinetic energy production, P_M, is balanced by dissipation of turbulent kinetic energy, ϵ, and buoyancy flux resulting from the entrainment at the base of the mixed layer , J_b, giving

$$P_M = \epsilon + J_b, \tag{3.4}$$

where $J_b = \overline{w'b'}$ (Plueddemann and Farrar 2006; Alford 2020b). While near-inertial motions generate shear-driven turbulence and entrainment, they are not singularly responsible for these processes. Rather, buoyancy flux and dissipation are part of the overall turbulent kinetic energy (TKE) budget in the OSBL, which extracts energy from the total kinetic energy of the boundary layer, and includes dynamics such as TKE production by wind shear, convective instability, wave breaking, and Langmuir turbulence. Calculating the OSBL TKE budget has been the subject of recent literature (Zippel et al. 2022) and is beyond the scope of this analysis. We can nevertheless calculate ϵ and J_b, and compare the total P_M to the residual from the other terms in the IKE budget. The ratio

$$\frac{\Pi_I - \partial_t \mathrm{IKE} - F_I}{P_M} \tag{3.5}$$

should provide insight into what fraction of TKE production is driven by inertial wind work

relative to other processes.

We have previously estimated the rate of kinetic energy dissipation from T-chain observations in Andriatis et al., *in prep.* from Thorpe scale estimates, $\varepsilon \approx 0.64 L_T^2 N^3$. We found average dissipation values of $\varepsilon = 1 \times 10^{-7}$ m^2 s^{-3} when averaging over the top of the transition layer during the time period of the greatest mixed layer deepening. For a flux coefficient of $\Gamma = 0.2$ the Thorpe scale estimates of ε in the transition layer can explain an entrainment velocity that agrees with the observed mixed layer deepening. The lateral advection of observed gradients in mixed layer depth is negligible. Assuming this TKE dissipation is representative of the rest of the mixed layer gives a mixed layer-integrated value of $\epsilon = \rho_0 h \varepsilon = 4 \times 10^{-3}$ W m^{-2}.

Our observations lack measurements of vertical velocity that would be necessary to directly measure buoyancy flux. We can, however, follow Alford 2020b in calculating buoyancy flux as the rate of increase of potential energy

$$J_b = \frac{\mathrm{d}}{\mathrm{d}t}\mathrm{PE}, \quad \text{with} \quad \mathrm{PE} = \int_D^0 \rho(z) g z \, \mathrm{d}z, \tag{3.6}$$

where D is a depth well below the mixed layer. The timeseries of potential energy anomaly are highly variable due to internal wave heaving (Figure 3.6(g)). Fitting a linear trend during the period of mixed layer deepening yields a mean entrainment buoyancy flux of about 2×10^{-3} W m^{-2}. A net outward surface heat flux of 3×10^3 J m^{-2} results in a similar potential energy contribution of 2×10^{-3} W m^{-2} (Figure 3.6(d)).

The final component of the NIW energy budget is the downward NIW energy flux into the interior, F_I. The flux of wave energy can be written as $\boldsymbol{F} = \overline{\boldsymbol{u} p}$, the correlation between velocity and pressure, with time averaging over the wave period, or $\boldsymbol{F} = \boldsymbol{c}_g E$, wave energy carried by the group velocity. As with most observations, our measurements of vertical velocity and pressure are insufficiently precise or dense to directly measure vertical flux of near-inertial wave energy F_I. Instead, we calculate the flux by estimating the group velocity and kinetic energy of the most prominent downward -propagating wave packet (Figure 3.10), giving an order of magnitude

estimate of $F_I \approx 1 \times 10^{-4}$ W m^{-2}.

To summarize, our mixed layer kinetic energy budget consists of: A mean wind work of about 250 J m^{-2} over 6 days, giving $\Pi_I \approx 5 \times 10^{-4}$ W m^{-2}. The mean entrainment buoyancy flux based on the increase in potential energy is $J_b \approx 2 \times 10^{-3}$ W m^{-2}, which is approximately same as the mean surface buoyancy flux $J_0 \approx 2 \times 10^{-3}$ W m^{-2}. Mean TKE dissipation is $\epsilon \approx 4 \times 10^{-3}$ W m^{-2} based on Thorpe scales at the base of the transition layer. Estimated downward NIW energy flux is $F_I \approx 1 \times 10^{-4}$ W m^{-2}. The net inertial kinetic energy change is near-zero, but we note that its peak was about half as large as the total inertial wind work.

The fraction of wind work going into NIW generation, $F_I/\Pi_I \approx 20\%$, is complementary to estimates from one-dimensional models such as a range of 15-40% from Alford (2020b) or 70% from Stokes et al. (2024). The total TKE production term $P_M \approx 6 \times 10^{-3}$ W m^{-2} is roughly an order of magnitude larger than the inertial wind work.

3.4 Downward NIWs and Vorticity Gradients

Timeseries of shear from the Wirewalkers are decomposed into upward and downward-going energy. We compute the two-dimensional rotary shear spectrum from WKB-stretched velocities on isopycnal coordinates following Pinkel (2008) and Alford et al. (2017), and take the negative frequency, negative wavenumber quadrant as the downward-going energy, with negative frequency, positive wavenumber quadrant as upward-going energy. Patterns of coherent shear bands with upward-sloping phase lines are obsevrved at all five WWs in the WKB-scaled depth range 60 - 300 m (Figure 3.7). Below this range, the shear bands become incoherent.

The NIW field exhibits a striking difference between the five WWs given their small spatial separation. NIWs are traditionally thought of as having large horizontal wavelengths due to coherent inertial oscillations that shrink with time due to lateral variability in the Coriolis parameter, known as the β-effect (D'Asaro 1989). Enhanced shear magnitude in Wirewalker 3 between 05 and 10 Nov in the 100 to 200 m depth range relative to the other Wirewalkers is a

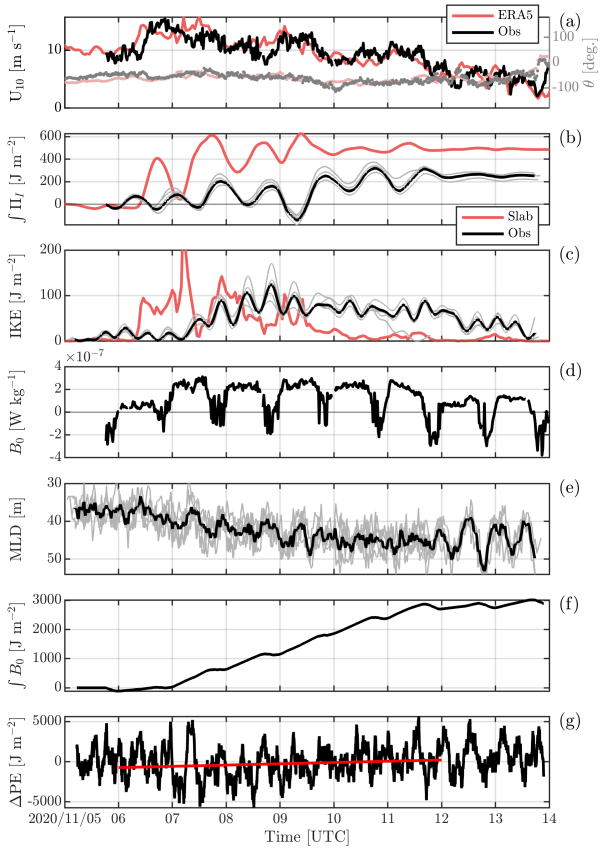

Figure 3.6. (a) Wind speed (lines) and direction (light dots), (b) integrated wind work, (c) inertial kinetic energy, (d) surface buoyancy flux, (e) mixed layer depth, (f) integrated surface buoyancy flux, and (g) change in potential energy at 60 m depth relative to its mean during the observation period, with a linear fit during the mixed layer deepening (red). Individual WW obs. are shown in gray, with mean over all WWs in black. ERA5 wind speed (a) and slab model forced by ERA5 winds (b,c) are shown in red.

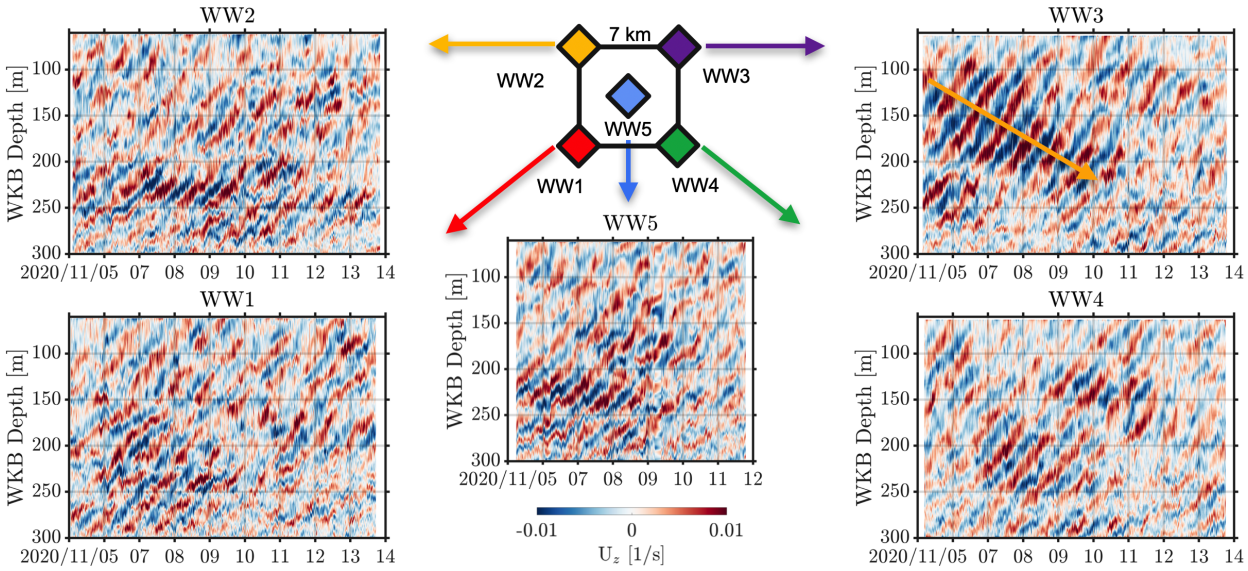

Figure 3.7. Downward component of vertical shear of zonal velocity from each Wirewalker, in WKB-stretched isopycnal coordinates. A pronounced packet of downward-propagating NIW is emphasized in the WW3 record with an orange arrow.

clear signal of a downward-propagating NIW whose lateral scale is smaller than the array size (Figure 3.7).

We turn to recent theory and observations of the effect of background vorticity on NIW propagation from (Asselin et al. 2020) and (Thomas et al. 2020) to explain the mechanism that would lead to differences in the NIW field at these scales. Vorticity was calculated by fitting a plane to observations of velocity (Davies-Jones 1993; Zeiden et al. 2022) at each depth and time across the Wirewalker array, along isopycnals. The uncertainty in the vorticity is calculated following Spydell et al. (2019, eq. 16), using a velocity uncertainty error of $\sigma_u = 0.06$ ms^{-1}, which is estimated from the variability of Wirewalker velocity observations at their Nyquist frequency. This method yields a vorticity error of about $\sigma_\zeta \approx 0.2f$. Reduction in the error is obtained by time and depth-averaging. For time averaging, we assume that consecutive velocity observations are independent, so that the error goes as $1/\sqrt{N_t}$, with Nt the number of observations in a time window. For depth averaging, an initial estimate for the decorrelation scale is about $\delta_z = 12$ m in the thermocline, while in the mixed layer we assume vertically uniform flow. In the thermocline the resulting scale factor for the is $1/\sqrt{N_z}$ with $N_z = \Delta z/\delta_z$, where Δz is the

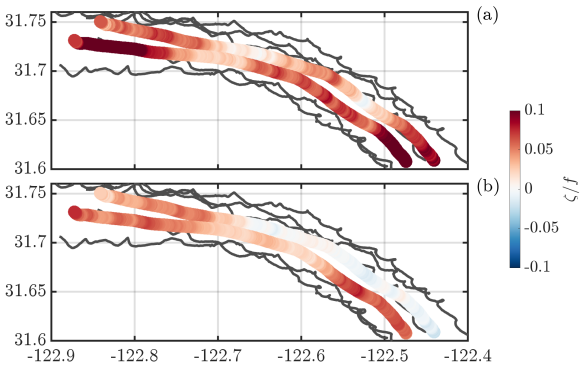

Figure 3.8. Vorticity determined by plane fits to WWs 1, 2, and 4 (south-west track) and WWs 2, 3, and 4 (north-east track), in the mixed layer between 10-30 m (a) and thermocline between 50-150 m (b), with 1-day temporal smoothing.

averaging depth range.

By comparing the vorticity estimate from different combinations of Wirewalker observations, we calculate the spatial gradient in vorticity (Figure 3.8). By comparing multiple combinations together we obtain a vorticity gradient magnitude and direction (Figure 3.9). A significant vorticity gradient is observed in both the mixed layer and in the thermocline until about 09 November. In the mixed layer, however, the down-gradient direction appears to be toward the north-east, rotating toward the east, while the thermocline vorticity gradient is down-gradient toward the southeast, rotating toward the east. After about 12 Nov the vorticity estimates become unreliable due to the array deformation, leading to growth in the vorticity error. The timing of the vorticity gradient coincides with the enhanced downward wave packet observed at WW3.

We are now interested in finding the horizontal wavenumber of this wave packet to determine whether the observed vorticity gradient could result in the appropriate wavenumber growth in a reasonable time from wave generation, $\mathbf{k}_h(\mathbf{x},t) = -\frac{t}{2}\nabla_h\bar{\zeta}(\mathbf{x},t)$ (Thomas et al. 2020). To find the frequency and vertical wavenumber, we fit a plane wave to the shear, of the form $\mathbf{u}_z = \mathbf{c} + a\cos(\omega_o t + mz + \phi)$, where the zonal and meridional shear are allowed to have different constant offsets, and are constrained to have their phase be 90° out of phase, $\phi = (\phi_u, \phi_u + \pi/2)$. Fitting is initially done manually, forming an initial guess that is passed to an optimizer. The best-fit plane wave is found to have $\omega_o = 0.99f$ and $\lambda_z = 64$ m (Figure 3.10).

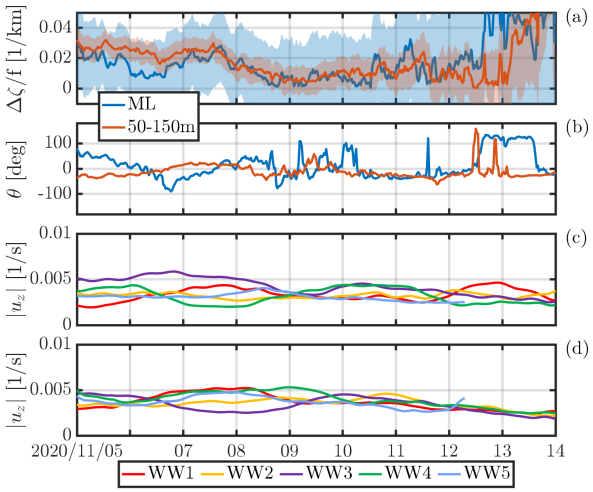

Figure 3.9. (a) Horizontal vorticity gradient magnitude and (b) the down-gradient direction. (c) Downward shear magnitude, averaged over 100-250 WKB m and (d) upward shear magnitude, averaged over 60-150 WKB m.

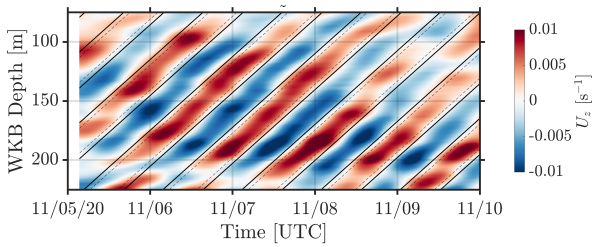

Figure 3.10. Plane wave fit to the downward component of shear in WW3, on isopycnal WKB coordinates.

We estimate the vertical group speed of the wave packet,

$$c_{g,z} \approx -\frac{N^2 k_h^2}{f m^3}, \tag{3.7}$$

by tracking the deepening of the packet's energy from 120 m to 180 m depth in three days, giving group speed $c_{g,z} \approx 20$ m/day. Using characteristic values of $N^2 = 2 \times 10^{-4}$ (rad/sec)^2, $f = 1.05 \times 2\pi$ rad/day, and $m = 2\pi/64$ m, we estimate a horizontal wavenumber of 2.9×10^{-4} rad/m, giving a horizontal wavelength of 21.7 km. For a horizontal vorticity gradient of $0.1f$ per 5 km, we can expect this wavenumber to be realized 4.4 days after generation.

The horizontal wavenumber can alternatively be estimated from looking at horizontal differences in the shear phase (Thomas et al. 2020),

$$k_h = \frac{\Delta \phi_{shear}}{\Delta x}, \tag{3.8}$$

with $\phi_{shear} = \tan^{-1}(v_z/u_z)$. At the start of the wind forcing on 06 Nov, the downward shear phase is uniform across the array (Figure 3.11). By 08 Nov, however, the array has developed significant shear phase differences. For instance, WW1 is about $\pi/4$ out of sync with WW3, which, given a 10 km separation, implies 80 km horizontal wavelength.

This approach can be further expanded by fitting plane waves to the shear phase to find horizontal wavenumber from shear phase gradient, in the same way that vorticity was determined from plane fits to array velocity (Figure 3.12). This method can resolve wavenumbers that are of array-scale or larger, but will alias larger wavenumbers. For downward-going waves, this method identifies a region of high wavenumbers between 05 Nov and 08 Nov at around 200 to 300 m WKB depth, with an approximate wavelength of 15 km. Indeed, one can see a signature of this wave packet in the shear plots at all of the Wirewalkers (Figure 3.7). By contrast, the energetic wave packet identified at WW3 and discussed in Figure 3.10 does not appear to have a clear signature in this method, which would be consistent with it having a much smaller wavelength

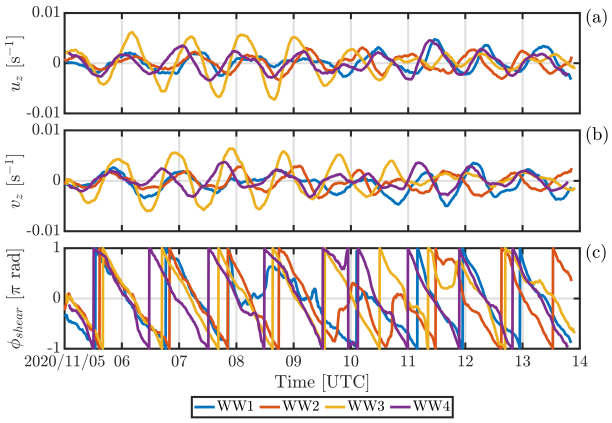

Figure 3.11. Downward-propagating component of (a) zonal and (b) meridional shear at the 170 m_{WKB} isopycnal, averaged over ±8 m, smoothed with a moving mean window of 1/4 inertial period width. (c) Shear phase difference.

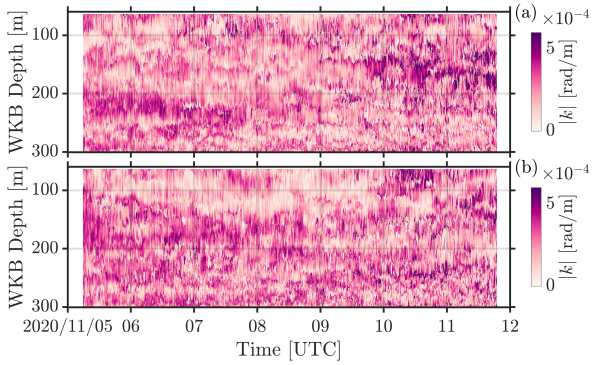

Figure 3.12. Wavenumber magnitude from multi-ww plane fits to shear phase for (a) down and (b) up-propagating NIWs.

than the array scale.

3.5 Upward NIWs

Another striking feature of these data is the near-surface intensification of up-going NIW energy (Figure 3.13). Across the entire array, a signature of upwards-propagating NIWs appears to be enhanced between 50 and 150 WKB m relative to the rest of the field, and is of the same order of magnitude as the down-propagating waves. The shear phase fit shows that in this depth range, across most of the deployment, the wavenumber is around 1×10^{-4} rad m^{-1} or smaller, giving a wavelength of 60 km or larger. The possible sources and significance of the upward

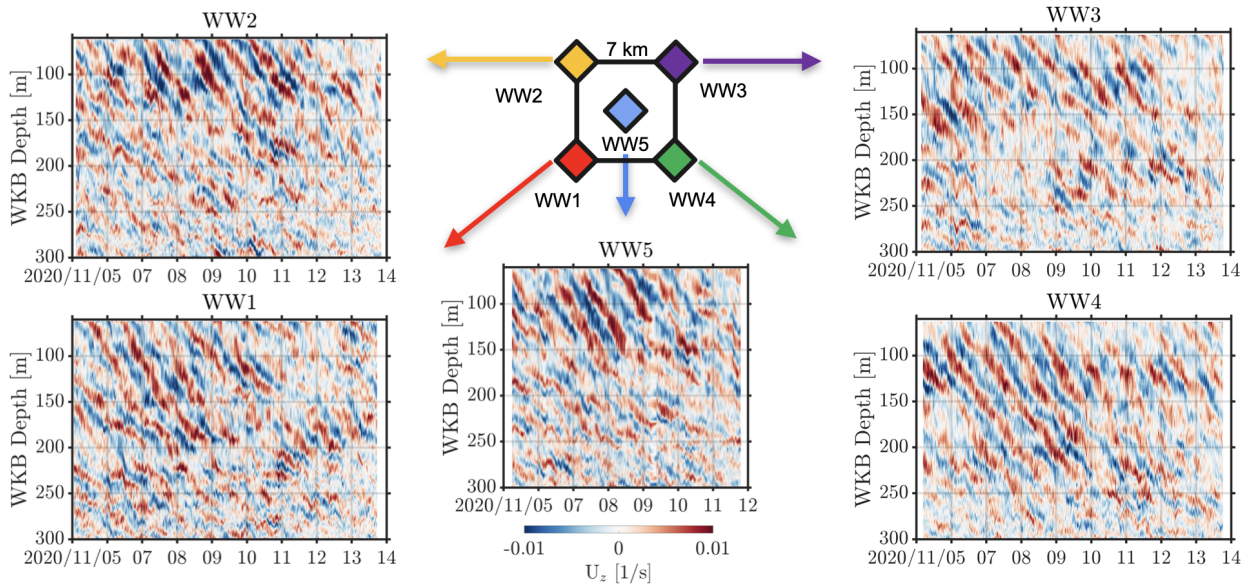

Figure 3.13. Upward component of vertical shear of zonal velocity from each Wirewalker, in WKB-stretched isopycnal coordinates.

component of NIW energy will be explored in a future study.

3.6 Discussion and Summary

We observed the generation of NIWs during a 9-day experiment in deep water offshore of Southern California from an array of drifting Wirewalkers. By decomposing the observed timeseries of shear into upward and downward-propagating waves using a rotary shear spectrum, we find that energy in the upward and downward-propagating directions is approximately equally partitioned. Velocity coherence across the instrument array is used to determine inertial wave energy flux and to estimate the impact of array-scale vorticity gradients on near-inertial wave generation and propagation.

By comparing the magnitude of vertical shear along isopycnals across the array, we identify significant differences in downward-propagating near-inertial internal wave energy at 7 km array scale, despite coherent wind forcing in the region. The strongest downward-propagating wave is observed towards the side of the array with the most negative vorticity. This observation is consistent with ζ-refraction, which predicts a growth rate in wavenumber proportional to the

negative vorticity gradient (Asselin et al. 2020; Thomas et al. 2020).

We combine observations of atmospheric forcing with observations of the mixed layer's response of inertial velocity and estimates of turbulent production to construct an inertial kinetic energy budget. The fraction of wind work that goes into forcing downward near-inertial waves appears to be about 20%, when considering the strongest observed near-inertial wave packet. Observations of buoyancy flux are of the same magnitude as estimates of TKE dissipation, which together give a total TKE production term that is about an order of magnitude larger than the portion of inertial kinetic energy that is dissipated in the mixed layer.

These observations highlight the large variability in near-inertial ocean response to wind forcing, and our ability to observe these scales using a novel deployment of drifting profiling instruments. Further campaigns to simultaneously observe ocean surface forcing and the subsurface response of the mixed layer and radiated near-inertial waves can improve estimates of the global ocean energy budget due to wind forcing.

3.7 Acknowledgments

Thank you to everyone at the Multiscale Ocean Dynamics group, the Air-Sea Interaction Laboratory, the Coastal Observing Research and Development Center, and the groups of William Hodgkiss and Bill Kuperman, as well as the captains and crews of the *R/V Sally Ride* and the *R/V Bob and Betty Beyster* for the data collected during the TFO 2020 observational campaign. Discussions with Jerry Smith and Rob Pinkel were very helpful. This research was supported by grants from ONR (N00014-19-1-2635) and NSF (OCE; Grant OCE-2219752 for LL).

Chapter 3, in part, is being prepared for submission for publication fo the material. Andriatis, Alexander, Matthew H. Alford, Luc Lenain, Andrew J. Lucas, Sophia Merrifield. " Observations of near-inertial wave generation and ζ-refraction from a drifting array". The dissertation author was the primary investigator and author of this paper.

Appendix A

Supplemental information for Chapter 1

A.1 2D Temperature Wavenumber Spectra and LC Scales

To create temperature wavenumber spectra, composite IR images and x-y LES temperature fields are 2-D Fourier transformed using 50-m square segments with 50% overlap, Hann windows, and zero-padding. A sample of the 2-D Fourier transform of the IR image of Figure 1.8, panel c, is shown in Figure A.1 . To find the orientation of the Langmuir cells, the radial-average PSD is made using 5-degree bins, averaging over wavelengths from 1 to 50 m. A Gaussian is fit to the radial average, with the prominence of the Gaussian peak giving a measure of the relative LC signature, while the width gives a measure of the directional certainty. For segments with prominent LCs, the peak in the spectrum has a definite direction, while the absence of LCs results in isotropically-distributed variance. To emphasize the scale of Langmuir circulations, an angular average of the directional spectrum is taken in the cross-wave direction, as defined by the peak direction of the Gaussian fit ± the full width at half maximum (FWHM), and compared to the angular average in the along-wave direction and the omnidirectional spectrum (Figure 1.8 b,d,f). The normal to the cross-cell direction fit is also used to reconstruct the wind direction for Figure 1.6, assuming that LCs are oriented along-wind.

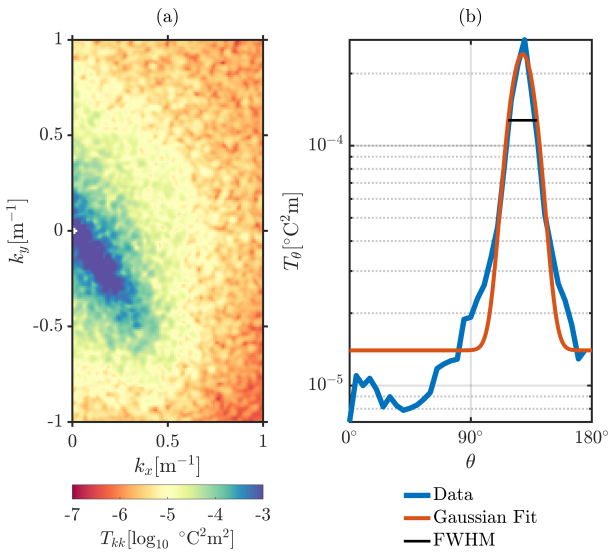

Figure A.1. (a) 2D spectrum of an IR image with Langmuir cells, panel c in Figure 1.8. (b) Radial-average of the 2D spectrum between 1 m and 50 m length scales, in 5-degree bins, with a Gaussian fit.

A.2 Timeseries of Scaling Parameters

Timeseries of the scaling parameters plotted in Figure 1.5 are provided in Figure A.2 for reference.

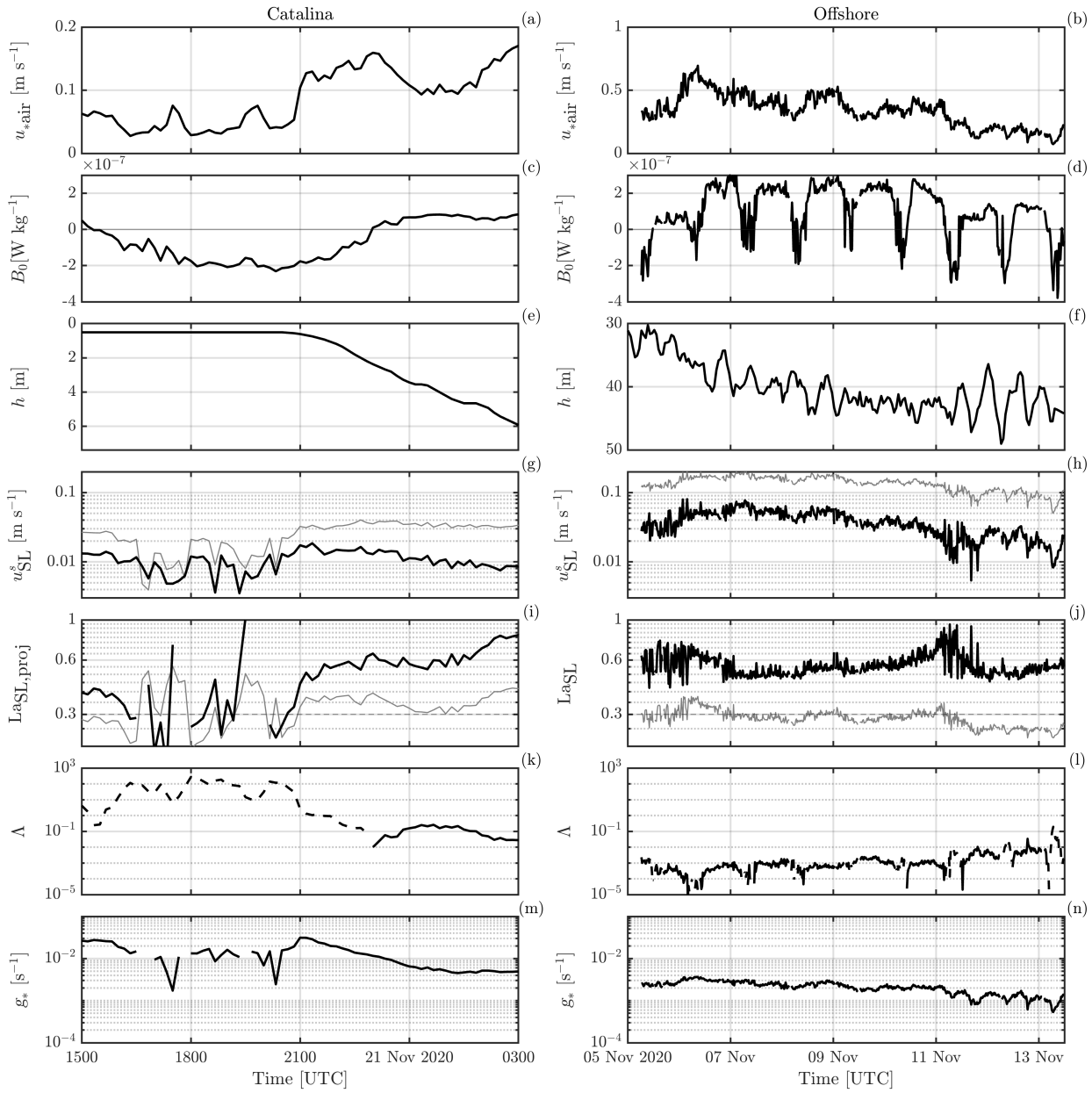

Figure A.2. Scale analysis of the forcing in (left) the Catalina basin and (right) the Offshore experiment. (a,b) Wind friction velocity in air $u_{*\mathrm{air}}$. (c,d) Surface buoyancy flux B_0. (e,f) Boundary layer depth h. (g,h) Surface layer Stokes drift u^s_{SL} (black) and surface Stokes drift u_{s0} (gray). (i,j) Surface layer projected turbulent Langmuir number $\mathrm{La}_{\mathrm{SL,proj}}$ (black) and La_t (gray). (k,l) Stability parameter Λ, with periods of stabilizing forcing ($\Lambda > 0$) shown as a dashed line. (m,n) LC growth timescale g_*.

Appendix B

Supplemental information for Chapter 2

B.1 Gaussian Fitting to Boundary Layer Heave

We used Gaussian fits to the depth of the boundary layer to systematically characterize the heave of the boundary layer due to turbulence. For an hour-long observation time window, the boundary layer depth is defined by the isopycnal whose mean depth matches the maximum depth for which the mean stratification exceeds 0.01 K m^{-1}, using the deepest isopycnal depth for times when the target isopycnal depth is multi-valued. The mean stratification is constructed as described in section 2.5.2, by binning instantaneous vertical temperature gradients by their associated temperature, into bins defined by the sorted profile of temperature vs mean isopycnal depth.

Anomalies in the boundary layer depth are defined relative to the mean depth of the target isopycnal during the 1-hour window. Working in a coordinate system relative to the 10-minute smoothed depth of the thermocline (depth of maximum stratification), we interpret negative (shallow) anomalies of boundary isopycnal depth as the signature of transition layer turbulence pushing stratified water upwards into the mixed layer. To identify the height of the anomaly and relate it to turbulent forcing, we fit a Gaussian to each continuous segment of negative depth anomaly which is at least four time bin (40 seconds) long (Figure B.1). Each Gaussian fit was constrained to to have a base equal to the 90^{th} percentile of the boundary isopycnal depth.

To ascribe a single vertical turbulent scale for the one-hour segment, we calculate, for

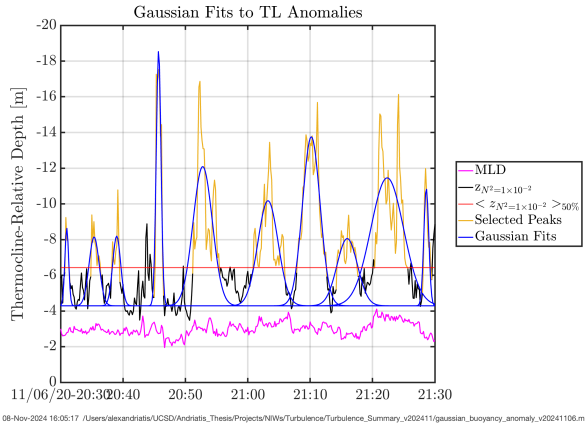

Figure B.1. Example of Gaussian fits to segments of isopycnal displacement in the transition layer. The black contour follows the isotherm whose mean depth is equal to the mean depth of the T_z=0.01 °C m^{-1} stratification level. Each continuous segment where the depth of the isotherm exceeds its mean (yellow) is fit with a Gaussian (blue). The vertical displacement of the Gaussian is constrained to be equal to the 90th percentile of isotherm depth. The depth of the mixed layer (pink) is shown for reference.

each profile, the vertical distance between the shallowest Gaussian fit in the profile and the Gaussian floor. The mean of each of these vertical distances over the one-hour segment defines the Gaussian fit outer turbulent scale for the segment.

Bibliography

Alford, Matthew H. 2020a. "Global calculations of local and remote near-inertial-wave dissipation." *J. Phys. Oceanogr.* 50 (11): 3157–3164. https://doi.org/10.1175/JPO-D-20-0106.1.

———. 2020b. "Revisiting near-inertial wind work: slab models, relative stress and mixed-layer deepening." *J. Phys. Oceanogr.* 50 (11): 3141–3156. https://doi.org/10.1175/JPO-D-20-0105.1.

———. 2001. "Internal Swell Generation: The Spatial Distribution of Energy Flux from the Wind to Mixed Layer Near-Inertial Motions." *Journal of Physical Oceanography* 31 (8): 2359–2368. https://doi.org/10.1175/JPO-D-20-0106.1.

———. 2003a. "Improved global maps and 54-year history of wind-work on ocean inertial motions." *Geophysical Research Letters* 30 (8). https://doi.org/10.1029/2002gl016614.

———. 2003b. "Redistribution of energy available for ocean mixing by long-range propagation of internal waves." *Nature* 423 (6936): 159–162. https://doi.org/10.1038/nature01628.

Alford, Matthew H., Meghan F Cronin, and Jody M Klymak. 2012. "Annual Cycle and Depth Penetration of Wind-Generated Near-Inertial Internal Waves at Ocean Station Papa in the Northeast Pacific." *J. Phys. Oceanogr.* 42 (6): 889–909. https://doi.org/10.1175/JPO-D-11-092.1.

Alford, Matthew H., Jennifer A. MacKinnon, Robert Pinkel, and Jody M. Klymak. 2017. "Space-Time Scales of Shear in the North Pacific." *Journal of Physical Oceanography* 47 (10): 2455–2478. https://doi.org/10.1175/JPO-D-17-0087.1.

Alford, Matthew H., Jennifer A. MacKinnon, Harper L. Simmons, and Jonathan D. Nash. 2016. "Near-Inertial Internal Gravity Waves in the Ocean." *Annual Review of Marine Science* 8 (1): 95–123. https://doi.org/10.1146/annurev-marine-010814-015746.

Ali, Alfatih, Kai H. Christensen, Øyvind Breivik, Mika Malila, Roshin P. Raj, Laurent Bertino, Eric P. Chassignet, and Mostafa Bakhoday-Paskyabi. 2019. "A comparison of Langmuir turbulence parameterizations and key wave effects in a numerical model of the North Atlantic and Arctic Oceans." *Ocean Modelling* 137:76–97. https://doi.org/10.1016/j.ocemod.2019.02.005.

Andriatis, Alexander, Luc Lenain, Matthew H. Alford, Nathaniel Winstead, and Joseph Geiman. 2023. "Data from: Observations and Numerical Simulations of the Onset and Growth of Langmuir Circulations." *UC San Diego Library Digital Collections,* https://doi.org/10.6075/J0VQ32W2.

———. 2024. "Observations and Numerical Simulations of the Onset and Growth of Langmuir Circulations." *Journal of Physical Oceanography* 54 (8): 1737–1763. https://doi.org/10.1175/jpo-d-24-0004.1.

Arthur, Robert S., Subhas K. Venayagamoorthy, Jeffrey R. Koseff, and Oliver B. Fringer. 2017. "How we compute N matters to estimates of mixing in stratified flows." *Journal of Fluid Mechanics* 831. https://doi.org/10.1017/jfm.2017.679.

Asselin, Olivier, Leif N Thomas, William R Young, and Luc Rainville. 2020. "Refraction and Straining of Near-Inertial Waves by Barotropic Eddies." *Journal of Physical Oceanography* 50 (12): 3439–3454. https://doi.org/10.1175/JPO-D-20-0109.1.

Asselin, Olivier, and William R. Young. 2020. “Penetration of Wind-Generated Near-Inertial Waves into a Turbulent Ocean.” *Journal of Physical Oceanography* 50 (6): 1699–1716. https://doi.org/10.1175/jpo-d-19-0319.1.

Beare, Robert J., Malcolm K. Macvean, Albert A. M. Holtslag, Joan Cuxart, Igor Esau, Jean-Christophe Golaz, Maria A. Jimenez, Marat Khairoutdinov, Branko Kosovic, David Lewellen, Thomas S. Lund, Julie K. Lundquist, Anne Mccabe, Arnold F. Moene, Yign Noh, Siegfried Raasch, and Peter Sullivan. 2006. “An Intercomparison of Large-Eddy Simulations of the Stable Boundary Layer.” *Boundary-Layer Meteorology* 118 (2): 247–272. https://doi.org/10.1007/s10546-004-2820-6.

Belcher, Stephen E., Alan L. M. Grant, Kirsty E. Hanley, Baylor Fox-Kemper, Luke Van Roekel, Peter P. Sullivan, William G. Large, Andy Brown, Adrian Hines, Daley Calvert, Anna Rutgersson, Heidi Pettersson, Jean-Raymond Bidlot, Peter A. E. M. Janssen, and Jeff A. Polton. 2012. “A global perspective on Langmuir turbulence in the ocean surface boundary layer.” *Geophysical Research Letters* 39 (18). https://doi.org/10.1029/2012gl052932.

Boyer Montégut, Clément de, Gurvan Madec, Albert S. Fischer, Alban Lazar, and Daniele Iudicone. 2004. “Mixed layer depth over the global ocean: An examination of profile data and a profile-based climatology.” *Journal of Geophysical Research: Oceans* 109 (C12). https://doi.org/10.1029/2004JC002378.

Breivik, Øyvind, Jean-Raymond Bidlot, and Peter A.E.M. Janssen. 2016. “A Stokes drift approximation based on the Phillips spectrum.” *Ocean Modelling* 100:49–56. https://doi.org/10.1016/j.ocemod.2016.01.005.

Breivik, Øyvind, and Kai H. Christensen. 2020. “A Combined Stokes Drift Profile under Swell and Wind Sea.” *Journal of Physical Oceanography* 50 (10): 2819–2833. https://doi.org/10.1175/jpo-d-20-0087.1.

Breivik, Øyvind, Peter A. E. M. Janssen, and Jean-Raymond Bidlot. 2014. "Approximate Stokes Drift Profiles in Deep Water." *Journal of Physical Oceanography* 44 (9): 2433–2445. https://doi.org/10.1175/jpo-d-14-0020.1.

Chang, Henry, Helga S. Huntley, A. D. Kirwan, Daniel F. Carlson, Jean A. Mensa, Sanchit Mehta, Guillaume Novelli, Tamay M. Özgökmen, Baylor Fox-Kemper, Brodie Pearson, Jenna Pearson, Ramsey R. Harcourt, and Andrew C. Poje. 2019. "Small-Scale Dispersion in the Presence of Langmuir Circulation." *Journal of Physical Oceanography* 49 (12): 3069–3085. https://doi.org/10.1175/jpo-d-19-0107.1.

Chini, G. P., and S. Leibovich. 2003. "Resonant Langmuir-circulation–internal-wave interaction. Part 1. Internal wave reflection." *Journal of Fluid Mechanics* 495:35–55. https://doi.org/10.1017/s0022112003006074.

Chor, Tomas, James C. McWilliams, and Marcelo Chamecki. 2021. "Modifications to the K-Profile Parameterization with Nondiffusive Fluxes for Langmuir Turbulence." *Journal of Physical Oceanography* 51 (5): 1503–1521. https://doi.org/10.1175/jpo-d-20-0250.1.

Ciappa, Achille, and Luca Pietranera. 2013. "High resolution observations of the Terra Nova Bay polynya using COSMO-SkyMed X-SAR and other satellite imagery." *Journal of Marine Systems* 113-114:42–51. https://doi.org/10.1016/j.jmarsys.2012.12.004.

Colosi, Luke, Nick Pizzo, Laurent Grare, Nick Statom, and Luc Lenain. 2023. "Observations of Surface Gravity Wave Spectra from Moving Platforms." *Journal of Atmospheric and Oceanic Technology,* https://doi.org/10.1175/jtech-d-23-0022.1.

Cózar, Andrés, Stefano Aliani, Oihane C. Basurko, Manuel Arias, Atsuhiko Isobe, Konstantinos Topouzelis, Anna Rubio, and Carmen Morales-Caselles. 2021. "Marine Litter Windrows: A Strategic Target to Understand and Manage the Ocean Plastic Pollution." *Frontiers in Marine Science* 8. https://doi.org/10.3389/fmars.2021.571796.

Craik, A. D. D., and S. Leibovich. 1976. “A rational model for Langmuir circulations.” *Journal of Fluid Mechanics* 73 (3): 401–426. https://doi.org/10.1017/s0022112076001420.

Crawford, G. B., and W. G. Large. 1996. “A Numerical Investigation of Resonant Inertial Response of the Ocean to Wind Forcing.” *Journal of Physical Oceanography* 26 (6): 873–891. https://doi.org/10.1175/1520-0485(1996)026⟨0873:ANIORI⟩2.0.CO;2.

Cronin, MF, and J Sprintall. 2009. “Wind-and buoyancy-forced upper ocean.” *Elements of Physical Oceanography: A derivative of the Encyclopedia of Ocean Sciences,* 237–245.

D’Asaro, E. 1985. “The energy flux from the wind to near-inertial motions in the mixed layer.” *J. Phys. Oceanogr.* 15 (8): 1043–1059. https://doi.org/10.1175/1520-0485(1985)015⟨1043:TEFFTW⟩2.0.CO;2.

D’Asaro, E. A., J. Thomson, A. Y. Shcherbina, R. R. Harcourt, M. F. Cronin, M. A. Hemer, and B. Fox-Kemper. 2014. “Quantifying upper ocean turbulence driven by surface waves.” *Geophysical Research Letters* 41 (1): 102–107. https://doi.org/10.1002/2013gl058193.

D’Asaro, Eric A. 1989. “The decay of wind-forced mixed layer inertial oscillations due to the β effect.” *Journal of Geophysical Research: Oceans* 94 (C2): 2045–2056. https://doi.org/10.1029/JC094iC02p02045.

D’Asaro, Eric A, C E Eriksen, M D Levine, P Niiler, C A Paulson, and P V Meurs. 1995. “Upper-ocean inertial currents forced by a strong storm, Part I, Data and comparisons with linear theory.” *J. Phys. Oceanogr.* 25:2909–2936. https://doi.org/10.1175/1520-0485(1995)025⟨2909:UOICFB⟩2.0.CO;2.

Davies-Jones, Robert. 1993. “Useful, Formulas for Computing Divergence, Vorticity, and Their Errors from Three or More Stations.” *Monthly Weather Review* 121 (3): 713–725. https://doi.org/10.1175/1520-0493(1993)121⟨0713:UFFCDV⟩2.0.CO;2.

Deardorff, James W. 1970. “A numerical study of three-dimensional turbulent channel flow at large Reynolds numbers.” *Journal of Fluid Mechanics* 41 (2): 453–480. https://doi.org/10.1017/s0022112070000691.

Dierssen, H.M., A. Chlus, and B. Russell. 2015. “Hyperspectral discrimination of floating mats of seagrass wrack and the macroalgae Sargassum in coastal waters of Greater Florida Bay using airborne remote sensing.” *Remote Sensing of Environment* 167:247–258. https://doi.org/10.1016/j.rse.2015.01.027.

Dohan, Kathleen, and Russ E. Davis. 2011. “Mixing in the Transition Layer during Two Storm Events.” *Journal of Physical Oceanography* 41 (1): 42–66. https://doi.org/10.1175/2010jpo4253.1.

Dorrell, Robert M., Charlie J. Lloyd, Ben J. Lincoln, Tom P. Rippeth, John R. Taylor, Colmcille P. Caulfield, Jonathan Sharples, Jeff A. Polton, Brian D. Scannell, Deborah M. Greaves, Rob A. Hall, and John H. Simpson. 2022. “Anthropogenic Mixing in Seasonally Stratified Shelf Seas by Offshore Wind Farm Infrastructure.” *Frontiers in Marine Science* 9. https://doi.org/10.3389/fmars.2022.830927.

Drucker, Robert. 2003. “Observations of ice thickness and frazil ice in the St. Lawrence Island polynya from satellite imagery, upward looking sonar, and salinity/temperature moorings.” *Journal of Geophysical Research* 108 (C5). https://doi.org/10.1029/2001jc001213.

Fairall, C. W., E. F. Bradley, J. E. Hare, A. A. Grachev, and J. B. Edson. 2003. “Bulk Parameterization of Air and Sea Fluxes: Updates and Verification for the COARE Algorithm.” *Journal of Climate* 16 (4): 571–591. https://doi.org/10.1175/1520-0442(2003)016⟨0571:bpoasf⟩2.0.co;2.

Fan, Yalin, Zhitao Yu, Ivan Savelyev, Peter P. Sullivan, Jun-Hong Liang, Tracy Haack, Eric Terrill, Tony de Paolo, and Kipp Shearman. 2020. "The effect of Langmuir turbulence under complex real oceanic and meteorological forcing." *Ocean Modelling* 149:101601. https://doi.org/10.1016/j.ocemod.2020.101601.

Farmer, David, and Ming Li. 1995. "Patterns of Bubble Clouds organized by Langmuir Circulation." *Journal of Physical Oceanography* 25 (6): 1426–1440. https://doi.org/10.1175/1520-0485(1995)025⟨1426:pobcob⟩2.0.co;2.

Ferrari, Raffaele, and Giulio Boccaletti. 2004. "Eddy-Mixed Layer Interactions in the Ocean." *Oceanography* 17 (3): 12–21. https://doi.org/10.5670/oceanog.2004.26.

Fox-Kemper, Baylor, Leah Johnson, and Fangli Qiao. 2022. "Ocean near-surface layers." In *Ocean Mixing,* 65–94. Elsevier. https://doi.org/10.1016/b978-0-12-821512-8.00011-6.

Gargett, A., J. Wells, A. E. Tejada-Martínez, and C. E. Grosch. 2004. "Langmuir Supercells: A Mechanism for Sediment Resuspension and Transport in Shallow Seas." *Science* 306 (5703): 1925–1928. https://doi.org/10.1126/science.1100849.

Gargett, A. E., and C. E. Grosch. 2014. "Turbulence Process Domination under the Combined Forcings of Wind Stress, the Langmuir Vortex Force, and Surface Cooling." *Journal of Physical Oceanography* 44 (1): 44–67. https://doi.org/10.1175/jpo-d-13-021.1.

Gargett, AE, DK Savidge, and JR Wells. 2014. "Anatomy of a Langmuir supercell event." *Journal of Marine Research* 72 (3): 127–163.

Gargett, Ann E. 2022. "Forcing Space: An Alternative to Regime Diagrams for Predicting Characteristics of Turbulence in the Ocean Surface Mixing Layer." *Journal of Physical Oceanography* 52 (3): 519–535. https://doi.org/10.1175/jpo-d-21-0145.1.

Gargett, Ann E., and Judith R. Wells. 2007. "Langmuir turbulence in shallow water. Part 1. Observations." *Journal of Fluid Mechanics* 576:27–61. https://doi.org/10.1017/s0022112006004575.

Gemmrich, Johannes R., and David M. Farmer. 1999. "Near-Surface Turbulence and Thermal Structure in a Wind-Driven Sea." *Journal of Physical Oceanography* 29 (3): 480–499. https://doi.org/10.1175/1520-0485(1999)029⟨0480:nstats⟩2.0.co;2.

Gill, A. E. 1984. "On the Behavior of Internal Waves in the Wakes of Storms." *Journal of Physical Oceanography* 14 (7): 1129–1151. https://doi.org/10.1175/1520-0485(1984)014⟨1129:otboiw⟩2.0.co;2.

Gonella, Joseph. 1972. "A rotary-component method for analysing meteorological and oceanographic vector time series." *Deep Sea Research and Oceanographic Abstracts* 19 (12): 833–846. https://doi.org/10.1016/0011-7471(72)90002-2.

Grant, Alan L. M., and Stephen E. Belcher. 2009. "Characteristics of Langmuir Turbulence in the Ocean Mixed Layer." *Journal of Physical Oceanography* 39 (8): 1871–1887. https://doi.org/10.1175/2009jpo4119.1.

Grare, Laurent, Nicholas M. Statom, Nick Pizzo, and Luc Lenain. 2021. "Instrumented Wave Gliders for Air-Sea Interaction and Upper Ocean Research." *Frontiers in Marine Science* 8. https://doi.org/10.3389/fmars.2021.664728.

Gregg, Michael C, Eric A D'Asaro, James J Riley, and Eric Kunze. 2018. "Mixing efficiency in the ocean." *Annual review of marine science* 10 (1): 443–473. https://doi.org/10.1146/annurev-marine-121916-063643.

Harcourt, Ramsey R., and Eric A. D'Asaro. 2008. "Large-Eddy Simulation of Langmuir Turbulence in Pure Wind Seas." *Journal of Physical Oceanography* 38 (7): 1542–1562. https://doi.org/10.1175/2007jpo3842.1.

Hodges, Benjamin A., Laurent Grare, Benjamin Greenwood, Kayli Matsuyoshi, Nick Pizzo, Nicholas M. Statom, J. Thomas Farrar, and Luc Lenain. 2023. "Evaluation of Ocean Currents Observed from Autonomous Surface Vehicles." *Journal of Atmospheric and Oceanic Technology* 40 (10): 1121–1136. https://doi.org/10.1175/jtech-d-23-0066.1.

Hughes, Kenneth G., James N. Moum, and Emily L. Shroyer. 2020. "Evolution of the Velocity Structure in the Diurnal Warm Layer." *Journal of Physical Oceanography* 50 (3): 615–631. https://doi.org/10.1175/jpo-d-19-0207.1.

Jochum, Markus, B P Briegleb, Gokhan Danabasoglu, W G Large, S R Jayne, Matthew H Alford, and F O Bryan. 2012. "On the impact of oceanic near-inertial waves on climate." *J. Climate* 26 (9): 2833–2844. https://doi.org/10.1175/JCLI-D-12-00181.1.

Johnson, Leah, Baylor Fox-Kemper, Qing Li, Hieu T. Pham, and Sutanu Sarkar. 2023. "A Finite-Time Ensemble Method for Mixed Layer Model Comparison." *Journal of Physical Oceanography* 53 (9): 2211–2230. https://doi.org/10.1175/jpo-d-22-0107.1.

Johnston, T. M. Shaun, and Daniel L. Rudnick. 2009. "Observations of the Transition Layer." *Journal of Physical Oceanography* 39 (3): 780–797. https://doi.org/10.1175/2008jpo3824.1.

Kaminski, A. K., and W. D. Smyth. 2019. "Stratified shear instability in a field of pre-existing turbulence." *Journal of Fluid Mechanics* 862:639–658. https://doi.org/10.1017/jfm.2018.973.

Kaminski, Alexis K., Eric A. D'Asaro, Andrey Y. Shcherbina, and Ramsey R. Harcourt. 2021. "High-resolution observations of the North Pacific transition layer from a Lagrangian float." *Journal of Physical Oceanography,* https://doi.org/10.1175/jpo-d-21-0032.1.

Kenyon, Kern E. 1969. "Stokes drift for random gravity waves." *Journal of Geophysical Research* 74 (28): 6991–6994. https://doi.org/10.1029/jc074i028p06991.

Klymak, Jody M., Robert Pinkel, and Luc Rainville. 2008. "Direct Breaking of the Internal Tide near Topography: Kaena Ridge, Hawaii." *Journal of Physical Oceanography* 38 (2): 380–399. https://doi.org/10.1175/2007jpo3728.1.

Kukulka, T., A. J. Plueddemann, and P. P. Sullivan. 2013. "Inhibited upper ocean restratification in nonequilibrium swell conditions." *Geophysical Research Letters* 40 (14): 3672–3676. https://doi.org/10.1002/grl.50708.

Kukulka, T., A. J. Plueddemann, J. H. Trowbridge, and P. P. Sullivan. 2009. "Significance of Langmuir circulation in upper ocean mixing: Comparison of observations and simulations." *Geophysical Research Letters* 36 (10). https://doi.org/10.1029/2009gl037620.

———. 2011. "The influence of crosswind tidal currents on Langmuir circulation in a shallow ocean." *Journal of Geophysical Research* 116 (C8). https://doi.org/10.1029/2011jc006971.

Kukulka, Tobias, Albert J. Plueddemann, John H. Trowbridge, and Peter P. Sullivan. 2010. "Rapid Mixed Layer Deepening by the Combination of Langmuir and Shear Instabilities: A Case Study." *Journal of Physical Oceanography* 40 (11): 2381–2400. https://doi.org/10.1175/2010jpo4403.1.

Langmuir, Irving. 1938. "Surface Motion of Water Induced by Wind." *Science* 87 (2250): 119–123. https://doi.org/10.1126/science.87.2250.119.

Large, W. G., J. C. McWilliams, and S. C. Doney. 1994. “Oceanic vertical mixing: A review and a model with a nonlocal boundary layer parameterization.” *Reviews of Geophysics* 32 (4): 363–403. https://doi.org/10.1029/94rg01872.

Large, William G., Gokhan Danabasoglu, Scott C. Doney, and James C. McWilliams. 1997. “Sensitivity to Surface Forcing and Boundary Layer Mixing in a Global Ocean Model: Annual-Mean Climatology.” *Journal of Physical Oceanography* 27 (11): 2418–2447. https://doi.org/10.1175/1520-0485(1997)027⟨2418:stsfab⟩2.0.co;2.

Larson, K. J. 1992. “Riding Langmuir circulations and swimming in circles: a novel form of clustering behavior by the scyphomedusa Linuche unguiculata.” *Marine Biology* 112 (2): 229–235. https://doi.org/10.1007/bf00702466.

Leaman, K. D., and Thomas B Sanford. 1975. “Vertical Energy Propagation of Inertial Waves: A Vector Spectral Analysis of Velocity Profiles.” *J. Geophys. Res.* 80 (15): 1975–1978. https://doi.org/10.1029/JC080i015p01975.

Lenain, Luc, and W. Kendall Melville. 2017. “Measurements of the Directional Spectrum across the Equilibrium Saturation Ranges of Wind-Generated Surface Waves.” *Journal of Physical Oceanography* 47 (8): 2123–2138. https://doi.org/10.1175/jpo-d-17-0017.1.

Lenain, Luc, and Nick Pizzo. 2020. “The Contribution of High-Frequency Wind-Generated Surface Waves to the Stokes Drift.” *Journal of Physical Oceanography* 50 (12): 3455–3465. https://doi.org/10.1175/jpo-d-20-0116.1.

Lenain, Luc, Nicholas M. Statom, and W. Kendall Melville. 2019. “Airborne Measurements of Surface Wind and Slope Statistics over the Ocean.” *Journal of Physical Oceanography* 49 (11): 2799–2814. https://doi.org/10.1175/jpo-d-19-0098.1.

Li, Ming, Chris Garrett, and Eric Skyllingstad. 2005. "A regime diagram for classifying turbulent large eddies in the upper ocean." *Deep Sea Research Part I: Oceanographic Research Papers* 52 (2): 259–278. https://doi.org/10.1016/j.dsr.2004.09.004.

Li, Ming, Konstantin Zahariev, and Chris Garrett. 1995. "Role of Langmuir Circulation in the Deepening of the Ocean Surface Mixed Layer." *Science* 270 (5244): 1955–1957. https://doi.org/10.1126/science.270.5244.1955.

Li, Qing, and Baylor Fox-Kemper. 2017. "Assessing the Effects of Langmuir Turbulence on the Entrainment Buoyancy Flux in the Ocean Surface Boundary Layer." *Journal of Physical Oceanography* 47 (12): 2863–2886. https://doi.org/10.1175/jpo-d-17-0085.1.

Li, Qing, Baylor Fox-Kemper, Øyvind Breivik, and Adrean Webb. 2017. "Statistical models of global Langmuir mixing." *Ocean Modelling* 113:95–114. https://doi.org/10.1016/j.ocemod.2017.03.016.

Li, Qing, Brandon G. Reichl, Baylor Fox-Kemper, Alistair J. Adcroft, Stephen E. Belcher, Gokhan Danabasoglu, Alan L. M. Grant, Stephen M. Griffies, Robert Hallberg, Tetsu Hara, Ramsey R. Harcourt, Tobias Kukulka, William G. Large, James C. McWilliams, Brodie Pearson, Peter P. Sullivan, Luke Van Roekel, Peng Wang, and Zhihua Zheng. 2019. "Comparing Ocean Surface Boundary Vertical Mixing Schemes Including Langmuir Turbulence." *Journal of Advances in Modeling Earth Systems* 11 (11): 3545–3592. https://doi.org/10.1029/2019ms001810.

Li, Qing, Adrean Webb, Baylor Fox-Kemper, Anthony Craig, Gokhan Danabasoglu, William G. Large, and Mariana Vertenstein. 2016. "Langmuir mixing effects on global climate: WAVEWATCH III in CESM." *Ocean Modelling* 103:145–160. https://doi.org/10.1016/j.ocemod.2015.07.020.

Longuet-Higgins, Michael S. 1996. "Surface manifestations of turbulent flow." *Journal of Fluid Mechanics* 308:15–29. https://doi.org/10.1017/s0022112096001371.

Lucas, Natasha S., Alan L. M. Grant, Tom P. Rippeth, Jeff A. Polton, Matthew R. Palmer, Liam Brannigan, and Stephen E. Belcher. 2019. “Evolution of Oceanic Near-Surface Stratification in Response to an Autumn Storm.” *Journal of Physical Oceanography* 49 (11): 2961–2978. https://doi.org/10.1175/JPO-D-19-0007.1.

Lueck, Rolf, Ilker Fer, Cynthia Bluteau, Marcus Dengler, Peter Holtermann, Ryuichiro Inoue, Arnaud LeBoyer, Sarah-Anne Nicholson, Kirstin Schulz, and Craig Stevens. 2024. “Best practices recommendations for estimating dissipation rates from shear probes.” *Frontiers in Marine Science* 11:1334327. https://doi.org/10.3389/fmars.2024.1334327.

MacKinnon, Jennifer A., Zhongxiang Zhao, Caitlin B. Whalen, Amy F. Waterhouse, David S. Trossman, Oliver M. Sun, Louis C. St. Laurent, Harper L. Simmons, Kurt Polzin, Robert Pinkel, Andrew Pickering, Nancy J. Norton, Jonathan D. Nash, Ruth Musgrave, Lynne M. Merchant, Angelique V. Melet, Benjamin Mater, Sonya Legg, William G. Large, Eric Kunze, Jody M. Klymak, Markus Jochum, Steven R. Jayne, Robert W. Hallberg, Stephen M. Griffies, Steve Diggs, Gokhan Danabasoglu, Eric P. Chassignet, Maarten C. Buijsman, Frank O. Bryan, Bruce P. Briegleb, Andrew Barna, Brian K. Arbic, Joseph K. Ansong, and Matthew H. Alford. 2017. “Climate Process Team on Internal-Wave Driven Ocean Mixing.” *Bulletin of the American Meteorological Society* 98 (11): 2429–2454. https://doi.org/10.1175/bams-d-16-0030.1.

Marmorino, G.O., G.B. Smith, and G.J. Lindemann. 2005. “Infrared imagery of large-aspect-ratio Langmuir circulation.” *Continental Shelf Research* 25 (1): 1–6. https://doi.org/10.1016/j.csr.2004.08.002.

Marmorino, George O., Geoffrey B. Smith, Jakov V. Toporkov, Mark A. Sletten, Dragana Perkovic, and Stephen J. Frasier. 2008. “Evolution of ocean slicks under a rising wind.” *Journal of Geophysical Research* 113 (C4). https://doi.org/10.1029/2007jc004538.

Marmorino, George O., Jakov V. Toporkov, Geoffrey B. Smith, Mark A. Sletten, Dragana Perkovic, Stephen Frasier, and K. Peter Judd. 2007. "Ocean Mixed-Layer Depth and Current Variation Estimated From Imagery of Surfactant Streaks." *IEEE Geoscience and Remote Sensing Letters* 4 (3): 364–367. https://doi.org/10.1109/lgrs.2007.895702.

McWilliams, J. C., Peter P. Sullivan, and Chin-Hoh Moeng. 1997. "Langmuir turbulence in the ocean." *Journal of Fluid Mechanics* 334:1–30. https://doi.org/10.1017/s0022112096004375.

McWilliams, James C., Edward Huckle, Junhong Liang, and Peter P. Sullivan. 2014. "Langmuir Turbulence in Swell." *Journal of Physical Oceanography* 44 (3): 870–890. https://doi.org/10.1175/jpo-d-13-0122.1.

McWilliams, James C., and Peter P. Sullivan. 2000. "Vertical Mixing by Langmuir Circulations." *Spill Science & Technology Bulletin* 6 (3-4): 225–237. https://doi.org/10.1016/s1353-2561(01)00041-x.

Melet, Angelique, Sonya Legg, and Robert Hallberg. 2016. "Climatic impacts of parameterized local and remote tidal mixing." *Journal of Climate* 29 (2016): 3473–3500. https://doi.org/10.1175/JCLI-D-15-0153.1.

Melville, W. Kendall, Luc Lenain, Daniel R. Cayan, Mati Kahru, Jan P. Kleissl, P. F. Linden, and Nicholas M. Statom. 2016. "The Modular Aerial Sensing System." *Journal of Atmospheric and Oceanic Technology* 33 (6): 1169–1184. https://doi.org/10.1175/jtech-d-15-0067.1.

Melville, W. Kendall, Robert Shear, and Fabrice Veron. 1998. "Laboratory measurements of the generation and evolution of Langmuir circulations." *Journal of Fluid Mechanics* 364:31–58. https://doi.org/10.1017/s0022112098001098.

Min, Hong Sik, and Yign Noh. 2004. “Influence of the Surface Heating on Langmuir Circulation.” *Journal of Physical Oceanography* 34 (12): 2630–2641. https://doi.org/10.1175/jpojpo-2654.1.

Moeng, Chin-Hoh. 1984. “A Large-Eddy-Simulation Model for the Study of Planetary Boundary-Layer Turbulence.” *Journal of the Atmospheric Sciences* 41 (13): 2052–2062. https://doi.org/10.1175/1520-0469(1984)041⟨2052:alesmf⟩2.0.co;2.

Mooers, C. N. K. 1970. “The interaction of an internal tide with the frontal zone in a coastal upwelling region.” PhD diss., Oregon State University.

Nikurashin, Maxim, and Raffaele Ferrari. 2011. “Global energy conversion rate from geostrophic flows into internal lee waves in the deep ocean.” *Geophys. Res. Lett.* 38 (L08610): doi:10.1029/2011GL046576.

Noh, Yign, Gahyun Goh, Siegfried Raasch, and Micha Gryschka. 2009. “Formation of a Diurnal Thermocline in the Ocean Mixed Layer Simulated by LES.” *Journal of Physical Oceanography* 39 (5): 1244–1257. https://doi.org/10.1175/2008jpo4032.1.

Osborn, T., D.M. Farmer, S. Vagle, S.A. Thorpe, and M. Cure. 1992. “Measurements of bubble plumes and turbulence from a submarine.” *Atmosphere-Ocean* 30 (3): 419–440. https://doi.org/10.1080/07055900.1992.9649447.

Osborn, T. R. 1980. “Estimates of the local rate of vertical diffusion from dissipation measurements.” *J. Phys. Oceanogr.* 10:83–89. https://doi.org/10.1175/1520-0485(1980)010⟨0083:EOTLRO⟩2.0.CO;2.

Paulson, Clayton A., and James J. Simpson. 1977. “Irradiance Measurements in the Upper Ocean.” *Journal of Physical Oceanography* 7 (6): 952–956. https://doi.org/10.1175/1520-0485(1977)007⟨0952:imituo⟩2.0.co;2.

Pearson, Brodie C., Alan L. M. Grant, Jeff A. Polton, and Stephen E. Belcher. 2015. "Langmuir Turbulence and Surface Heating in the Ocean Surface Boundary Layer." *Journal of Physical Oceanography* 45 (12): 2897–2911. https://doi.org/10.1175/jpo-d-15-0018.1.

Peltier, WR, and CP Caulfield. 2003. "Mixing efficiency in stratified shear flows." *Annual review of fluid mechanics* 35 (1): 135–167. https://doi.org/10.1146/annurev.fluid.35.101101.161144.

Pham, Hieu T., and Sutanu Sarkar. 2014. "Evolution of an asymmetric turbulent shear layer in a thermocline." *Journal of Turbulence* 15 (7): 449–471. https://doi.org/10.1080/14685248.2014.914216.

Pham, Hieu T., Sutanu Sarkar, Leah Johnson, Baylor Fox-Kemper, Peter P. Sullivan, and Qing Li. 2023. "Multi-Scale Temporal Variability of Turbulent Mixing During a Monsoon Intra-Seasonal Oscillation in the Bay of Bengal: An LES Study." *Journal of Geophysical Research: Oceans* 128 (1). https://doi.org/10.1029/2022jc018959.

Pham, Hieu T.., Sutanu Sarkar, and Kyle A. Brucker. 2009. "Dynamics of a stratified shear layer above a region of uniform stratification." *Journal of Fluid Mechanics* 630:191–223. https://doi.org/10.1017/s0022112009006478.

Pinkel, R. 1985. "A Wavenumber-frequency Spectrum of Upper Ocean Shear." *J. Phys. Oceanogr.* 15:1453–1569. https://doi.org/10.1175/1520-0485(1985)015⟨1453:AWFSOU⟩2.0.CO;2.

Pinkel, R., M. A. Goldin, J. A. Smith, O. M. Sun, A. A. Aja, M. N. Bui, and T. Hughen. 2011. "The Wirewalker: A Vertically Profiling Instrument Carrier Powered by Ocean Waves." *Journal of Atmospheric and Oceanic Technology* 28 (3): 426–435. https://doi.org/10.1175/2010jtecho805.1.

Pinkel, Robert. 2008. "Advection, Phase Distortion, and the Frequency Spectrum of Finescale Fields in the Sea." *Journal of Physical Oceanography* 38 (2): 291–313. https://doi.org/10.1175/2007jpo3559.1.

Pizzo, Nick, W. Kendall Melville, and Luc Deike. 2019. "Lagrangian Transport by Nonbreaking and Breaking Deep-Water Waves at the Ocean Surface." *Journal of Physical Oceanography* 49 (4): 983–992. https://doi.org/10.1175/jpo-d-18-0227.1.

Plueddemann, AJ, and JT Farrar. 2006. "Observations and models of the energy flux from the wind to mixed-layer inertial currents." *Deep Sea Research Part II: Topical Studies in Oceanography* 53 (1): 5–30. https://doi.org/10.1016/j.dsr2.2005.10.017.

Plueddemann, Albert J., Jerome A. Smith, David M. Farmer, Robert A. Weller, William R. Crawford, Robert Pinkel, Svein Vagle, and Anand Gnanadesikan. 1996. "Structure and variability of Langmuir circulation during the Surface Waves Processes Program." *Journal of Geophysical Research: Oceans* 101 (C2): 3525–3543. https://doi.org/10.1029/95jc03282.

Pollard, R.T., and R.C. Millard. 1970. "Comparison between observed and simulated wind-generated inertial oscillations." *Deep Sea Research and Oceanographic Abstracts* 17 (4): 813–821. https://doi.org/https://doi.org/10.1016/0011-7471(70)90043-4.

Polzin, Kurt L, Binbin Wang, Zhankun Wang, Fred Thwaites, and Albert J Williams III. 2021. "Moored flux and dissipation estimates from the northern deepwater gulf of Mexico." *Fluids* 6 (7): 237. https://doi.org/10.3390/fluids6070237.

Price, James F. 1979. "On the scaling of stress-driven entrainment experiments." *Journal of Fluid Mechanics* 90 (3): 509–529. https://doi.org/10.1017/S0022112079002366.

Reichl, Brandon G., Alistair Adcroft, Stephen M. Griffies, and Robert Hallberg. 2022. "A Potential Energy Analysis of Ocean Surface Mixed Layers." *Journal of Geophysical Research: Oceans* 127 (7). https://doi.org/10.1029/2021jc018140.

Reichl, Brandon G., Isaac Ginis, Tetsu Hara, Biju Thomas, Tobias Kukulka, and Dong Wang. 2016. "Impact of Sea-State-Dependent Langmuir Turbulence on the Ocean Response to a Tropical Cyclone." *Monthly Weather Review* 144 (12): 4569–4590. https://doi.org/10.1175/mwr-d-16-0074.1.

Sarkar, Sutanu, and Hieu T Pham. 2019. "Turbulence and thermal structure in the upper ocean: Turbulence-resolving simulations." *Flow, Turbulence and Combustion* 103 (4): 985–1009. https://doi.org/10.1007/s10494-019-00065-5.

Schultz, C., S. C. Doney, W. G. Zhang, H. Regan, P. Holland, M. P. Meredith, and S. Stammerjohn. 2020. "Modeling of the Influence of Sea Ice Cycle and Langmuir Circulation on the Upper Ocean Mixed Layer Depth and Freshwater Distribution at the West Antarctic Peninsula." *Journal of Geophysical Research: Oceans* 125 (8). https://doi.org/10.1029/2020jc016109.

Simecek-Beatty, Debra, and William J. Lehr. 2017. "Extended oil spill spreading with Langmuir circulation." *Marine Pollution Bulletin* 122 (1-2): 226–235. https://doi.org/10.1016/j.marpolbul.2017.06.047.

Skyllingstad, Eric D., and Donald W. Denbo. 1995. "An ocean large-eddy simulation of Langmuir circulations and convection in the surface mixed layer." *Journal of Geophysical Research* 100 (C5): 8501. https://doi.org/10.1029/94jc03202.

Skyllingstad, Eric D., W. D. Smyth, and G. B. Crawford. 2000. "Resonant Wind-Driven Mixing in the Ocean Boundary Layer." *Journal of Physical Oceanography* 30 (8): 1866–1890. https://doi.org/10.1175/1520-0485(2000)030⟨1866:rwdmit⟩2.0.co;2.

Smagorinsky, Joseph. 1963. “General Circulation Experiments with the Primitive Equations.” *Monthly Weather Review* 91 (3): 99–164. https://doi.org/10.1175/1520-0493(1963)091⟨0099:gcewtp⟩2.3.co;2.

Smith, Jerome A. 1992. “Observed growth of Langmuir circulation.” *Journal of Geophysical Research: Oceans* 97 (C4): 5651–5664. https://doi.org/10.1029/91jc03118.

Smyth, WD, and WR Peltier. 1991. “Instability and transition in finite-amplitude Kelvin–Helmholtz and Holmboe waves.” *Journal of Fluid Mechanics* 228:387–415. https://doi.org/10.1017/S0022112091002756.

Smyth, William D., and James N. Moum. 2000. “Length scales of turbulence in stably stratified mixing layers.” *Physics of Fluids* 12 (6): 1327–1342. https://doi.org/10.1063/1.870385.

———. 2012. “Ocean Mixing by Kelvin-Helmholtz Instability.” *Oceanography* 25 (2): 140–149.

Smyth, William D., Eric D. Skyllingstad, Gregory B. Crawford, and Hemantha Wijesekera. 2002. “Nonlocal fluxes and Stokes drift effects in the K-profile parameterization.” *Ocean Dynamics* 52 (3): 104–115. https://doi.org/10.1007/s10236-002-0012-9.

Solano, Miguel, and Yalin Fan. 2022. “A new K-profile parameterization for the ocean surface boundary layer under realistic forcing conditions.” *Ocean Modelling* 171:101958. https://doi.org/10.1016/j.ocemod.2022.101958.

Spydell, Matthew S., Falk Feddersen, and Jamie Macmahan. 2019. “The Effect of Drifter GPS Errors on Estimates of Submesoscale Vorticity.” *Journal of Atmospheric and Oceanic Technology* 36 (11): 2101–2119. https://doi.org/10.1175/jtech-d-19-0108.1.

Stokes, Ian A., Samuel M. Kelly, Andrew J. Lucas, Amy F. Waterhouse, Caitlin B. Whalen, Thilo Klenz, Verena Hormann, and Luca Centurioni. 2024. “A Generalized Slab Model.” *Journal of Physical Oceanography* 54 (3): 949–965. https://doi.org/10.1175/JPO-D-23-0167.1.

Sullivan, Peter P., and James C. McWilliams. 2010. “Dynamics of Winds and Currents Coupled to Surface Waves.” *Annual Review of Fluid Mechanics* 42 (1): 19–42. https://doi.org/10.1146/annurev-fluid-121108-145541.

———. 2017. “Frontogenesis and frontal arrest of a dense filament in the oceanic surface boundary layer.” *Journal of Fluid Mechanics* 837:341–380. https://doi.org/10.1017/jfm.2017.833.

Sullivan, Peter P., James C. McWilliams, and W. Kendall Melville. 2007. “Surface gravity wave effects in the oceanic boundary layer: large-eddy simulation with vortex force and stochastic breakers.” *Journal of Fluid Mechanics* 593:405–452. https://doi.org/10.1017/s002211200700897x.

Sullivan, Peter P., Leonel Romero, James C. McWilliams, and W. Kendall Melville. 2012. “Transient Evolution of Langmuir Turbulence in Ocean Boundary Layers Driven by Hurricane Winds and Waves.” *Journal of Physical Oceanography* 42 (11): 1959–1980. https://doi.org/10.1175/jpo-d-12-025.1.

Sullivan, Peter P., Jeffrey C. Weil, Edward G. Patton, Harmen J. J. Jonker, and Dmitrii V. Mironov. 2016. “Turbulent Winds and Temperature Fronts in Large-Eddy Simulations of the Stable Atmospheric Boundary Layer.” *Journal of the Atmospheric Sciences* 73 (4): 1815–1840. https://doi.org/10.1175/jas-d-15-0339.1.

Sutherland, Bruce R., Michelle DiBenedetto, Alexis Kaminski, and Ton van den Bremer. 2023. “Fluid dynamics challenges in predicting plastic pollution transport in the ocean: A perspective.” *Physical Review Fluids* 8 (7). https://doi.org/10.1103/physrevfluids.8.070701.

Sutherland, Peter, and W. Kendall Melville. 2015. “Field Measurements of Surface and Near-Surface Turbulence in the Presence of Breaking Waves.” *Journal of Physical Oceanography* 45 (4): 943–965. https://doi.org/10.1175/jpo-d-14-0133.1.

Teixeira, M. A. C., and S. E. Belcher. 2002. "On the distortion of turbulence by a progressive surface wave." *Journal of Fluid Mechanics* 458:229–267. https://doi.org/10.1017/s0022112002007838.

Tejada-Martinez, A. E., and C. E. Grosch. 2007. "Langmuir turbulence in shallow water. Part 2. Large-eddy simulation." *Journal of Fluid Mechanics* 576:63–108. https://doi.org/10.1017/s0022112006004587.

Thomas, Leif N, Luc Rainville, Olivier Asselin, William R Young, James Girton, Caitlin B Whalen, Luca Centurioni, and Verena Hormann. 2020. "Direct observations of near-inertial wave ζ-refraction in a dipole vortex." *Geophys. Res. Lett.* 47 (21): e2020GL090375. https://doi.org/https://doi.org/10.1029/2020GL090375.

Thomas, Leif N., Eric D. Skyllingstad, Luc Rainville, Verena Hormann, Luca Centurioni, James N. Moum, Olivier Asselin, and Craig M. Lee. 2023. "Damping of Inertial Motions through the Radiation of Near-Inertial Waves in a Dipole Vortex in the Iceland Basin." *Journal of Physical Oceanography* 53 (8): 1821–1833. https://doi.org/10.1175/jpo-d-22-0202.1.

Thorpe, S. A., T. R. Osborn, D. M. Farmer, and S. Vagle. 2003. "Bubble Clouds and Langmuir Circulation: Observations and Models." *Journal of Physical Oceanography* 33 (9): 2013–2031. https://doi.org/10.1175/1520-0485(2003)033⟨2013:bcalco⟩2.0.co;2.

Thorpe, S. A., T. R. Osborn, J. F. E. Jackson, A. J. Hall, and R. G. Lueck. 2003. "Measurements of Turbulence in the Upper-Ocean Mixing Layer Using Autosub." *Journal of Physical Oceanography* 33 (1): 122–145. https://doi.org/10.1175/1520-0485(2003)033⟨0122:motitu⟩2.0.co;2.

Thorpe, S.A. 2004. "Langmuir Circulation." *Annual Review of Fluid Mechanics* 36 (1): 55–79. https://doi.org/10.1146/annurev.fluid.36.052203.071431.

Van Roekel, L. P., B. Fox-Kemper, P. P. Sullivan, P. E. Hamlington, and S. R. Haney. 2012. "The form and orientation of Langmuir cells for misaligned winds and waves." *Journal of Geophysical Research: Oceans* 117 (C5). https://doi.org/10.1029/2011jc007516.

VanDine, Alexandra, Hieu T. Pham, and Sutanu Sarkar. 2021. "Turbulent shear layers in a uniformly stratified background: DNS at high Reynolds number." *Journal of Fluid Mechanics* 916:A42. https://doi.org/10.1017/jfm.2021.212.

Veron, F., and W. Kendall Melville. 2001. "Experiments on the stability and transition of wind-driven water surfaces." *Journal of Fluid Mechanics* 446:25–65. https://doi.org/10.1017/s0022112001005638.

Veron, Fabrice, W. Kendall Melville, and Luc Lenain. 2008a. "Infrared Techniques for Measuring Ocean Surface Processes." *Journal of Atmospheric and Oceanic Technology* 25 (2): 307–326. https://doi.org/10.1175/2007jtecho524.1.

———. 2008b. "Wave-Coherent Air–Sea Heat Flux." *Journal of Physical Oceanography* 38 (4): 788–802. https://doi.org/10.1175/2007jpo3682.1.

———. 2009. "Measurements of Ocean Surface Turbulence and Wave–Turbulence Interactions." *Journal of Physical Oceanography* 39 (9): 2310–2323. https://doi.org/10.1175/2009jpo4019.1.

Voet, Gunnar, Amy Waterhouse, Anna Savage, Eric Kunze, Jennifer MacKinnon, Matthew Alford, John Colosi, Harper Simmons, Thilo Klenz, Samuel Kelly, James Moum, Caitlin Whalen, Ren-Chieh Lien, and James Girton. 2024. "Near-Inertial Energy Variability in a Strong Mesoscale Eddy Field in the Iceland Basin." *Oceanography,* https://doi.org/10.5670/oceanog.2024.302.

Vrećica, Teodor, Nick Pizzo, and Luc Lenain. 2022. "Airborne Observations of Shoaling and Breaking Internal Waves." *Geophysical Research Letters* 49 (21). https://doi.org/10.1029/2022gl100622.

Wagner, Gregory LeClaire, Nick Pizzo, Luc Lenain, and Fabrice Veron. 2023. "Transition to turbulence in wind-drift layers." *Journal of Fluid Mechanics* 976. https://doi.org/10.1017/jfm.2023.920.

Wang, Dong, and Tobias Kukulka. 2021a. "Wind- and Wave-Driven Reynolds Stress and Velocity Shear in the Upper Ocean for Idealized Misaligned Wind-Wave Conditions." *Journal of Physical Oceanography* 51 (2): 633–644. https://doi.org/10.1175/jpo-d-20-0157.1.

Wang, Dong, Tobias Kukulka, Brandon G. Reichl, Tetsu Hara, and Isaac Ginis. 2019. "Wind and Wave Misalignment Effects on Langmuir Turbulence in Tropical Cyclone Conditions." *Journal of Physical Oceanography* 49 (12): 3109–3126. https://doi.org/10.1175/jpo-d-19-0093.1.

Wang, Dong, Tobias Kukulka, Brandon G. Reichl, Tetsu Hara, Isaac Ginis, and Peter P. Sullivan. 2018. "Interaction of Langmuir Turbulence and Inertial Currents in the Ocean Surface Boundary Layer under Tropical Cyclones." *Journal of Physical Oceanography* 48 (9): 1921–1940. https://doi.org/10.1175/jpo-d-17-0258.1.

Wang, Xingchi, and Tobias Kukulka. 2021b. "Ocean Surface Boundary Layer Response to Abruptly Turning Winds." *Journal of Physical Oceanography,* https://doi.org/10.1175/jpo-d-20-0198.1.

Wang, Xingchi, Tobias Kukulka, J. Thomas Farrar, Albert J. Plueddemann, and Seth F. Zippel. 2023. "Langmuir Turbulence Controls on Observed Diurnal Warm Layer Depths." *Geophysical Research Letters* 50 (10). https://doi.org/10.1029/2023gl103231.

Wang, Xingchi, Tobias Kukulka, and Albert J. Plueddemann. 2022. “Wind Fetch and Direction Effects on Langmuir Turbulence in a Coastal Ocean.” *Journal of Geophysical Research: Oceans* 127 (5). https://doi.org/10.1029/2021jc018222.

Watanabe, Michio, and Toshiyuki Hibiya. 2002. “Global estimates of the wind-induced energy flux to inertial motions in the surface mixed layer.” *Geophysical Research Letters* 29 (8). https://doi.org/10.1029/2001gl014422.

Watanabe, Tomoaki, James J. Riley, Koji Nagata, Ryo Onishi, and Keigo Matsuda. 2018. “A localized turbulent mixing layer in a uniformly stratified environment.” *Journal of Fluid Mechanics* 849:245–276. https://doi.org/10.1017/jfm.2018.400.

Waterhouse, Amy F, Jennifer A MacKinnon, Jonathan D Nash, Matthew H Alford, Eric Kunze, Harper L Simmons, Kurt L Polzin, Louis C St Laurent, Oliver M Sun, Robert Pinkel, Lynne D. Talley, C B Whalen, Tycho N. Huussen, Glenn S Carter, Ilker Fer, Stephanie Waterman, Alberto C Naveira Garabato, T B Sanford, and Craig M Lee. 2014. “Global patterns of diapycnal mixing from measurements of the turbulent dissipation rate.” *J. Phys. Oceanogr.* 44 (7): 1854–1872. https://doi.org/10.1175/JPO-D-13-0104.1.

Webb, A., and B. Fox-Kemper. 2011. “Wave spectral moments and Stokes drift estimation.” *Ocean Modelling* 40 (3-4): 273–288. https://doi.org/10.1016/j.ocemod.2011.08.007.

———. 2015. “Impacts of wave spreading and multidirectional waves on estimating Stokes drift.” *Ocean Modelling* 96:49–64. https://doi.org/10.1016/j.ocemod.2014.12.007.

Weller, Robert A. 1982. “The Relation of Near-Inertial Motions Observed in the Mixed layer During the JASIN (1978) Experiment to the Local Wind Stress and to the Quasi-Geostrophic Flow Field.” *Journal of Physical Oceanography* 12 (10): 1122–1136. https://doi.org/10.1175/1520-0485(1982)012⟨1122:tronim⟩2.0.co;2.

Weller, Robert A., Jerome P. Dean, James F. Price, Erika A. Francis, John Marra, and David C. Boardman. 1985. "Three-Dimensional Flow in the Upper Ocean." *Science* 227 (4694): 1552–1556. https://doi.org/10.1126/science.227.4694.1552.

Weller, Robert A., and James F. Price. 1988. "Langmuir circulation within the oceanic mixed layer." *Deep Sea Research Part A. Oceanographic Research Papers* 35 (5): 711–747. https://doi.org/10.1016/0198-0149(88)90027-1.

Wijesekera, Hemantha W., David W. Wang, and Ewa Jarosz. 2020. "Dynamics of the Diurnal Warm Layer: Surface Jet, High-Frequency Internal Waves, and Mixing." *Journal of Physical Oceanography* 50 (7): 2053–2070. https://doi.org/10.1175/JPO-D-19-0285.1.

Winters, Kraig B., and Eric A. D'Asaro. 1996. "Diascalar flux and the rate of fluid mixing." *Journal of Fluid Mechanics* 317:179–193. https://doi.org/10.1017/s0022112096000717.

Winters, Kraig B., Peter N. Lombard, James J. Riley, and Eric A. D'Asaro. 1995. "Available potential energy and mixing in density-stratified fluids." *Journal of Fluid Mechanics* 289:115–128. https://doi.org/10.1017/s002211209500125x.

Wunsch, Carl. 2020. "Is the Ocean Speeding Up? Ocean Surface Energy Trends." *Journal of Physical Oceanography* 50 (11): 3205–3217. https://doi.org/10.1175/jpo-d-20-0082.1.

Yan, Chao, James C. McWilliams, and Marcelo Chamecki. 2021. "Generation of attached Langmuir circulations by a suspended macroalgal farm." *Journal of Fluid Mechanics* 915. https://doi.org/10.1017/jfm.2021.111.

Zappa, C.J., and A.T. Jessup. 2005. "High-Resolution Airborne Infrared Measurements of Ocean Skin Temperature." *IEEE Geoscience and Remote Sensing Letters* 2 (2): 146–150. https://doi.org/10.1109/lgrs.2004.841629.

Zedel, Len, and David Farmer. 1991a. "Organized structures in subsurface bubble clouds: Langmuir circulation in the open ocean." *Journal of Geophysical Research: Oceans* 96 (C5): 8889–8900. https://doi.org/10.1029/91jc00189.

———. 1991b. "Organized structures in subsurface bubble clouds: Langmuir circulation in the open ocean." *Journal of Geophysical Research* 96 (C5): 8889. https://doi.org/10.1029/91jc00189.

Zeiden, Kristin, Jim Thomson, Andrey Shcherbina, and Eric D'Asaro. 2024. "Observations of elevated mixing and periodic structures within diurnal warm layers." *Journal of Geophysical Research: Oceans* 129 (11): e2024JC021399. https://doi.org/10.1029/2024JC021399.

Zeiden, Kristin L., Daniel L. Rudnick, Jennifer A. MacKinnon, Verena Hormann, and Luca Centurioni. 2022. "Vorticity in the Wake of Palau from Lagrangian Surface Drifters." *Journal of Physical Oceanography* 52 (9): 2237–2255. https://doi.org/10.1175/JPO-D-21-0252.1.

Zheng, Bofu, Andrew J. Lucas, Robert Pinkel, and Arnaud Le Boyer. 2022. "Fine-Scale Velocity Measurement on the Wirewalker Wave-Powered Profiler." *Journal of Atmospheric and Oceanic Technology* 39 (2): 133–147. https://doi.org/10.1175/jtech-d-21-0048.1.

Zippel, Seth F, J Thomas Farrar, Christopher J Zappa, Una Miller, Louis St. Laurent, Takashi Ijichi, Robert A Weller, Leah McRaven, Sven Nylund, and Deborah Le Bel. 2021. "Moored turbulence measurements using pulse-coherent Doppler sonar." *Journal of Atmospheric and Oceanic Technology* 38 (9): 1621–1639. https://doi.org/10.1175/JTECH-D-21-0005.1.

Zippel, Seth F., J. Thomas Farrar, Christopher J. Zappa, and Albert J. Plueddemann. 2022. "Parsing the Kinetic Energy Budget of the Ocean Surface Mixed Layer." *Geophysical Research Letters* 49 (2). https://doi.org/10.1029/2021gl095920.